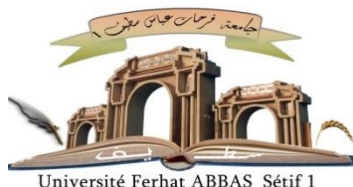


الجمهورية الجزائرية الديمقراطية الشعبية
République Algérienne Démocratique et Populaire
Ministère de L'Enseignement Supérieur et de la Recherche Scientifique



UNIVERSITÉ FERHAT ABBAS - SETIF1

FACULTÉ DE TECHNOLOGIE

THÈSE

Présentée au Département de génie des procédés

Pour l'obtention du diplôme de

DOCTORAT

Domaine: Sciences et Technologie

Filière: Génie des procédés

Option: Génie chimique

Par

HARIZI INTISSAR

THÈME

**Synthèse et caractérisation des matériaux à base de zéolithe et
d'hydroxydes doubles lamellaires : Application à l'élimination
des colorants**

Soutenue le 30/01/2020 devant le Jury :

BOUTAHALA Mokhtar	Professeur	Univ. Ferhat Abbas Sétif 1	Président
CHEBLI Derradji	M.C.A.	Univ. Ferhat Abbas Sétif 1	Directeur de thèse
BOUGUETTOUCHA Abdellah	Professeur	Univ. Ferhat Abbas Sétif 1	Co-Directeur
OMARI Mahmoud	Professeur	Universite de Biskra	Examineur
BERKAT Djamel	Professeur	Universite de Biskra	Examineur

To my parents, to my husband, to Mounib

To all my family and beloveds...

Acknowledgement

Above all, thanks to Allah for guiding me, giving me the health, the patience the courage and the capacity to accomplish this work.

I would like to express my infinite gratitude and sincere esteem to my supervisor **Dr. Derradji Chebli** for his constant help, guidance, valuable advices especially for his moral support and understanding. I would never been able to complete this work without his incredible encouragement and follow up. I have been extremely lucky to have a supervisor who cared so much about my research and who responded to my emails and queries so immediately. I would also like to thank **Dr. Abdellah Bouguettoucha** for his co-direction, support, kindness and his immediate response to emails and questions.

I would like to thank **Prof. Rohani Sohrab**, professor at the University of Western Ontario (Canada) as well as the team members of the **Zeolitic & Nano Materials Laboratory** at Western (ZNML-Western) for the warm welcome and the opportunity to work with them during the two years of my internship. A special thank to **Ms. Tahani El-dahri**, Ph.D. student at the Department of Chemical and Biochemical at Western University, for her help with the lab material and the several fruitful discussions on this research topic.

I am truly grateful to my parents for their immeasurable love and the sacrifices that they have made to help me succeed in my education and research career. They have always encouraged me to pursue my dreams and have put all their efforts to support me to reach my goals.

Also, no word can explain how much I am thankful to my husband for his support, encouragements and understanding during the period of my PhD studies.

Finally, I thank all my family members, friends, colleagues, and all people who helped me and encouraged me to accomplish this thesis.

Contents

Acknowledgement	3
Contents	4
List of figures	9
List of tables	12
Abstract.....	14
General introduction	15

Chapter I: Background

I.1	Introduction	22
I.2	Generalities on dyes.....	23
I.2.1	Definition and structure.....	23
I.2.2	Dyes classification.....	23
I.2.3	Azo dyes.....	25
I.2.4	The hazard and toxicity of dyes	26
I.2.5	Different methods for dyes removal.....	26
I.3	Generalities on the adsorption	27
I.3.1	Physical adsorption	28
I.3.2	Chemical adsorption.....	28
I.3.3	Adsorption for dye removal	28
I.4	Layered double hydroxides (LDH).....	29
I.4.1	Definition and structure.....	29
I.4.2	Methods of synthesis.....	31
I.4.2.1	Coprecipitation	31
I.4.2.2	Ion-exchange	32

I.4.2.3	Reconstruction.....	33
I.4.3	Applications	33
I.4.4	Removal of dyes using LDH in literature	34
I.5	Zeolites	35
I.5.1	History	35
I.5.2	Definition and structure.....	36
I.5.3	Properties and applications.....	39
I.5.3.1	Adsorption and molecular sieve	39
I.5.3.2	Ion exchange.....	40
I.5.4	Methods of zeolite synthesis	40
I.5.4.1	Hydrothermal synthesis using pure chemicals	40
I.5.4.2	Synthesis of zeolite using waste materials	41
I.5.4.3	Effects of zeolitization parameters	44
I.5.4.4	Methods of zeolite synthesis in literature	45
I.6	Introduction to the Response Surface Methodology (RSM)	46
I.6.1	The Experimental design.....	47
I.6.1.1	Full three-level factorial designs	48
I.6.1.2	Box–Behnken designs	49
I.6.1.3	Central composite design	49
I.6.1.4	Doehlert design.....	50
I.6.2	Mathematical modeling and data fitting.....	51
I.6.3	Experimental Design software: Design-Expert 7.....	53

Chapter II:Materials and methods

II.1	Introduction	56
II.2	Reagents	56
II.2.1	Products used for the synthesis of LDH.....	56
II.2.2	Products used for the synthesis of Zeolite Na-P	56
II.2.3	Products used as adsorbates	57

II.2.3.1	The Acid Red 66 (AR66).....	57
II.2.3.2	The Congo Red (CR)	58
II.3	Methods of adsorbents preparation.....	59
II.3.1	Synthesis of LDH by coprecipitation method	59
II.3.2	Synthesis of calcined LDH.....	59
II.3.3	Method of zeolite synthesis.....	60
II.3.3.1	Pre-treatment of the CFA	60
II.3.3.2	CFA conversion into zeolite	61
II.4	Methods of analysis and characterization.....	62
II.4.1	X-ray diffraction analysis.....	62
II.4.2	Fourier-transform infrared spectroscopy (FT-IR).....	63
II.4.3	Wavelength dispersive X-ray Fluorescence (XRF)	64
II.4.4	Scanning electron microscopy (SEM).....	65
II.4.5	N ₂ sorption-desorption analysis	65
II.4.6	Thermogravimetric and differential thermal analysis TGA/DTA.....	66
II.4.7	Zeta potential measurement	66
II.5	Study of the adsorption.....	67
II.5.1	Ultraviolet–visible spectroscopy (UV/VIS).....	67
II.5.2	Kinetics of adsorption	68
II.5.2.1	The pseudo-first-order model	69
II.5.2.2	Pseudo-second-order model.....	69
II.5.2.3	Elovich model	70
II.5.2.4	Diffusion-chemisorption model.....	70
II.5.2.5	Intraparticle diffusion model	70
II.5.3	Isotherms models.....	71
II.5.3.1	Langmuir model.....	72
II.5.3.2	Freundlich model	72
II.5.3.3	Sips model.....	73
II.5.3.4	Toth model	73
II.5.4	Thermodynamic study.....	74

II.6	Experimental Design software: Design-Expert 7	74
------	---	----

Chapter III: Mg-Cu-Al-Fe LDH to enhance the adsorption of Acid Red 66 Dye: Characterization, kinetics and isotherm analysis

III.1	Introduction	77
III.2	Materials and Methods	77
III.2.1	Characterization	77
III.2.2	Adsorption experiments	78
III.3	Results and Discussion	79
III.3.1	Characterizations of the adsorbents.....	79
III.3.2	Adsorption behavior	87
III.3.2.1	Effect of the initial solution pH on the dye adsorption.....	87
III.3.2.2	Effect of the adsorbent dosage.....	89
III.3.2.3	Effect of the initial concentration and the contact time	91
III.3.2.4	Effect of coexisting ions on dye removal	92
III.3.3	Kinetic modeling	93
III.3.4	Adsorption mechanism.....	94
III.3.5	Equilibrium modeling	97
III.3.6	Adsorption thermodynamics	100
III.4	Conclusion.....	100

Chapter IV: The removal of anionic dyes from wastewater onto zeolite Na-P synthesized from waste coal fly ash

IV.1	Introduction	103
IV.2	Materials and methods.....	103
IV.2.1	Characterization	103
IV.2.2	Adsorption experiments	104
IV.2.3	Experimental design.....	105

IV.3	Results and discussion	106
IV.3.1	Characterization of the adsorbent.....	106
IV.3.2	Study of the Adsorption of CR on ZNa-P	111
IV.3.2.1	The effect of the pH	111
IV.3.2.2	The effect of the adsorbent mass	113
IV.3.2.3	The effect of the initial concentration and the contact time.....	114
IV.3.2.4	Modeling of the kinetics of CR adsorption on ZNa-P	115
IV.3.2.5	Adsorption mechanism of CR on ZNa-P	116
IV.3.2.6	Study of the isotherms of adsorption	118
IV.3.2.7	Effect of the temperature and thermodynamic study	121
IV.3.3	Study of the Adsorption of AR66 on ZNa-P using CCD.....	122
IV.3.3.1	CCD regression model development	122
IV.3.3.2	The effect of the pH	125
IV.3.3.3	The effect of the initial dye concentration	126
IV.3.3.4	The effect of the adsorbent mass	126
IV.3.3.5	The effect of the contact time	126
IV.3.3.6	Investigation of the interaction effects between the different parameters	129
IV.3.3.7	Kinetics of adsorption	135
IV.3.3.8	Kinetics modeling.....	135
IV.3.3.9	Adsorption mechanism of AR66 on ZNa-P	137
IV.3.3.10	Isotherms of adsorption	139
IV.3.3.11	Effect of the temperature and thermodynamic study	142
IV.3.4	Proposed adsorption mechanism of CR and AR66 on ZNa-P	143
IV.3.5	Comparison of adsorption capacity of CR / AR66 on different adsorbents.....	144
IV.4	Conclusion	145
	References.....	147
	General conclusion and perspectives.....	171

List of figures

Chapter I

Figure.I.1. Example of the chromophore group placed in (a) non -conjugated system (b) conjugated system	23
Figure.I.2. Schematic representation of the general structure of LDH	30
Figure.I.3. Schematic representation of the anion exchange property of the LDH.....	33
Figure.I.4. schematic representation of the reconstruction phenomenon of the LDH	33
Figure.I.5. General structure of zeolite.....	36
Figure.I.6. Structure of some common zeolites frameworks (a) LTA, (b) FAU, (c) GIS, (d) SOD, (e) CHA, (f) ANA, (g) EDI and (h) MER	38
Figure.I. 7. Schematic illustration of zeolitization process of CFA particle (a) Dissolution of Al and Si content of CFA into the solution (b) Condensation of Al and Si polymers (dimers, trimers etc.) on the surface of CFA particle (c) Nucleation of zeolites (d) Zeolite crystal growth.	43
Figure.I.8. Three-level factorial design for the optimization of (a) two variables and (b) three variables.....	48
Figure.I.9. Box–Behnken design for the optimization of three variables	49
Figure.I.10. Central composite design of: (a) two variables ($\alpha=1.41$) and (b) three variables ($\alpha=1.68$).	50
Figure.I.11. Doehlert design for the of two variables.....	51
Figure.I.12. Some profiles of surface response generated from a quadratic model in the optimization of two variables. (a) maximum, (b) plateau, (c) maximum outside the experimental region, (d) minimum, and (e) saddle surfaces.	53

Chapter II

Figure.II.1. Structure of Acid Red 66	58
Figure.II.2. Structure of Congo Red.....	58
Figure.II.3. Schematic presentation of the experimental protocol used for LDH synthesis	60
Figure.II.4. Schematic presentation of the experimental protocol used for ZNa-P synthesis..	61
Figure.II.5. Schematic diagram of the experimental steps used for zeolite Na-P synthesis	62
Figure.II.6. X-ray diffraction phenomenon inside a diffractometer.....	63

Figure.II. 7. The window of Design Expert software.....	75
--	----

Chapter III

Figure.III. 1. XRD patterns of (a) LDH, (b) CLDH, (c) LDH-AR66 and (d) CLDH-AR66..	80
Figure.III. 2. FTIR spectra of (a) LDH, (b) CLDH, (c) AR66, (d) LDH-AR66 and (e) CLDH-AR66.....	81
Figure.III. 3. SEM micrographs of (a) LDH, (b) CLDH	82
Figure.III.4. XRF patterns of LDH and CLDH.....	83
Figure.III.5. N ₂ adsorption desorption isotherms of LDH and CLDH	84
Figure.III.6. The pore size distribution for LDH and CLDH.....	85
Figure.III. 7. TGA and DTA curves of LDH and CLDH (heating rate = 10°C/min, under 40 mL/min N ₂).....	86
Figure.III.8. Initial pH effect on AR66 adsorption onto LDH ($C_0 = 200 \text{ mg.L}^{-1}$, $T = 23^\circ\text{C}$, speed = 250rpm) and CLDH ($C_0 = 800 \text{ mg.L}^{-1}$, $T = 23^\circ\text{C}$, spd = 250rpm).	88
Figure.III.9. Zeta potential distribution of LDH and CLDH.	89
Figure.III.10. Effect of adsorbent dosage on dye adsorption capacity on LDH and CLDH...	90
Figure.III.11. Variation of the removal percentage with the adsorbent dosage onto LDH ($C_0 = 200 \text{ mg L}^{-1}$) and CLDH ($C_0 = 800 \text{ mg L}^{-1}$) at $T = 23^\circ\text{C}$, speed = 250 rpm	90
Figure.III. 12. Effect of contact time and initial dye concentration on dye adsorption on (a) LDH, (b) CLDH. ($\text{pH} = 6.87$, $T = 23^\circ\text{C}$, speed = 250rpm)	91
Figure.III.13. Effect of coexisting ions on dye removal by (a) LDH, (b) CLDH.....	93
Figure.III. 14. Data fitting of the AR66 adsorption kinetics by intra-particle diffusion model (a) LDH, (b) CLDH.	95
Figure.III. 15. Non-linear regression of isotherm experimental data with: (a) Langmuir, and Freundlich and models (b) Sips and Thoth models.	97

Chapter IV

Figure.IV.1. The XRD patterns of CFA and ZNa-P (Q: Quartz, M: Mullite, H: Hematite, C: Calcite, P: zeolite P)	106
Figure.IV.2. The FT-IR spectrum of the raw CFA and the ZNa-P	107
Figure.IV.3. The thermogravimetric and the differential thermal analysis of ZNa-P	109

Figure.IV.4. N ₂ adsorption-desorption isotherms of ZNa-P	110
Figure.IV.5. SEM images of (a) CFA, (b) and (c) ZNa-P	111
Figure.IV.6. The effect of pH on the capacity of adsorption of CR on ZNa-P	112
Figure.IV.7. The effect of the adsorbent mass on the adsorption of CR on ZNa-P	113
Figure.IV.8. Kinetics of adsorption of CR on ZNa-P at different concentrations	114
Figure.IV.9. Plots of the pseudo-second-order kinetics of CR on ZNa-P	115
Figure.IV.10. Intraparticle diffusion plots for the adsorption of CR on ZNa-P	117
Figure.IV.11. Isotherm of CR adsorption on ZNa-P and its nonlinear regression to Langmuir Freundlich Sips and Toth models	120
Figure.IV.12. The effect of the temperature of CR adsorption on ZNa-P.....	121
Figure.IV.13. Diagnostic plot of the predicted values versus actual values.....	124
Figure.IV.14. Normal probability plots of the residuals	124
Figure.IV.15. 2D response surface plots for AR66 removal on ZNa-P	128
Figure.IV.16 Interaction effect of the pH X_1 and the initial dye concentration X_2 on the capacity of adsorption for (a) $X_3= 0.2\text{g/L}$ and $X_4= 25\text{ min}$ (b) $X_3= 1\text{g/L}$ and $X_4= 5\text{min}$	130
Figure.IV.17. Interaction effect of the initial dye concentration X_2 and the adsorbent mass X_3 on the capacity of adsorption for (a) $X_1=2$ and $X_4=25\text{min}$ and (b) $X_1=4$ and $X_4=5\text{min}$	131
Figure.IV.18. The interaction effect of: (a) pH - adsorbent mass X_1X_3 (b) initial concentration - contact time X_2X_4 (c) pH - contact time X_1X_4 (d) adsorbent mass - contact time X_3X_4	134
Figure.IV.19. AR66 adsorption kinetics at different initial concentrations	135
Figure.IV.20. Kinetics of AR66 adsorption onto ZNa-P fitted to the pseudo-second-order.....	137
Figure.IV.21. Kinetic simulation by the Intraparticle diffusion model for different initial concentrations.....	138
Figure.IV.22. Isotherm of AR66 adsorption onto ZNa-P at room temperature $\sim 24^\circ\text{C}$	139
Figure.IV.23. Isotherm data fitted to Langmuir, Freundlich models, Sips and Toth models	140
Figure.IV.24. The effect of the temperature on the AR66 adsorption onn the AR66 adsorption onto ZNa-P	142
Figure.IV.25. The effect of the temperature on the AR66 adsorption onn the AR66 adsorption onto ZNa-P	144

List of tables

Chapter I

Table.I.1. Examples of chromophores and auxochrome groups presents in dyes structure	23
Table.I. 2. Classification based on their chemical structure	24
Table.I. 3. Classification on dyes based on their applications	25
Table.I.4. Common frameworks with their idealized cell parameters and examples of zeolites.	37

Chapter II

Table.II.1. the Chemical and mineral composition of CFA	57
Table.II.2. Some properties of the dye AR66.....	58
Table.II.3. Some properties of the dye CR.....	58

Chapter III

Table.III.1. Elemental analysis of LDH and CLDH	83
Table.III.2. BET textural properties of LDH and CLDH.....	84
Table.III.3. Kinetics model parameters for AR66 adsorption and coefficient of correlation R^2	96
Table.III.4 Langmuir, Freundlich, Sips and Toth parameters for AR66 adsorption on LDH and CLDH	98
Table.III.5. Comparison of the maximum of adsorption capacities reported for dye adsorption on CLDH	99
Table.III.6. Thermodynamic parameters of AR66 adsorption onto LDH and CLDH.	100

Chapter IV

Table.IV.1 The independent variables and their coded levels using CCD.....	106
Table.IV.2. Chemical composition of the synthesized ZNa-P	108
Table.IV.3 Textural properties of ZNa-P	110
Table.IV.4 Comparison of pseudo first order, pseudo second order, Elovich and Diffusion- Chemisorption models for CR adsorption on ZNa-P	116
Table.IV.5. Intraparticle diffusion model parameters	118

Table.IV.6 Langmuir, Freundlich, Sips and Toth parameters for CR adsorption on ZNa-P..	119
Table.IV.7. The thermodynamic parameters of AR66 adsorption onto ZNa-P.....	121
Table.IV.8. Experimental design based on central composite design (CCD) used in this study	122
Table.IV.9. Zeta potential of ZNa-P at different pH	125
Table.IV.10 Comparison of pseudo first order, pseudo second order, Elovich and Diffusion-Chemisorption models for AR66 adsorption on ZNa-P	136
Table.IV.11. Intraparticle diffusion model parameters	138
Table.IV.12 Langmuir, Freundlich, Sips and Toth parameters for AR66 adsorption on ZNa-P	141
Table.IV.13. The thermodynamic parameters of AR66 adsorption onto ZNa-P.....	143
Table.IV.14. The comparison of the adsorption capacities of CR / AR66 on of the studied materials with other materials in literature	145

Appendix

Table. 1. Fit summary for AR66 adsorption onto ZNa-P	178
Table. 2. Analysis of variance (ANOVA) results for the suggested quadratic model.....	179

Abstract

In this research, we are interested in the synthesis of innovative materials that can be used as efficient and cost-effective adsorbents. First, a new layered double hydroxide (LDH) material has been synthesized from raw chemicals by the method of coprecipitation at constant pH. LDH has been prepared based on four metal cations to obtain a quadratic Mg-Cu-Al-Fe LDH reported, for the first time in this work. A part of the obtained LDH has been calcined to obtain metal oxides. Moreover, as a contribution in waste valorisation, an innovative zeolitic material Z-NaP has been prepared from coal fly ash (CFA) waste. The synthesized materials have been carefully characterized by different methods such as XRD, FTIR, TGA/DTA, BET, SEM and XRF. Furthermore, the application of LDH and Z-NaP as adsorbents for anionic dyes has been studied. The kinetics of adsorption, the equilibrium studies and the influences of the different factors such as initial pH, adsorbent mass, contact time and temperature were explored. Extremely high capacities of adsorption have been obtained confirming the efficiency of LDH and Z-NaP for anionic dyes removal.

Keywords: Mg-Cu-Al-Fe LDH, Zeolite Na-P, CFA, Adsorption, Acid Red 66, Congo Red.

Résumé

Dans cette recherche, nous nous intéressons à la synthèse des matériaux innovants qui pourraient être utilisés comme adsorbants efficaces et rentables. D'abord, un nouveau matériau à base d'hydroxyde double lamellaire (HDL) a été synthétisé à partir des produits chimiques par la méthode de coprécipitation à pH constant. L'HDL a été préparée à la base de quatre cations métalliques afin d'obtenir une HDL quadratique Mg-Cu-Al-Fe rapportée pour la première fois dans ce travail. Une partie de la HDL obtenue a été calcinée pour obtenir des oxydes métalliques. Ensuite, comme contribution à la valorisation des déchets, un matériau zéolithique innovant, le Z-NaP, a été préparé à partir des cendres volantes de charbon (CVC) produites comme déchets. Les matériaux synthétisés ont été soigneusement caractérisés par différentes méthodes telles que DRX, IRTF, ATG / ATD, BET, MEB et XRF. De plus, l'application de HDL et de Z-NaP en tant qu'adsorbants a été étudiée. Les cinétiques d'adsorption, les études d'équilibre aussi que l'influences de différents facteurs tels que le pH initial, la masse d'adsorbant, le temps de contact et la température ont été explorés. Des capacités d'adsorption extrêmement élevées ont été obtenues, confirmant l'efficacité de la HDL et du Z-NaP pour l'élimination des colorants anioniques.

Mots clés : Mg-Cu-Al-Fe HDL; Zeolithe Na-P; CVC, Adsorption, Acide Rouge 66, Rouge Congo.

ملخص

في هذا البحث ، اولينا اهتماما لتوليف مواد مبتكرة يمكن استخدامها كمادة ماصة فعالة غير مكلفة. أولاً ، تم تصنيع مادة هيدروكسيد صفائح مزدوجة جديدة من المواد الكيميائية الخام. تم تحضيرها باستعمال أربعة كاتيونات معدنية للحصول على HDL رباعي والذي تم إقتراحه لأول مرة في هذا العمل. كمساهمة في تأمين النفايات ، تم إعداد مادة زيوليتية Z-NaP ، من الرماد المتطاير من الفحم الذي يتم إنتاجه كمخلفات. تم تحديد خصائص المواد المنتجة بطرق مختلفة مثل DRX و IRTF و ATG / ATD و BET و MEB و XRF. بالإضافة إلى ذلك، تم استخدام LDH و Z-NaP كمادة ماصة. تمت دراسة حركية و توازن الامتزاز وكذلك تأثير مختلف العوامل كالحموضة ، وكمية المادة ، ومدة الاحتكاك ودرجة الحرارة. تم الحصول على نسبة امتصاص عالية للغاية ، مما يؤكد فعالية LDH و Z-NaP لإزالة الأصباغ الأنيونية.

الكلمات المفتاحية: Mg-Cu-Al-Fe LDH , زيوليت ب , رماد الفحم المتطاير, أحمر الحمض 66 ، أحمر الكونغو.

General introduction

General introduction

The water pollution has always been a challenging problem for the environment and the human wellbeing. Wastewater coming from different human activities such as agricultural, commercial, industrial, and others, is known to be the source of large types of pollutants. The emission of effluents from textile industries has been a major concern of the modern world due to the great pollution that these effluents promote on the water resources. Before the mid nineteenth century, substances with colouring properties were extracted from natural sources, mainly from animals or vegetables. However, natural dyes were almost completely replaced the synthetic in the beginning of the twentieth century. Today, virtually all dyes and pigments commercially available are synthetic substances. Dyes of all kinds, especially azo dyes, are considered to be among the most harmful contaminants that are contained in the wastewater because of their non-degradability and persistence in the aquatic environment. The resistance to the biodegradability, shown by these compounds, is ensured by their complex chemical structure, involving aromatic rings, azoic linkages and amino groups. The azo dyes are a class of dyes widely used in numerous industries, principally in textile industries [1].

An indication of the scale of the problem is given by the observation that the annual market for dyes is more than 7×10^5 tonnes per year [1] and approximately over 10,000 of different dyes and pigments are used industrially [2]. During the textile process, inefficiency in the colouring generates large amounts of dyes residues, which are directly released into water bodies. Residues of dyes are either discharged in waters that undergo treatment systems of the companies or are released directly into the environment. This causes a severe contamination of water bodies, which is mainly observed and aggravated in areas near the vicinity of textile industries. Studies reported that around 10-15% of the dyes used for industrial purposes are ending up being released to the nature [3]. However, treatment to remove the residual dye amounts was not considered until the early natural dyes were replaced by synthetic dyes and the persistence of such synthetic dyes in the environment was recognised.

Azo dyes, found in the industrial wastewater discharges, are renowned by their visibility, water solubility, degradability, toxicity, carcinogenicity and mutagenicity which cause serious and severe health and environmental problems [4]. Therefore, in a tentative to reduce their

harmful impact, a wide range of research has been devoted to the treatment of the wastewater effluents. For this purpose, several techniques have been applied: coagulation, filtration, degradation by means of special fungi, oxidation, ozonation, ion exchange, neutralization and photocatalysis [5], sonochemical degradation [6]. Due to its low cost, ease of operation and reliability, the adsorption is one of the most popular techniques used in dyes elimination. The activated carbon was the most ordinarily used adsorbent. Since then, tens of materials of different natures have been applied as alternative low-cost sorbents such as alumina, polysaccharide, biopolymers, clays [7], layered double hydroxides [8], zeolites, graphene oxides [4].

Layered double hydroxides (LDHs) are increasingly investigated as potential materials for adsorbents wastewater treatment [9]. Many researchers have studied the capacity of adsorption of many compounds onto different types of LDH. Along with magnesium and aluminium, large cations have been integrated in the synthesis of LDHs including zinc, iron, lithium, calcium, manganese, chromium, cobalt, nickel, copper and others [10]–[12]. To the best of our knowledge, LDHs used as adsorbents reported in literatures were mostly binary [12], [13] or ternary LDHs [14], [15] and rarely quaternary LDH [16]. Their interesting properties including large surface area and high anion exchange capacity give them a considerable interest typically in environmental contaminants removal. The LDHs have been used as adsorbents for a large environmental wastewater pollutant, such as dyes [10], chlorophenols [17], heavy metals [18] and monoatomic ions [19].

Recently, there has been a growing interest in the use of industrial waste to synthesis ecofriendly materials used as effective adsorbents [20]. The valuation of these unused sources (industrial waste) is of great interest since it contributes to diminish environmental pollution by reducing the pile of industrial waste and, then, exploiting that waste for water treatment purposes. The coal fly ash is a by-product generated from coal burning in combustion power plants. It constitutes more than 70% of the combustion solid residues [21]. One of the best ways to recycle the coal fly ash collected after the combustion process is to use it for the synthesis of new materials useful in other fields such as pollutants removal. Many studies have proved that coal fly ash can be transformed to valued compounds efficient for dyes removal, essentially zeolites, mesoporous silica [22], silica aerogels [23].

At the very outset, the zeolite preparation was based on pure alumina and silica chemical products. Afterwards, it was of interest to use other alumina and silica carriers as raw materials to synthesize zeolites with the view of an economical and environment-friendly synthesis. As long as the CFA has a composition rich in alumina and silica, it is considered as a potential raw material for zeolite synthesis [24].

Usually, to explore the adsorption process, researchers apply a conventional method where the “one variable at a time” procedure is used to explore the effect of different parameters. This method allows to examine the effect of each influencing parameter separately from others [25]. The application of an experimental design to study the influence of multi factors on a desired response was found to be more effective and time-saving technique. The response surface methodology (RSM) is one of the most efficient methodologies applied to investigate the influence of multiple factors on a single or multi response system. RSM technique provides in a short time a lot of information on the studied process through a limited number of experiments. In fact, RSM allows to:

- depict the individual and the combined effects of the different parameters on the response.
- define the optimum experimental conditions for which the maximum response is obtained.
- provide a mathematical model that best fits the experimental data.

RSM includes several experimental designs such as Box Behenken design, Doehlert design, three full level factorial design and the central composite design (CCD) which is the most applied RSM design.

The main objective of this work is the synthesis of innovative material based on raw chemicals or using waste then testing their ability to remove pollutants namely anionic dyes from stimulated wastewater. Furthermore, this work highlighted the efficiency of using an experimental design to study a physical and/or chemical process in economizing time, products and energy in comparison with the conventional method used. More specifically, we synthesized a novel layered double hydroxide (LDH) material by the method of coprecipitation at constant pH using pure chemicals. LDH has been prepared based on four metal cations to obtain a quadratic Mg-Cu-Al-Fe LDH reported, for the first time in this work. A part of the obtained LDH has been calcined to obtain calcined LDH (CLDH) with ameliorated properties.

Moreover, as a contribution in waste valorisation, an innovative zeolitic material Z-NaP has been prepared from coal fly ash (CFA) waste. The synthesized materials have been carefully characterized by different methods such as XRD, FTIR, TGA/DTA, BET, SEM and XRF. Furthermore, LDH, CLDH and Z-NaP have been used as adsorbents for the anionic dye acid red 66 (AR66). A preliminary study of the adsorption of congo red (CR) on Z-NaP is also represented. ‘One variable at a time’ method was used to explore the influences of the different factors such as initial pH, adsorbent mass, contact time and temperature on the adsorption capacity of AR66 onto LDH and CLDH while an experimental design was applied to study the capacity of adsorption of that same dye onto Z-NaP. The kinetics of adsorption and the equilibrium studies were fitted to different mathematical models to better understand the adsorption mechanism.

This dissertation is divided into four chapters. The first chapter summarized the background concerning the dyes, the process of adsorption, the experimental designs, the layered double hydroxides and the zeolites including their main structural features and properties. A literature review on competitive adsorption research using layered double hydroxides and zeolite Na-P as adsorbents for dyes removal was also presented in this chapter.

The second chapter summarized the materials and all the methods used to accomplish this research work. First, the methods of preparation of the layered double hydroxide and the zeolite were carefully detailed. Then the methods of characterization as well as the devices and the conditions of analysis were described. The mathematical models applied to describe the kinetics and the isotherms of adsorption were presented at the end of the second chapter.

The results obtained during this work are presented in chapters III and IV in the form of articles. Particularly, the third chapter represents the synthesis of an innovative layered double hydroxide and its application as an adsorbent to remove the dye acid red 66 from wastewater. However, the fourth chapter propose a multi-step method to convert the waste coal fly ash into zeolite Na-P. The obtained zeolite has been used as adsorbent for the anionic dyes congo red and acid red 66. The study of the adsorption of acid red 66 onto zeolite has been investigated using a design software that allows to obtain as much results as the method of one variable with a smaller number of experiments and a shorter time.

Finally, we conclude this thesis by summarizing the conducted investigations and the obtained results as well as providing some perspective for future research directions in this field of study.

Chapter I: Background

I.1 Introduction

Dyes are extensively used in diverse industries where the main consumer domains are textile, tannery, paper, rubber, plastic, electroplating industries, food, cosmetics to name a few. This large use of dyes results in immense quantities of dyestuff effluents discharged directly from the dyeing process to the environment which causes serious environmental problems [26]. Besides water pollution [27], it is a rising danger for the whole ecosystem: human, fauna and flora since they are known as refractory products that may become toxic after decomposition in nature. Despite the continuous development of new methods for wastewater treatment, adsorption is still considered as one the most powerful and the most used methods for the elimination of organic dyes from aqueous solutions with high efficiency as reported in different research studies. Numerous studies have been performed for the development of cheaper and more effective adsorbents that are able to remove the contaminants at trace levels. For instance, Layered double hydroxides and zeolites.

In this background chapter, we have tried to give an overview on the dyes, their classifications and the different techniques used for their elimination from wastewater with an emphasize on the technique of adsorption. The basic aspects of the theory of adsorption are briefly described with a focus on the solid-liquid adsorption. The adsorption isotherms as well as the different models used for the kinetics and equilibrium adsorption modeling are exposed. These models are applied thereafter in the thesis to describe the adsorption mechanisms.

The adsorption process could be economically very profitable if the activated carbon, the most used material as adsorbent, could be replaced by other efficient and less expensive adsorbents. In this chapter we are also presenting two main materials widely used as alternatives for the activated carbon namely layered double hydroxides and zeolites. An overview on these materials is presented including their structures, methods of synthesis, their main properties as well as their applications in the different domains. Moreover, a literature review is performed on the different layered double hydroxides synthesized as well as on their use for dye adsorption. A review of the different methods used in literature for the synthesis of zeolite from coal fly ash (CFA) is, also, presented. An introduction to the response surface methodology and the experimental design is induced at the end of this chapter.

I.2 Generalities on dyes

I.2.1 Definition and structure

A dye is an organic colored compound that is able to share its color with other materials. A dye has at least one group that confers to it the color called chromophore (electron acceptor) and a group that allows its fixation on textile materials called auxochromes (electron donor). Examples of chromophore and auxochrome groups are presented in Table.I.1. The dye substance has a conjugated system with alternating single and double bonds (π bonds). In order that the organic substance gives a color the chromophore group should be located between conjugated systems. The production of colorless substances occurs by the placement of chromophore, azo group, between methyl groups, as it is represented in Figure.I.1. The dyes are characterized by their ability to absorb light in the visible spectrum (400 nm -750nm)

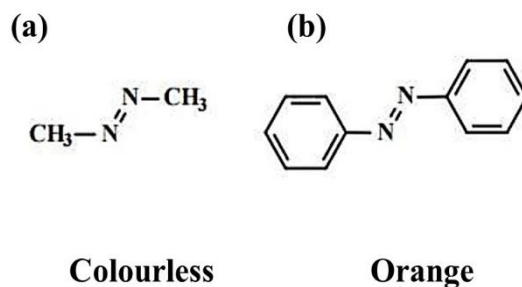


Figure.I.1. Example of the chromophore group placed in (a) non -conjugated system (b) conjugated system

Table.I.1 Examples of chromophores and auxochrome groups presents in dyes structure

Chromophore group [28]	Auxochrome group [29]
Azo (-N=N-)	Amino (-NH ₂)
Sulfur (=C=S)	Chlorine (-Cl)
Nitroso (-N=O, -N-OH)	Hydroxyl (-OH)
Carbonyl (=C=O)	Methyl (-CH ₃)
Vinyl or methane (-C=CH ₂ , =C=)	Sulphonic acid and sodium salts (-SO ₃ H)

I.2.2 Dyes classification

Based on their nature and origin dyes can be classified in tow major classes: natural and synthetic dyes. Natural dyes which were mainly used in textile industries until 1856, beginning in 2600 B.C were manufactured from vegetable and animal sources. For instance, Phoenicians

used the Tyrian purple produced from crushed sea snails in the 15th century B.C. Also, Egyptians used madder plants to extract dyes used to wrap and dye mummies clothes. In 1856, while trying to find a cure to malaria, the first synthetic dye was accidentally explored by William Henry Perkin, it was a reddish-purple dye called “mauve”. Then azo dyes synthesized by diazotization reactions were discovered in 1958 by P. Gries [30].

The dyes could be classified differently based on their chemical structure or their application. Hereafter two major classifications will be presented. Table.I.2 and Table.I.3 present the classification of dyes according to their chemical structure and their applications, respectively.

Table.I.2. Classification based on their chemical structure [31]

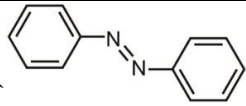
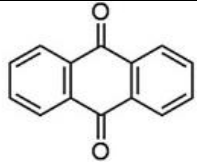
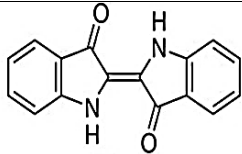
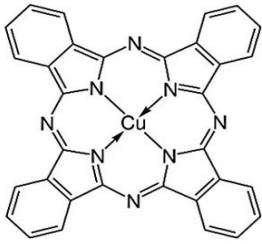
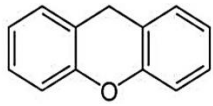
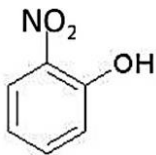
Dyes class	Description	Example
Azo	Its structure contains one or more azo groups $-N=N-$ The most used dyes in textile industry.	
Anthraquinone	its general formula is based on anthraquinone molecules	
Indigoid	These dyes give large range of colors, from orange to turquoise	
Phthalocyanine	Its structure is based on complex structures with a central atom of metal (ex: Cu, Co, Pb, Fe, Mg)	
Xanthene	The compounds of this class provide intensive fluorescence. The most representative member is fluorescein	
Nitro and nitroso dyes.	They have sample structure composed of a nitro group ($-NO_2$) bonded with amine or hydroxyl group	

Table.I.3. Classification on dyes based on their applications [32]

Dyes class	Application
Acid	Wool, nylon, silk, inks, leather and paper
Basic	Inks, paper, polyacrylonitrile, treated nylon, and polyester
Direct	Nylon, rayon, paper, leather and cotton
Reactive	Wool, cotton, silk and nylon
Sulfurous	Cotton and viscose polyamides and polyesters rarely silk
Vat	Wool and cotton.
Dispersive	Polyamide, acrylic polyester, acetate, and plastics
Mordant	Wool, silk
Pigments	Used in printing processes

I.2.3 Azo dyes

Azo dyes are characterized by the presence of one or more azo groups ($-N = N-$) in their molecule structure. This dyes category is currently the most widely used in terms of applications, accounting for more than 50% of the world's dye production [33]. Azo dyes fall into several kinds of dyes namely basic, acid, direct and reactive, dispersed and mordant dyes [34].

The reactivity of azo dyes depends on different parameters. The first factor is the nature of the substituent in the molecular structure. They can be found in different forms: acid (if the functional groups are in protonated form), basic (deprotonated with free electron pair on nitrogen) or non-ionic depending on the pH values. The basicity of dyes is influenced by additional factors. For example, the presence of acceptors substituents in aromatic rings such as $-Cl$ or $-NO_2$ groups decreases the basicity of the amino groups [35]. The azo dyes also have amphoteric properties if they contain additional acidic groups (hydroxyl) carboxyl or sulfoxyl groups).

These dyes are used in the textile industry for the colouring of polyester, nylon, cellulose diacetate and triacetate and acrylic fibres [36] and are also used as additives in products derived

from the petroleum and in the dyeing of leather, paints, plastics, papers, wood, oils, cosmetics, pharmaceuticals, metals and food.

I.2.4 The hazard and toxicity of dyes

It is estimated that 10-15% of the initial quantities of the azo dyes are lost during dyeing procedures and are discharged without prior treatment in the effluents. The discharge of these wastewaters into the ecosystem without any pre-treatments, is a source of pollution, eutrophication and non-aesthetic disturbance in the aquatic life. It can cause serious environmental problems such as: reduction of the light absorption due to the organisms that inhabit the aquatic environments and the production of different amines under anaerobic conditions.

Dyes are visible in water even at very low concentrations ($<1 \text{ mg L}^{-1}$) and they known as refractory materials that are characterized by high resistance to the biodegradation [37]. Therefore, dyes present a potential bioaccumulation hazard that can affect species at the high end of the food chain including human beings [38]. The toxicity of the different types of dyes has been studied in different research works on aquatic organisms (fish, algae, bacteria, etc.) as well as on mammals [39]. Indeed, it has been proven that some of disperse dyes can cause allergic, dermatological reactions and that the bladder cancer is more prevalent between the workers in textile industry [40]. Most dyes are not initially toxic; however, they can be transformed into even more toxic mutagenic, teratogenic or carcinogenic compounds after their metabolization by micro-organisms present in the environment [29] [41]. In addition, coloring agents have the ability to interfere with the transmission of light in water, blocking the photosynthesis of aquatic plants.

I.2.5 Different methods for dyes removal

Several methods have been used to treat the wastewater and they can be divided into three main types: biological such as enzyme degradation, microorganism), chemical (oxidation, ozonation, electrolysis) and physical techniques (filtration, adsorption, coagulation / flocculation, osmosis reverse) [42].

The conventional biological methods include aerobic and anaerobic process, adsorption by microbial biomass, algae degradation, enzyme degradation, fungal cultures and microbial

cultures. The biodegradation of synthetic dyes by microorganisms is a common technique for wastewater treatment however the processes of the degradation can be very complex since most of synthetic dyes are very stable and resistant to biological degradation [43]. Moreover, instability is one of the major disadvantages in these methods since they deal with living organism [44].

Regarding the chemical processes, the oxidation, the advanced oxidation process, ozonation, electrochemical destruction, Fenton reaction, photo-chemical and ultraviolet irradiation are the conventional chemical techniques applied for dye removal. Though the chemical processes are very effective and capable to eliminate toxic materials they are commercially unattractive because of their high cost, huge electrical energy consumption, specific equipment requirements besides to the generation of toxic by-products [45], [46].

Finally, the conventional physical processes include the adsorption, coagulation or flocculation, ion exchange, irradiation, membrane filtration, nano filtration or ultra-filtration and reverse osmosis. These methods are commonly accomplished straightforwardly by the mass transfer mechanism. Physical techniques are usually the most methods employed for dye removal due to their its simplicity, efficiency and adsorbent regeneration possibility [44].

I.3 Generalities on the adsorption

The adsorption is a surface phenomenon that transfers a substance found in a mobile liquid or gaseous phase to a solid phase [47]. The adsorption will occur when a liquid or gaseous effluent containing a solute is put in contact with a solid that has specific structure with a porous surface. This phenomenon takes place at the interface liquid-solid where the molecules of solute called 'adsorbate' are attracted, then being fixed on the surface of the solid called 'adsorbent' due to intermolecular attraction forces [48]. This process of adsorbate retention on the adsorbent surface is the adsorption. The attractive forces that cause the adsorption can be 'physical' forces or 'chemical' forces [49]. Therefore, it is customary to distinguish two major types of adsorption: physical adsorption or physisorption (also called Van Der Waals adsorption because of the nature of these forces of physical cohesion) and chemical adsorption, or chemisorption [49].

I.3.1 Physical adsorption

Physical adsorption or physisorption is the adsorption provided by the formation of weak intermolecular attraction forces between the adsorbent and the adsorbate, mainly van der Waals forces, electrostatic forces and hydrogen bonds [50]. It is a fast and reversible process since it doesn't cause any modification to the adsorbate molecules. At high relative pressure, generally, physisorption occurs in multilayer (multiple layers) with a low heat of adsorption ranging from 20 to 40 kJ mol⁻¹ and therefore more stable at low temperatures [51].

I.3.2 Chemical adsorption

Chemical adsorption or chemisorption is an adsorption in which the forces involved are much stronger forces than those involved in a physisorption. In this adsorption chemical bonds are formed between the adsorbate and the adsorbent. The bonds can be covalent bonds formed by sharing the same pair of electrons or strong electrostatic (or ionic) bonds. Chemisorption is irreversible since it produces a modification of the adsorbent molecules. This type of adsorption is characterized by an accumulation of molecules adsorbed on a monolayer with a heat of adsorption, relatively high compared to the physisorption and thus can be more stable at high temperatures.

As the contact time progress, the adsorption of the solute on the adsorbent surface tends towards an equilibrium after which the concentration in the liquid phase will be constant and the solute is no more retained by the adsorbent.

I.3.3 Adsorption for dye removal

The adsorption method has been widely applied for the elimination of different pollutants especially dyes. The adsorption was found to be a method of choice for dyes removal, compared to other water treatment techniques, due to its flexibility and simplicity of design, initial cost and ease of use. Selective and non-selective adsorption has been the subject of large range of studies.

The choice of the adsorbent is the most crucial issue in the adsorption process [52]. To overcome this issue, numerous studies have been performed to discover and develop cheap, innovative and eco-friendly adsorbents with high efficiency. Several adsorbents were applied

for the removal of dyes from waste water such as activated carbon chitosan [53], [54] alumina [55]–[57], Silica Gel [58], [59], graphene oxide, [4], anthracite [60], bentonite [61], [62], fly ash [63], Sugar Cane Dust [64], [65].

Usually, in the process of dye molecules adsorption several steps are involved [17]. First, the dye molecule will diffuse through the bulk of solution. The second step involves the diffusion of the dye molecule from the bulk solution to the surface of the porous solid through the boundary layer (film diffusion). The next step is the internal dye molecule diffusion (diffusion of the molecule into the pores or in the pores of the adsorbent particle). Finally, the adsorption step takes place where the dye molecules will be attached to the adsorbent surface [66].

I.4 Layered double hydroxides (LDH)

I.4.1 Definition and structure

Layered double hydroxides (LDH) are a class of the anionic clay minerals. They are also known in the literature as Hydrotalcite-like compounds (HTLc) by analogy to the first natural mineral discovered in this family [67]. They are presented as platelet-shaped crystallites corresponding to the stacking of a certain number of sheets.

The structure of LDH is formed by a stack of $\text{Mg}(\text{OH})_2$ brucite layers which are based on the superposition on octahedral units where the Mg cations are surrounded by six hydroxide ions (OH^-). These octahedral units share their edges so that each OH ion is shared between three octahedra to build 2-dimensional brucite layer $\text{Mg}(\text{OH})_2$ [68]. Then, the layers are stacked to form a three-dimensional structure with electrostatic interactions and hydrogen bonds between the layers [69]. In each layer, a fraction of the divalent metal cations is substituted by trivalent metal ones resulting in positively charged layers. To compensate the positive charges of the stacked layers, anion species and water molecules are intercalated in the interlayer spaces forming the general structure of the layered double hydroxides.

The cohesion of the LDH structure is due to electrostatic interactions between the oxygenated metal sheets and the anions as well as to the network of hydrogen bonds established between the water molecules, the interlamellar anions and the hydroxyl groups of the leaflets [70]. The general structure of LDH could not be described until the 1960s [71], [72]. Schematic representation of the general structure of LDH is shown in Figure.I.2 [73].

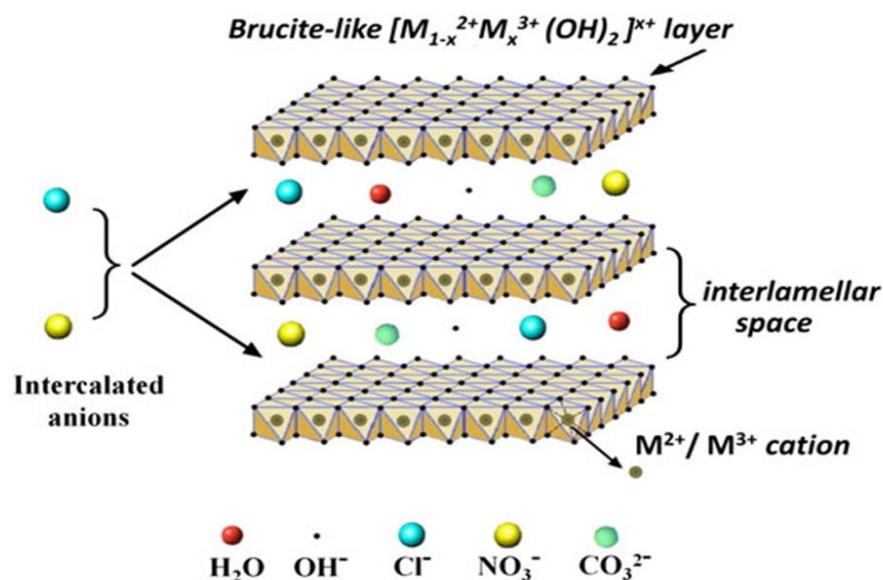
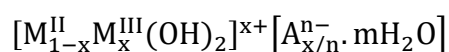


Figure.I.2. Schematic representation of the general structure of LDH

The general formula of the layered double hydroxide can be written as follow:



M^{II} is a divalent metal cation and M^{III} is a trivalent metal cation. A^{n-} is an anion of valence n . x is the fraction of the trivalent cation : $x = M^{III}/(M^{II}+M^{III})$ and m is the number of water molecules: $m = 1 - 3*x/2$ [74], [12].

For natural compounds, the ratio M^{II}/M^{III} is generally close to 3, so the fraction of the trivalent x is of the order of 0.25. In synthetic materials, the relative proportions of di- and trivalent cations may vary, and x generally takes values between 0.20 and 0.33. M^{II} could be Cu^{2+} , Zn^{2+} , Ni^{2+} , Co^{2+} , Fe^{2+} , Ca^{2+} ...etc, M^{III} could be Cr^{3+} , Fe^{3+} , Co^{3+} , Al^{3+} ...etc and A^{n-} could be Cl^- , NO_3^- , SO_4^{2-} , CO_3^{2-} ...etc.

I.4.2 Methods of synthesis

Several methods have been successfully used to synthesize layered double hydroxides. The methods of LDH synthesis can be either direct or indirect. The direct methods comprise the coprecipitation, sol-gel synthesis, salt-oxide method, electrochemical synthesis, and *in-situ* film growth. The indirect methods are rather additional treatments and modifications of pre-synthesized LDHs, they include anion exchange, LDH reconstruction, and delamination [75]. Hereafter, three of the mostly used synthesis methods.

I.4.2.1 Coprecipitation

The coprecipitation method is the simplest and the most commonly used method for LDH preparation. It is often coupled with hydrothermal treatment to improve the crystallinity and the size of LDH particles [76]. This method consists in causing a simultaneous precipitation of divalent and trivalent metal cations by addition of an alkaline species to a solution of corresponding salts taken in adequate proportions. In order to successfully synthesize the LDH by coprecipitation method it is required to perform the synthesis operation under the conditions of supersaturation which are attained by controlling the pH of the reaction mixture. In particular, it is necessary to operate at a pH higher than or equal to the one at which the most soluble hydroxide is precipitated to ensure simultaneous precipitation of all desirable metal cations [77]. There are two types of the coprecipitation method usually used: precipitation at low supersaturation and precipitation at high supersaturation

Precipitation at low supersaturation is performed by drop wise adding the mixed solutions containing divalent and trivalent metal salts in the chosen ratio, simultaneously, with an alkaline solution into a reactor containing an aqueous solution of the desired interlayer anion. The pH of the reaction mixture is maintained at a selected value leading to the co-precipitation of all desired metallic cations. The general process of this method is established by Miyata [78]. The coprecipitation at low supersaturation conditions allows to control the M^{II}/M^{III} ratio of the resulting LDH via a precise control of operating pH. Moreover, it usually leads to LDH structure with higher homogeneity and crystallinity comparing to LDH obtained under high supersaturation conditions, [78].

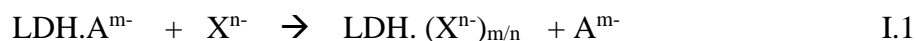
The precipitation at high supersaturation is performed by the addition of a mixed M^{II}/M^{III} salts to an alkaline solution containing the desired interlayer anion. Precipitation at high supersaturation technique generally gives rise to materials with less crystallinity, because of the high number of crystallization nuclei. Furthermore, the formation of impurity phases, therefore an LDH with an undesired M^{II}/M^{III} ratio, often results since the precipitation at high supersaturation leads to a continuous change in the pH of the mixture [75].

Thermal treatment performed following coprecipitation may increase the crystallinity of amorphous or badly crystallized materials.

I.4.2.2 Ion-exchange

The ion-exchange method is generally applied on a pre-synthesized LDH. It is based on the high anionic exchange capacity shown by these materials. It is generally useful when the divalent/trivalent metal cations or the anions are unstable in the alkaline solution, or when LDHs have larger affinity to the guest anions compared to the intercalated anions priorly present in the LDH structure. Miyata proposed an order of anion selectivity: $OH^- > F^- > Cl^- > Br^- > NO_3^- > I^-$ and $CO_3^{2-} > C_{10}H_4N_2O_8S^{2-} > SO_4^{2-}$ [78]. However the anion exchange process is strongly affected by the operating conditions such as pH and temperature, for instance the intercalation of CO_3^{2-} anions is favored at higher pH values [79]. This method allows to produce LDHs pillared with specific anion. From a thermodynamic point of view, the ion exchange in LDHs depends mainly on the electrostatic interactions between the positively-charged host sheets and the exchanging anions and, slightly, on the free energy involved in the changes of hydration [80]. Figure.I.3 illustrates a schematic representation of the anionic exchange phenomenon [81].

The general process of the anion exchange method can be described by the following equation.



Based on the mass action law, working in excess of anions guest (X^{n-}) will favor the exchange reaction of outcoming anions (A^{m-}) to generate the fully exchanged phase $LDH.(X^{n-})_{m/n}$.

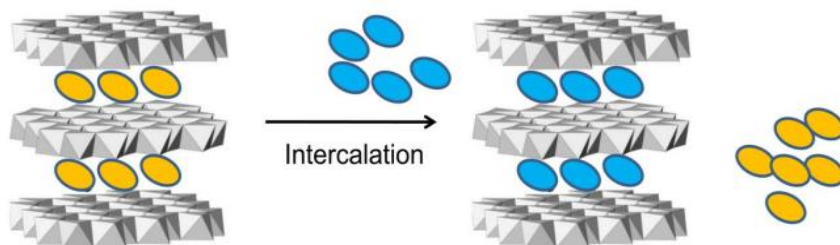


Figure.I.3. Schematic representation of the anion exchange property of the LDH

I.4.2.3 Reconstruction.

The LDH has a unique property known as reconstruction. After undergoing a thermal treatment or calcination the layered structure of the LDH is collapsed and mixed oxides are obtained. The destruction of the LDH structure under high temperatures is mainly caused by the dehydration and the departure of the intercalated anions. Put in contact with solution containing guest anions, the calcined LDHs are able to recover their original layered structure and form a new LDH phase. This phenomenon is called the "memory effect" [82].

Miyata et al [83] were the first to describe the ability of LDH phases to recover their original structure after calcination under certain heat treatment conditions. Figure.I.4 gives a schematic representation of the reconstruction phenomenon of the LDH [84].

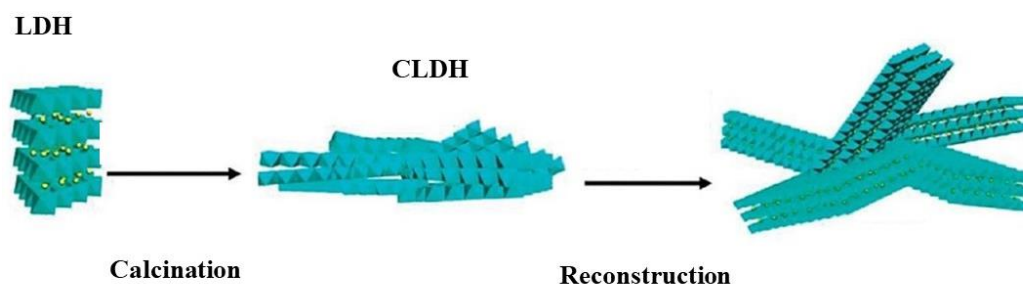


Figure.I.4. schematic representation of the reconstruction phenomenon of the LDH

I.4.3 Applications

Layered double hydroxides have many potential applications due to their varied compositions, ease of synthesis, low cost, low toxicity and high specific surface area. LDHs have been used in a wide range of important areas, e.g., catalysis, photochemistry,

electrochemistry, polymerization, magnetization, biomedical science, and environmental application [77], [85]. As catalysts, LDHs have been applied in catalyzing the production of basic chemicals [86], acid–base processes [87], redox process [88]. In electrochemistry LDHs have been investigated for their use as new modified electrodes [89]. LDHs have also great applications in medicine such as in pharmaceutical formulations [90] and delivery systems [91]. In industrial applications the LDHs have been used as heat retention additives [92] stabilizing agents [93] and flame retardants [94].

LDHs have been widely used as adsorbent for the removal of several types of contaminants from wastewater: dyes [10], chlorophenols [17], heavy metals [9],[18], and monoatomic anions [19]. Recently, great interest has been given to the preparation of different types of composites based on LDH and the investigation of their potential in wastewater treatments. Bin et al [95] have used magnetic and recyclable calcined CoFe-LDH/g-C₃N₄ composite for the removal of hexavalent chromium (VI), Zheng et al [96] have applied graphene oxide-Ni Fe LDH composite for the removal of congo red, methyl orange and Cr(VI) ions. Karthikeyan and Meenakshi [97] have investigated the capacity of Zn–Al LDHs/activated carbon composite to adsorb phosphate and nitrate ions from aqueous medium.

I.4.4 Removal of dyes using LDH in literature

Several studies have been published on the adsorption of dyes on LDHs. Large varieties of LDH have been synthesized for that purpose. The most of the reported LDHs were binary or ternary LDH. The parent material of anionic clays is $\text{Mg}_6\text{Al}_2(\text{OH})_{16}\text{CO}_3 \cdot 4\text{H}_2\text{O}$ which is naturally occurring hydrotalcite. Therefore the first synthetic LDH was Mg/Al LDH reported by Feitknecht [98]. Then, hundreds of metal cations have been used in the synthesis of different LDHs. El Gain et al [99] have synthesized Mg-Al-CO₃ and applied it for the removal of indigo carmine dye. De Sá et al [10] have prepared binary LDH including Ca/Al metal cations and investigate its application as adsorbent for sunset yellow FCF food dye. Ni et al [100] investigated the removal of methyl orange using Zn/Al LDH. Benselka-Hadj et al [74] and Guo et al [101] have studied the adsorption of Orange G and acid brown 14 respectively onto calcined and uncalcined Mg/Fe LDH. Both uncalcined and calcined Mg/Ni/Al hydrotalcites were applied for the adsorption of methyl orange and reported by Zaghoulane et al [102]. Dos Santos [103] et al and Lafi et al [104] have reported the application of Mg/Al LDH in the

elimination of Acid Green 68:1 and congo red respectively. Lu et al [105] demonstrates the high performance of synthesized Ni/Fe LDH in the removal of methyl orange dye.

Recently, Li et al [106] have proved the efficiency of Mg/Al LDH, synthesized by an ethanol–water mediated solvothermal method, to remove the congo red from aqueous solution. Chebli et al [13] have studied the adsorption of the acid red 66 dye on calcined and non-calcined Mg/Al LDH. Lei et al [107] have reported a very high capacity of adsorption of the congo red on Ni/Mg/Al LDH. El-Hassani et al [108] have discussed the application of Ni/Al LDH with different morphologies as adsorbents for the methyl orange. Li/Al synthesized via mechanochemical route have been reported by Qu et al [109]. Bharali and Deka [110] investigated the removal of the congo red on sonochemically synthesized Ni/Al LDH. De Sontos et al [111] have demonstrated the high adsorption capacity of the calcined Mg/Al to remove the acid yellow 42 dye from solutions.

Tiar et al [112] have reported the synthesis of quaternary LDH based on Zn/Mg/Ni/Al metal cations. Bharali and Deka [113] have also studied the removal of different dyes (methyl orange, bromothymol blue, erichrome black-T, congo red, methylene blue and rhodamine B) on synthesized Cu/Mg/Al LDHs with different Cu/Mg molar ratio. An other work that deals with quaternary LDH (Co/Ni/Zn/Al LDH) was reported by Linares et al [114].

I.5 Zeolites

I.5.1 History

The notion of zeolite was mentioned for the first time in 1756 by the Swedish mineralogist Cronsted [115]. These minerals have a particular property of releasing water under the effect of heating which gives the impression of being boiling. Based on this property they have been named zeolite referring to their Greek name zeolithos: zeo “boil” and litos “stone”. Since then, zeolites are considered as a separate group of minerals, composed by a large variety of species (about 50) [116]. Studies and applications of zeolites have increased considerably in recent decades and a large number of publications and patents have been established [117]. Natural zeolites have been increasingly substituted by synthetic zeolites and recently more than 170 different crystalline structures of the material are known [118].

I.5.2 Definition and structure

Zeolites are microporous crystalline materials [119]. They belong to the family of tectosilicates. Their three-dimensional crystalline structure results from the arrangement of TO_4 tetrahedra (generally T is Si or Al) connected through bridging oxygen atoms. These connections must respect Loewenstein rule which states that the same oxygen atom cannot be bound to two aluminum atoms. The aluminum atom of valence (III) is surrounded by four oxygen atoms where each oxygen atom is related to an atom of Al and Si simultaneously. So, in the case of the AlO_4 tetrahedron, the Al ends up with a negative charge on it. Therefore, the electroneutrality of the crystalline structure $(\text{AlO}_4)^-$ is ensured by cations, generally by alkaline cations. These basic units come together to form a three-dimensional network by repetition of elementary mesh $(\text{SiO}_4)/(\text{AlO}_4)^-$ [116]. This framework involves regular channels and cavities that give the porous properties to the crystalline zeolite. The open framework may contain salts and water molecules in addition to the compensation cations. Moreover, the framework is characterized by its rigidity which makes it unaffected if it adsorbs or desorbs water. The general structure of the zeolite is represented in Figure.I.5.

The unit cell forming the zeolite is generally given by the following formula [120].

$$M^{+}_{2/n} O Al_2 O_3 x Si O_2 y H_2 O \quad \text{I. 2}$$

M: the exchangeable cations, (generally is alkaline or alkaline-earth cation although it can be another metallic, non-metallic, or organic cation)

n: the valence of the cation M.

x: the number of silicon atoms ($X \geq 2$ since the alumina tetrahedron does not occupy adjacent sites)

y: the degree of hydration.

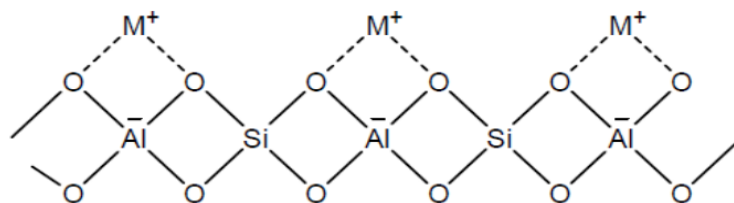


Figure.I.5. General structure of zeolite

The amount and the location of Al affect strongly the properties of the zeolite produced. The lowest value of Si/Al ration in the zeolite structure is limited to the unit, since the alumina tetrahedra (AlO_4)⁻ cannot occupy adjacent sites, while the highest value of the ratio can go to ∞ where the compound is SiO_2 [119].

The characteristic arrangements of tetrahedra giving rise to several frameworks and therefore different types of zeolites. The sixth edition of the Atlas of Zeolite Framework Types publication has listed 176 different framework structures. Each framework structure is represented by a three letter code proposed by the commission of International Zeolite Association [118]. Recently more than 230 type of framework structures were described in the Database of Zeolite Structures by the same association [121]. Figure.I.6 represents some common zeolite framework structures while Table.I.4 provides some descriptions and examples of those frameworks [118].

Table.I.4. Common frameworks with their idealized cell parameters and examples of zeolites.

Framwork	Idealized cell		Zeolite
	Shape	Parameters	
LTA	Cubic	$a = 11.9\text{\AA}$	Zeolite-A, SAOP-42
FAU	Cubic	$a = 24.3\text{\AA}$	Faujasite, Na-X, Na-Y, SAPO-37, ZSM-20
GIS	Tetragonal	$a = 9.8\text{\AA}, c = 10.2\text{\AA}$	Gismondine, Na-P, Na-P1, Na-P2, SAPO-43
SOD	Cubic	$a = 9.0\text{\AA}$	Sodalite, hydroxysodalite, AIPO-20
CHA	Trigonal	$a = 13.7\text{\AA}, c = 14.8\text{\AA}$	Chabazite, AIPO-34, SAPO-34. SAPO-47
ANA	Cubic	$a = 13.6\text{\AA}$	Analcime, AIPO-24,
EDI	Tetragonal	$a = 6.9\text{\AA}, c = 6.4\text{\AA}$	Edingtonite, K-F, Linde F, Zeolite N
MER	Tetragonal	$a = 14.0\text{\AA}, c = 10.0\text{\AA}$	Merlinoite, K-M, Linde W, Zeolite W

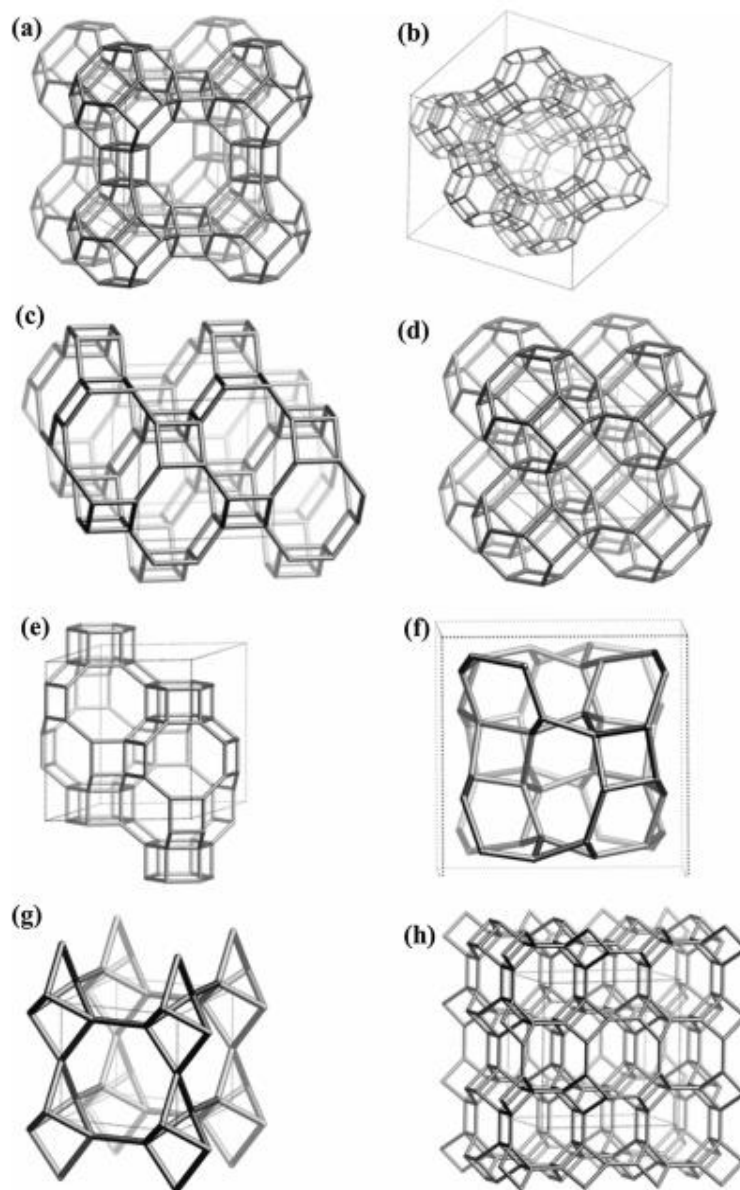


Figure.I.6. Structure of some common zeolites frameworks (a) LTA, (b) FAU, (c) GIS, (d) SOD, (e) CHA, (f) ANA, (g) EDI and (h) MER

Among the large number of zeolite types, we distinguish the P-group zeolites. Several researchs have been interested this type of zeolite due to their water-softening properties and also ease of preparation comparing to other types. Zeolite P has a Gismondine-like framework

(Figure.I.6 (c)) with intersecting channels of 0.31×0.44 nm and 0.26×0.49 nm along [100] and [010] directions, respectively [122]

Two polymorphs of zeolite P are known at room temperature: cubic (Pc) and tetragonal (Pt). The zeolite cation exchange capacity has been widely studied. Na^+ was the most used exchanged ion other ions have been also reported: Ca^{2+} , Mg^{2+} , Li^+ , Zn^{2+} , 1°Cs^+ , Sr^{2+} and Ba^{2+} .

I.5.3 Properties and applications

The zeolites have a wide range of applications in the industry as selective heterogeneous catalysts, as ion exchangers, as adsorbents, they have also great applications in separation processes especially in petrochemical and fine chemical industries. These considerable applications of the zeolites in different domains are owe to their structure and composition that give them special properties. Recently, zeolites are finding new applications in electronics, magnetism, chemical sensors, medicine [123].

I.5.3.1 Adsorption and molecular sieve

In the normal state, the zeolites are saturated with water which is found inside the channels and cavities of the crystal lattice. Water molecules can be removed and replaced by molecules of sizes smaller than the pore size without destroying the structure. However, it is the discovery of their selective adsorption properties of organic molecules that has led to the expansion of work on zeolites. The adsorption properties of zeolites are essentially due to their large specific surface area, the important size of the pores and the existence of an electric field within the cavities of the zeolite structure (due to the presence of cations) resulting in a high affinity for the polar molecules [119]. The first use of zeolites as adsorbents in the drying and purification of refrigerant gases and natural gases dates back to 1955 [124].

Moreover, the porosity of a zeolite allows the selective separation of related organic molecules. Depending on its structure, the zeolite has the possibility to fix, selectively, many compounds. This property is known as molecular sieve[125]. The porous system of a zeolite can be mono- (1D), bi- (2D) or three-dimensional (3D), and each unique system is designated by its topology [126]. Molecular sieves are classified, based on the pore diameter dimensions,

into small, medium, large, and ultra-large pores. The openings of the channels or pores are generally characterized by the number of the elements T forming them (for example, 8MR (8-member ring) means that the pore comprise eight tetrahedrons as in the case of the zeolite A.

These properties depend largely on the shape and size of the pores, the nature of the compensation cation and the hydrophobic / hydrophilic character of the mineral framework. The latter can be modified by changing the ratio Si/Al; an increase in this ratio makes it possible to increase the hydrophobicity of the zeolite, leading to greater selectivity for organic molecules

I.5.3.2 Ion exchange

The presence of aluminum in the framework in substitution of the silicon induces a negative charge. The cations that balance the negative charge of the zeolite's framework are often alkaline or alkaline-earth. The most frequently used mineral cation is the sodium Na^+ . The presence of these cations gives them remarkable ion exchange properties. The exchange capacity of a zeolite can be defined as the amount of cations could be retained per gram of zeolite. The more the zeolite is rich in aluminum, the greater is its exchange capacity. Zeolites are then widely used as cation exchangers in several applications such as:

- water softeners: replacing the Mg^{2+} and Ca^{2+} ions in the aqueous solutions by Na^+ ions contained in the zeolite [127].
- the treatment of radioactive effluents by retention of cesium (Cs^+) or strontium (Sr^{2+}) [128].
- the removal of NH_4^+ ions in wastewater.

The first works describing this characteristic of zeolites go back to 1858 [129].

I.5.4 Methods of zeolite synthesis

I.5.4.1 Hydrothermal synthesis using pure chemicals

The hydrothermal synthesis method is the basic way used to prepare the zeolites. Generally, a hydrothermal synthesis is conducted in closed system under high temperature ($\geq 100^\circ\text{C}$) and high pressure ($\geq 1\text{bar}$). Zeolites often crystallize, under hydrothermal conditions, at a temperature below 250°C for a duration ranging from a few hours to a few days [123]. The reaction mixture called hydrogel, or more commonly gel, must contain:

- Source materials: the sources of the different elements (Si, Al ...) forming the zeolitic framework.
- A structuring agent: source of the compensating cation (alkaline or alkaline earth...)
- A solvent (most often water).

The different ingredients are mixed at low temperature ($< 60^{\circ}\text{C}$) to obtain the "synthesis gel". A gel is obtained because of the high concentrations of reagents, Inside the gel, the aluminum and silicon monomers are in equilibrium with condensed aluminosilicate units. In a second step, the synthesis mixture is brought to its crystallization temperature. It is heated to reduce the activity of the water and to shift the equilibrium of condensation of the silica. During this process the oligomers of silicon and aluminum continue to dissociate, increasing the number of monomers in solution. Prior to the crystallization of zeolites, there is an induction period called nucleation. During this period the crystal nuclei, poly-silicate structural units and aluminosilicates, are formed and become stable beyond a certain size from which crystallization propagates. Indeed, it is a process of nucleation and growth. Finally, depending on the nature of the zeolite desired to be prepared, the crystallization will be completed after few hours or after few days. The crystals formed are then washed with water and dried [123], [130].

I.5.4.2 Synthesis of zeolite using waste materials

The synthesis of zeolitic materials from industrial wastes has many advantages comparing to their direct synthesis from pure chemicals. In fact, the use of industrial wastes for the preparation of zeolite contribute in diminishing the waste amount discharged in the environment and in by-products valorization. There are different methods proposed in the literature for the reuse of the fly ash. However, those methods that convert the fly ash into zeolitic compounds offers the greatest benefits. In fact, this process transforms the waste ash materials from disposal sites into secondary products that are useful in different environmental applications [131]

a. Coal fly ash waste (CFA)

Over the years, there has been a growing increase in the production of waste ash from different sources (e.g., biomass, animal, coal, industrial, and municipal solid waste) as well as

from traditional and renewable energy technologies. This has generated challenging environmental problems due to the large amount of material disposed of in landfills.

Coal and biomass fly ash are the two main waste products produced, respectively, from the combustion of fossil fuels and alternative natural sources of energy [132]. Conversion to zeolite provides the greatest advantages among the various methods suggested for the reuse of fly ash. This method allows the conversion of waste fly ash from disposal sites into secondary products useful for large applications in different domains ranging from environmental mitigation to catalysis. There are two main categories for coal ash: bottom ash and fly ash. The residual coal ash that settles on the bottom of the boiler after the combustion process is called bottom ash. On the other hand, the finer coal ash particles that floats into the exhaust chimneys and collected by electrostatic precipitators during the coal combustion process is called coal fly ash.

CFA's major chemical components and properties are heavily influenced by the coal burning properties, combustion method, heating and cooling regimes in the coal boiler. CFA can contain various alumina and silica phases, including mullite, quartz, hematite, and calcite. Usually, CFA consists of 90%–99% inorganic material and 1%–9% organic material. The inorganic material contains 34%–80% of amorphous materials and crystalline phases (e.g. quartz, mullite, hematite, goethite, and calcite) [131].

In CFAs, two main classes can be distinguished: Class F and Class C. the class F is generated primarily by higher-ranked coal such as anthracite and bituminous coal, mainly, consists of quartz and mullite crystalline compounds and its is characterised by containing less than 20% of CaO, while, the Class C is composed of quartz, tricalcium aluminate, calcium silicate, and tetracalcium aluminosilicate and it is characterised by containing more than 20% of CaO [133], [134] [135].

Despite the worldwide variability of CFA composition, zeolitic compounds were successfully synthesized from CFA in various countries among them, for example: Australia [136], United States [137], Canada [138], [139], Bulgaria [140], Italy [141], Spain [142], South Africa [143].

b. Conversion of CFA into to zeolite

The main components of CFA and zeolite are Al and Si [144]. Nevertheless, the crystalline structure is the main difference between the two. Zeolite has a well-defined crystalline structure, while CFA is an amorphous compound. The similarities in the main composition between CFA and zeolite, make of the CFA potential resource for zeolite synthesis [145]. Aluminosilicates, which are the main component of fly ash, are converted into zeolite crystals by hydrothermal reaction in alkaline solution. The aluminosilicates dissolve first into the reaction mixture and then cluster, nucleate and grow as crystals on the CFA surface. The conversion of CFA into zeolite occurs mainly in four stages illustrated in Figure.I. 7 [146]. Amorphous aluminosilicates present in CFA are extracted and dissolved into the reaction mixture. The aluminosilicates' dissolution dictates not only the amount of conversion but also the conversion rate [145]. The concentration of Si and Al in the reaction mixture may vary locally. However, particular type of zeolite can be produced by adjusting the average ratio of Si/Al through the addition of pure chemicals. The synthesis of zeolite from CFA is different from the normal direct preparation methods since the source of Si and Al in CFA are relatively less reactive. Moreover the CFA

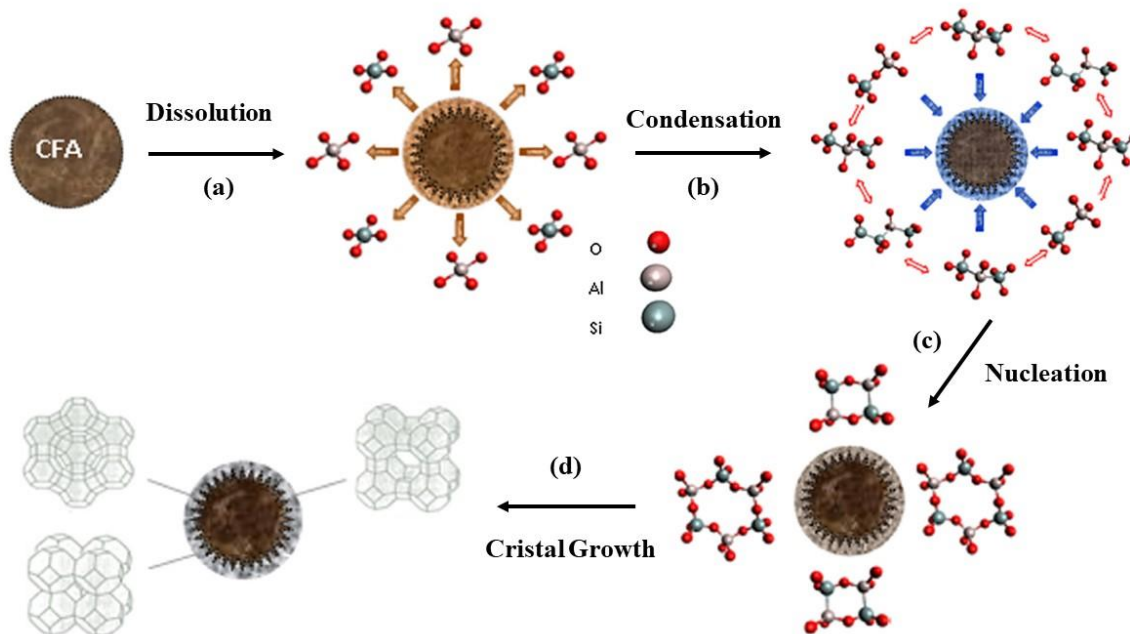


Figure.I. 7. Schematic illustration of zeolitization process of CFA particle (a) Dissolution of Al and Si content of CFA into the solution (b) Condensation of Al and Si polymers (dimers, trimers etc.) on the surface of CFA particle (c) Nucleation of zeolites (d) Zeolite crystal growth.

contains other phases that can affect the crystallization process [145]. The lower reactivity of the Al and Si source present in the CFA may be due to the aluminosilicate dissolution issue in reaction mixture.

I.5.4.3 Effects of zeolitization parameters

Several factors, such as the composition of the raw CFA, decide the formation of a particular zeolite. Hereafter, the role of concentration of cations and anions, alkalinity of the aqueous phase, and the temperature, in the formation of zeolite are explained.

a. Role of cations and anions

The existence, the concentration and the type of the different alkali metal cations in the reaction gel may direct the crystallization process to the formation of specific zeolite frameworks. The final zeolite structure is heavily influenced and determined by the interactions between the negatively charged aluminosilicates and cations in the solution phase. Cationic species' tendency and ability to favor one zeolite structure over another is called "structure-direction". Several organic compounds are also used as structure-directing agents [147]. Murayama et al. [148] observed that Na^+ cations have a significant role in the crystallization zeolite of Na-P1. Na^+ cations accelerate the reaction process from 24h using K^+ cations only to 3h in presence of Na^+ ions. Moreover, It was observed that the addition of anions such as F^- and Cl^- produce zeolite with higher crystallinity and CEC [149].

b. Role of alkalinity

The zeolitization conversion percent and the conversion rate are directly related to the amount of the amorphous aluminosilicates (in CFA) dissolved into the solution [145]. The dissolution of Si^{4+} and Al^{3+} present in CFA mainly depends on the alkalinity of the solution [69]. Higher pH is favorable for the dissolution of Quartz crystal within CFA however further increase in pH directs the reaction towards the formation of hydroxysodalite [148]

c. Role of the Temperature

For a given composition of the gel, the crystallization temperature determines the type of zeolite formed. Moreover, its elevation favors the solubility of the silicate species and thus increases the supersaturation of the solution, the transport of dissolved species will therefore be

faster and the crystallization times shorter. The temperature can influence the respective growth rates of each face, and consequently the morphology of the crystal.

I.5.4.4 Methods of zeolite synthesis in literature

The composition of the CFA rich in silicate and aluminate compound, gives raise to a wide range of studies aiming to valorize the waste CFA by its transformation into value added materials. The zeolitization of the CFA has attracted considerably the attention of researchers. Several ways of CFA conversion into zeolitic materials has been reported in thousands of researches. Basically, the conversion of CFA is performed using the conventional direct way. In this method the CFA is mixed with an alkaline solution which serves to extract Si and Al from the deep coal fly ash particle and being dissolved in the reaction mixture. A desired type of zeolite can be obtained by adjusting the Si/Al ratio by adding pure chemicals. Using this method of synthesis several types of zeolite were reported. zeolite A [150]–[152] Zeolite X [137], [152], [153] Zeolite P [148], [154], [155] chabazite [156], [157] hydrosodalite [156] analcime [158].

Other methods of CFA zeolitization were developed including the pre-treatment of the CFA prior the hydrothermal conversion, or the integration of other mode of energy such as microwave and ultrasound. Microwave assisted hydrothermal conversion, Ultrasound assisted hydrothermal conversion, Fusion followed by hydrothermal treatment (indirect conversion), Fusion followed by ultrasound assisted hydrothermal conversion and Fusion followed by microwave assisted hydrothermal conversion. Different researchers for instance Querol et al.[142], Inada et al.[159] and Aldahri et al.[138] have reported a Microwave assisted hydrothermal conversion method where different types of zeolite have been synthesized from CFA using the microwave induced heating. Aldahri et al. have reported a successful conversion of the coal fly ash into zeolite P using hydrothermal method followed by sonochemical has been also reported in literature by [160]. Shigemoto et al. [161] added a pre-treatment step of the coal fly ash which consists on fusion of CFA with NaOH at high temperature. The induction of the fusion step conducts to the dissolution of more Al and Si and thus enhance the ratio of conversion. Bukhari et al.[162] have reported a zeolite successfully prepared using fused CFA with NaOH followed by microwave-assisted hydrothermal conversion. Musyoka et al. have

succeeded to convert fused CFA into zeolite A by mean of ultrasound assisted hydrothermal method.

I.6 Introduction to the Response Surface Methodology (RSM)

In chemical engineering, we are often required to select (choose) the conditions of the given process in order to produce a desired response. When we are interested to obtain the maximum (best) possible response, we refer to this selection process as *optimization*. Generally, the study of a chemical process is carried out by monitoring the influence of one factor (or variable) at a time. To do that, only the parameter or variable in interest is changed while others are kept constants. However, the major limitation of this one-variable-at-a-time approach is the fact that it does not include interactive effects between the variables of the process. In fact, the optimum set of variables (for the whole process) may differ from the collection of the variables that are obtained by maximizing the response for each variable using the one-variable-at-a-time approach [163]. Moreover, this one-factor optimization requires a large number of experiments necessary to conduct the research study, which leads to an increase of time, effort and expenses (caused, for example, by the increase in the consumption of reagents and materials).

In order to overcome these limitations, different multi-variables (also referred to as multivariate) optimization techniques have been proposed in the literature. One of the most successfully used multivariate optimization techniques is the response surface methodology (RSM), which was introduced by George E. P. Box and K. B. Wilson in 1951 [164]. The main idea of RSM is to use a sequence of specifically chosen designed experiments to obtain an optimal response by fitting a polynomial equation to the experimental data, which must describe the behavior of a data set as close as possible. The objective in the RSM approach is to simultaneously optimize the values of the important variables to attain the best system performance. Although, originally, Box and Wilson suggest using a second-degree polynomial model to do this, polynomials with different degrees can be used. Nevertheless, polynomials with first- and second-degree are more suitable for optimization as most of the analytical optimization algorithms are proven to converge well for second degrees.

The first step in RSM consists on the selection of the experimental variables, also called factors, which represent the independent variables of the process (variables that can be changed

independently of each other). Typical independent variables comprise the pH, temperature, reagents concentration, microwave irradiation time, flow rate, temperature, among others. The selection of the important factors is done through screening studies and the delimitation of the experimental region, according to the aim of the study and the previous experience of the investigator. However, since many variables may affect the response of the process studied while it is practically impossible to identify and control the small contributions from each one, it is usually necessary to select only those that have a major effect on the process.

The measured values of the experimental results (wanted to be studied) are called responses. For *example*, the adsorption capacity, recovery of an analyte, the conversion ratio and efficiency of removal, among others, are considered as responses. Once the experimental data are obtained (from the selected experimental matrix), the data are fit to a polynomial function using mathematic–statistical analysis.

To sum up, the steps to be taken during an experimental design process are as follows:

- Selecting the independent variables (factors) that have major effects on the process
- Choosing the appropriate experimental design and carrying out the experiments according to the selected experimental matrix.
- Fitting the experimental data to a polynomial function.
- Evaluating of the model's fitness.
- Verifying the necessity and possibility of performing a displacement (other experiments) in direction to the optimal region.
- Obtaining the optimum values for each studied variable.

I.6.1 The Experimental design

Before starting the application of the RMS methodology, it is important to choose the so-called experimental design. Experimental design is a specific set of experiments defined by a matrix composed of different combinations (values) of the variables studied. The experimental design is defined over an experimental domain which is the domain defined by the minimum and maximum limits of the experimental variables used in the process. Experimental designs for first-order models (e.g., factorial designs) can be used when the data set does not present curvature [165]. However, to approximate a response function to experimental data that cannot

be described by linear functions, experimental designs for quadratic response surfaces should be used, such as three-level factorial, Box–Behnken, central composite, and Doehlert designs.

Some of the experimental designs used in RSM are discussed in this section. These symmetrical designs differ from one another with respect to their selection of experimental points, number of levels for variables, and number of runs and blocks.

I.6.1.1 Full three-level factorial designs

The full three-level factorial design is an experimental design which is usually limited to RSM applications with no more than two variables. In fact, the number of experiments needed for this experimental design is given by the formula I.3.

$$N = 3^k \quad \text{I. 3}$$

where N is the number of experiments and k is the number of variables. When k is greater than 2, the number of experiments N becomes very large and cannot be accommodated in practice. In this case, we need to use a more efficient experimental design with smaller number of experiments. The majority of applications of three-level factorial designs were conducted in the field of chromatography, see for example [166]. Figure.I.8 (a and b) shows the representation of the three-level factorial designs for the optimization of two and three variables, respectively.

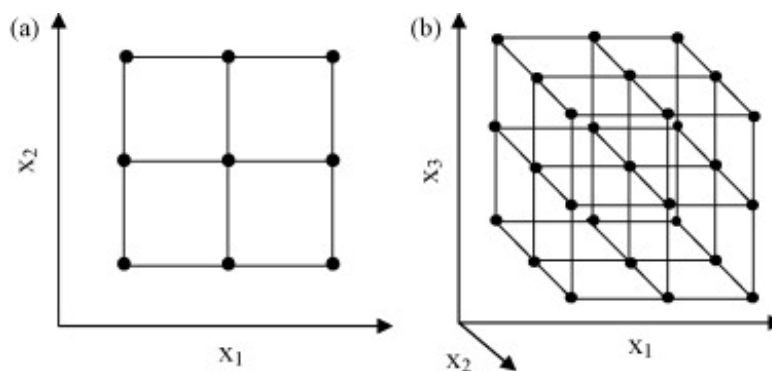


Figure.I.8. Three-level factorial design for the optimization of (a) two variables and (b) three variables

I.6.1.2 Box–Behnken designs

Box and Behnken [167] proposed an approach to select specific experimental points from the three-level factorial arrangement, which allows an efficient estimation of the first- and second-order coefficients of the mathematical model. This design approach is, hence, more efficient and economical (since it requires less experimental points) in the case we have a large number of variables. In Box–Behnken designs [168], the experimental points are selected to lie on the hypersphere centered at the design central point (equidistant points from the central point), see Figure 2 for an illustration with three variables.

Box–Behnken designs require a number of experiments N given by the following formula (I.4).

$$N = 2k(k - 1) + c_p \quad \text{I. 4}$$

where k is the number of variables and c_p is the number of central points.

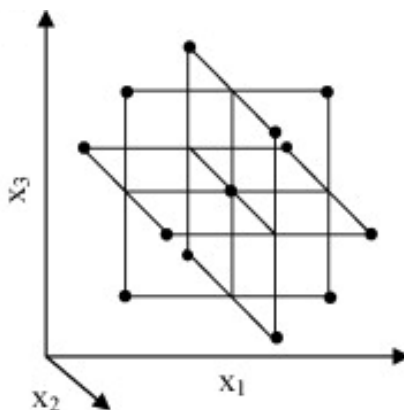


Figure.I.9. Box–Behnken design for the optimization of three variables

As a comparison, for three variables and one central point, Box–Behnken design requires 13 experimental points while the full three-level factorial design requires $3^3 = 27$ experimental points. This experimental design has been applied for the optimization of several chemical and physical processes; however, its application is still much smaller in comparison with central composite design.

I.6.1.3 Central composite design

The central composite design was proposed by Box and Wilson [169]. This design consists of the following parts:

- a full factorial or fractional factorial design.
- an additional design, often a star design in which experimental points are at a distance α from its center (called axial points).
- a central point.

The CCD proposes five variation levels for each independent experimental factor: $-\alpha$, -1 , 0 , 1 and $+\alpha$. For n experimental factors, the CCD is characterized by a total number of experiments N given by formula I.5. N is divided into three series of points: factorial (2^n) points, axial points ($2n$) and center points (cp) which is generally chosen to be 6.

$$N = 2^n + 2n + c_p \quad \text{I. 5}$$

Figure.I.10 (a and b) illustrates the full central composite design of two and three variables system.

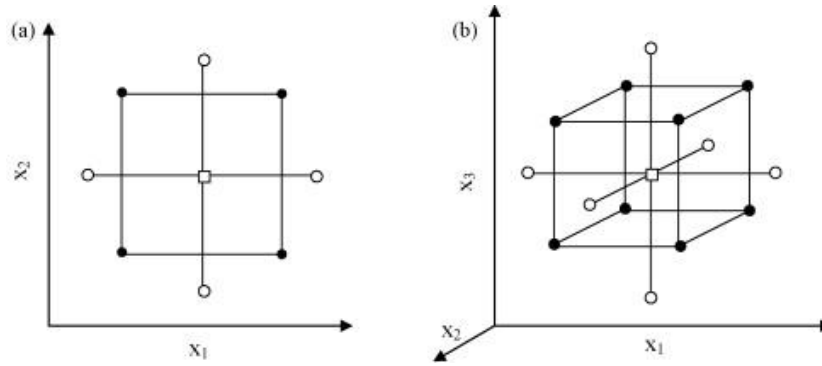


Figure.I.10. Central composite design of: (a) two variables ($\alpha=1.41$) and (b) three variables ($\alpha=1.68$).
 (●) Points of factorial design, (○) axial points and (□) central point

I.6.1.4 Doehlert design

This design approach is developed by Doehlert [170]. This design describes a circular domain for two variables, spherical for three variables, and hyperspherical for more than three variables, which accents the uniformity of the studied variables in the experimental domain.

It presents some advantages, such as requiring few experimental points for its application and high efficiency. In fact, it requires a number of experimental points N given by the formula I.6.

$$N = k^2 + k + c_p \quad \text{I. 6}$$

where k is the number of variables and c_p is the number of central points.

For two factors, the Doehlert design is given by a central point surrounded by six points representing the vertices of a regular hexagon (Figure.I.11). As shown in the same figure, Doehlert design allows for displacement of the experimental matrix to another experimental region using previous adjacent points. Applications of the Doehlert are increasing in recent years, but it is not yet sure whether this design is superior in general to the central composite design.

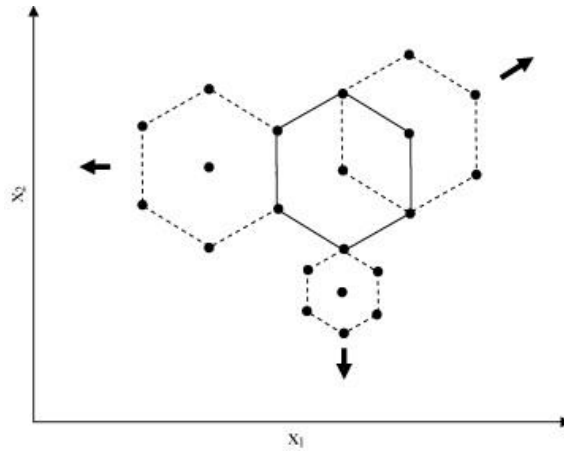


Figure.I.11. Doehlert design for the of two variables

I.6.2 Mathematical modeling and data fitting

The linear model is the simplest polynomial model that can be used in the RMS methodology. The equation of the linear model is given by equation I.7.

$$y = \beta_0 + \sum_{i=1}^k \beta_i x_i + \epsilon \quad \text{I.7}$$

where k is the number of independent variables, β_0 is a constant bias term, β_i represents the coefficients of the linear model, x_i represents the independent variables, and ϵ is the residual associated to the error between the experimental data and the predicted values from the model. For a linear model fitting, the true should not have any important curvature, otherwise the linear model cannot capture this curvature. To evaluate curvature, we usually use instead a second-

order model. A second order model that can capture the interactions between the variables is given by the factorial model in equation I.8.

$$y = \beta_0 + \sum_{i=1}^k \beta_i x_i + \sum_{1 \leq i < j}^k \beta_{ij} x_i x_j + \epsilon \quad \text{I.8}$$

where the parameters β_{ij} represent the interaction coefficients. If we want to capture the curvature as well as the critical point (maximum, minimum, or saddle), we use a general *quadratic model* of the form:

$$y = \beta_0 + \sum_{i=1}^k \beta_i x_i + \sum_{i=1}^k \beta_{ii} x_i^2 + \sum_{1 \leq i < j}^k \beta_{ij} x_i x_j + \epsilon \quad \text{I.9}$$

where the parameters β_{ii} represent the coefficients of the quadratic terms. For quadratic models, the critical point (optimal point) can be characterized as maximum, minimum, or saddle. This point is characterized by equating the first derivative of the mathematical model to zero.

Figure.I.12 illustrates some plots of the quadratic response surface in the optimization of two variables system. Figure.I.12 (a and b) represents surfaces where the maximum point is located inside the experimental region. It is interesting to note that, in surface shown in Figure.I.12 (b), there is a plateau in relation to variable x_2 , indicating that variation of its levels does not affect the studied system.

Surface shown in Figure.I.12 (c) shows that the maximum point is outside the experimental region and that it is necessary to displace, if possible, the initial design to attain it. The surface shown in Figure.I.12 (d) presents a minimum point, and that shown in Figure.I.12 (e) presents a saddle point as the critical point. The saddle point is an inflexion point between a relative maximum and a relative minimum. If the purpose is to obtain a maximum or minimum response to a studied system, the saddle point coordinates do not serve as optimal values. Again, it is possible to find the optimum region through visual inspection of the surfaces.

Fitting the experimental data to the polynomial model (such as second-order polynomial) is called data fitting and it allows to estimate the parameters of the model. This is usually done using the method of least squares (MLS). MLS is a multiple regression technique used to fit a mathematical model to a set of experimental data generating the lowest residual possible. The best fit (in the least-squares sense) is the one that minimizes the sum of squared residuals (a

residual is the difference between an experimental value and the fitted value provided by the model).

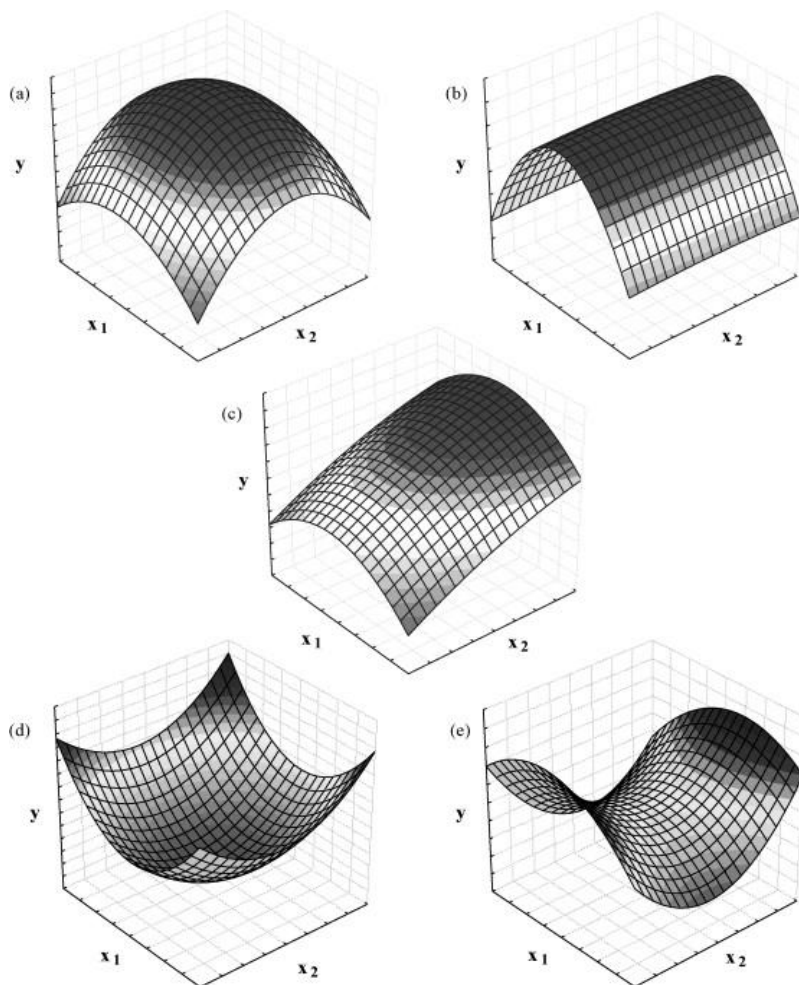


Figure.I.12. Some profiles of surface response generated from a quadratic model in the optimization of two variables. (a) maximum, (b) plateau, (c) maximum outside the experimental region, (d) minimum, and (e) saddle surfaces.

I.6.3 Experimental Design software: Design-Expert 7

In this thesis, we use the Design Expert software to help us with the design and the fitting of our experimental data. The software offers a variety of designs, including factorials, fractional factorials and composite designs. It can handle both process variables, such as contact

time, and also mixture variables, such as the proportion of component in a composite. In Design Expert, the process variables can be either continuous (numeric) or categorical (discrete values). For example, the dye concentration, with concentration varying from 100 to 2000mg.L⁻¹, is a continuous variable. Once we have decided on the type of design that we are going to use, the Design Expert software could be run. There are three main steps:

- Constructing the design: in this step Design Expert allows you to specify the information needed to construct the design (e.g. names and ranges of your variables and degree of replication). At the end of this step, Design Expert gives the design layout which is a list of the experimental settings to be used for each of the experimental runs.
- Evaluating the design: at this step Design Expert allows you to know whether you'll be able to estimate the effects that you're interested in (Alias pattern information). Moreover, Design Expert helps you to estimate the degree of precision of the fitted model that you're likely to achieve.
- Modelling and interpreting the experimental data: at this step, Design Expert offers you a wide range of analytical and graphical techniques for model fitting and interpretation of the obtained results.

Chapter II

Materials and methods

II.1 Introduction

In this chapter we present and describe the main materials and methods used throughout the thesis. First, we represent the reagents used for the synthesis of the different materials as well as the compounds used as model adsorbates: AR66 and CR. Then, the methods of synthesis of materials used as adsorbents: layered double hydroxide (LDH) and zeolite Na-P (ZNa-P) are described. After that, we present the different methods used for material characterization namely XRD, FTIR, TGA/DTA, BET, SEM, XRF and Zeta potential. Moreover, the different models for kinetics and equilibrium studies are discussed. Finally, we present the software used for the investigation of the adsorption of the AR66 on ZNa-P.

II.2 Reagents

II.2.1 Products used for the synthesis of LDH

The chemicals used for LDH synthesis were supplied mainly by Sigma-Aldrich and Alphachem. These are the high purity metal salts mentioned below:

- Magnesium chloride hexahydrate $\text{MgCl}_2 \times 6\text{H}_2\text{O}$
- Copper chloride dihydrate $\text{CuCl}_2 \times 2\text{H}_2\text{O}$
- Aluminum Chloride Hexahydrate $\text{AlCl}_3 \times 6\text{H}_2\text{O}$
- Ferric chloride hexahydrate $\text{FeCl}_3 \times 6\text{H}_2\text{O}$
- Sodium hydroxide NaOH (Alphachem)
- Hydrochloric acid HCl
- sodium carbonate Na_2CO_3

II.2.2 Products used for the synthesis of Zeolite Na-P

The coal fly ash (CFA), used as a raw material to synthesize zeolite Na-P in this research, was collected from the Canadian coal-fired power plant 'Nanticoke' owned by Ontario Power Generation (OPG). The CFA is of class F (CaO content < 20%) and has a composition rich in Silica and Alumina. The whole composition of CFA is shown in Table.II.1. Also, an analytical grade sodium hydroxide NaOH supplied by Alphachem, was used for the synthesis of the zeolite.

Table.II.1. the Chemical and mineral composition of CFA

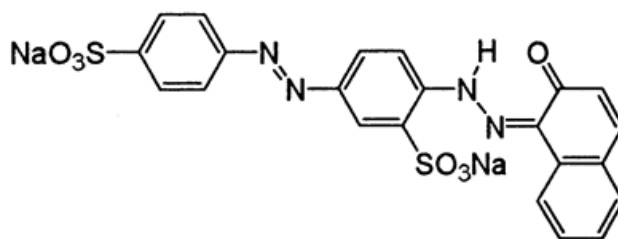
Parameter	Weight percent
Major oxide	
SiO ₂	41.78
Al ₂ O ₃	19.61
CaO	13.64
Fe ₂ O ₃	5.79
MgO	3.23
TiO ₂	1.39
K ₂ O	1.10
Na ₂ O	0.94
P ₂ O ₅	0.71
BaO	0.36
SrO	0.25
Cr ₂ O ₃	0.01
MnO	0.02
Loss on ignition	10.89
Total	99.72
Phases analysis	
Amorphous	88

Deionized water (DI) was used for the preparation of all aqueous solutions.

II.2.3 Products used as adsorbates

II.2.3.1 The Acid Red 66 (AR66)

The Acid Red 66 (AR66) which is used as adsorbate in our study was purchased from Alfa Aesar. This dye is also known as Biebrich Scarlet or either Ponceau BS is an anionic dye belongs to azo dyes class. The product is stable, highly dissolved in water with a solubility higher than 30g.L⁻¹, and it gives a dark red color in aqueous solution. Other properties are given in Table.II.2. It is used in many industries or research purposes. Typically, this dye is not suitable for human consumption or therapeutic use. The AR66 (pK_a=4.5) is hazardous in case of skin contact (sensitizer and irritant) or ingestion and very dangerous in case of eye contact (irritant) or inhalation [171].

**Figure.II.1.** Structure of Acid Red 66**Table.II.2.** Some properties of the dye AR66

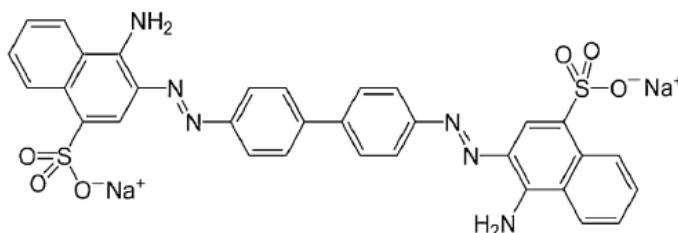
Dye	Class	λ_{\max}	Empirical formula	Molecular mass	Solubility
Acid red 66	Azo	~510 nm	C ₂₂ H ₁₄ N ₄ Na ₂ O ₇ S ₂	556.5 g. mol ⁻¹	> 30 g. L ⁻¹

II.2.3.2 The Congo Red (CR)

The Congo red was supplied by Alfa Aesar. Also known as Direct Red 28, the Congo red is an anionic organic compound belongs also to the azo dyes. Congo Red is the sodium salt of benzidinediazo-bis-1-naphthylamine-4-sulfonic acid; a diazo dye ($pK_a=3.7$) that has high solubility in water yielding a red brown color in alkaline solution and blue color in acid solution. It is more soluble in organic solvent. It is generated by some industries, including textiles, printing and dyeing, paper, rubber and plastic industries. It is used especially as an indicator and as a biological stain. It is classified as a hazardous product. In fact that it may cause cancer and damaging the unborn child. Some properties of the Congo red are presented in Table.II.3 [172].

Table.II.3. Some properties of the dye CR

Dye	Class	λ_{\max}	Empirical formula	Molecular weight	Solubility
Congo red	Di-azo	497 nm	C ₃₂ H ₂₂ N ₆ Na ₂ O ₆ S ₂	696.65 g/mol	10mg/mL

**Figure.II.2.** Structure of Congo Red

II.3 Methods of adsorbents preparation

II.3.1 Synthesis of LDH by coprecipitation method

LDH phases or anionic clays are easily synthesized in the laboratory. The coprecipitation is the most often used method to synthesize LDH. It is based on the co-precipitation reactions of the different metallic cations at constant pH. This method allows to obtain LDH structures with relatively high crystallinity.

Operating mode

Two solutions, A and B, were prepared. Solution A (500 mL) contained 0.8 M of cation metals (M^{+2} , M^{+3}) which were obtained by dissolving their chloride salts in deionized water at a ratio $M^{2+}/M^{3+} = 3$. Solution B (500 mL) contained 0.6 M of NaOH and 0.2 M of Na_2CO_3 . Solutions A and B were continuously added dropwise over 4h, in three-necked round bottom flask. The mixture was thoroughly stirred during the reaction under inert gas atmosphere (Argon). To induce the coprecipitation, the pH of the mixture was adjusted using 2M NaOH solution to $pH = 10.5 \pm 0.1$ and the temperature was maintained at $T = 65^\circ C$. After the drip process, the suspension was stirred at $65^\circ C$ for 24h and, afterward, centrifuged. The precipitate was then washed several times until the $AgNO_3$ test of the supernatant gave Cl^- free. After all, the resulting solid was dried at $70^\circ C$, grounded and sieved through 100-mesh sieve to give, finally, the LDH adsorbent powder. The protocol of the experiment is presented in Figure.II.3.

II.3.2 Synthesis of calcined LDH

The LDH synthesized as described in the previous paragraph was used to prepare the calcined LDH. A weighted mass of LDH was put in a porcelain nacelle of combustion. The nacelle was put inside a closed reactor equipped with input and output tubes allowing the circulation of the argon gas to insure a calcination under a flow of an inert gas (Ar_2). The reactor was installed inside a programmable furnace where the final temperature, the calcination period, the heating and cooling time are to be set. The LDH was calcined under $550^\circ C$ for 1h. The obtained LDH which had undergone a calcination was denominated as CLDH.

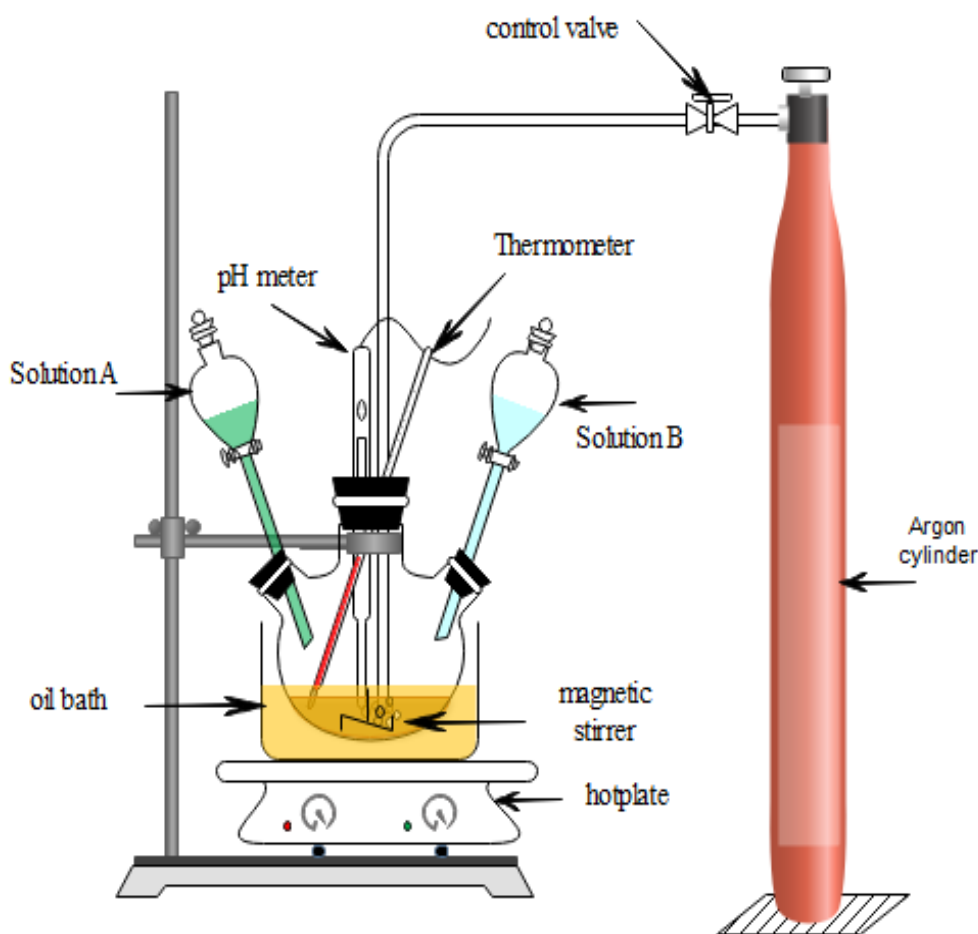


Figure.II.3. Schematic presentation of the experimental protocol used for LDH synthesis

II.3.3 Method of zeolite synthesis

II.3.3.1 Pre-treatment of the CFA

The CFA collected from the combustion power plant was firstly sieved through a 600 μ m screen. A mass of the obtained powder was put in a porcelain nacelle of combustion and put inside a programable furnace (Lindberg Blue M Box) provided with inert gas circulate on system.

The CFA had undergone a thermal treatment under 800C for 1h. Afterwards, the calcined CFA was acidly treated. A weighted mass (2g) of the calcined CFA was mixed with 20 ml of HCl solution 0.1M. The mixture was slowly stirred for 3 hours at 65°C. The solid was then recovered by filtration, washed by deionized water and dried out to be ready for the conversion into zeolite.

II.3.3.2 CFA conversion into zeolite

The solid powder recovered from the previous step (treated CFA) was added to 20ml of NaOH alkaline solution (1M). The Teflon tube, containing the mixture, was introduced into programmable microwave (single-mode, 2.5 GHz, CEM cooperation, Discover, USA) under a total reflux and an atmospheric pressure. The radiation power was adjusted at 250W and the running time at 45min. After 45 min, the tube was cooled down, the content was filtered and washed with DI water several times. Finally, the recovered powder was left to dry overnight at room temperature and stored for later use. Figure.II.4 represents a schema of the experimental protocol while Figure.II.5 summarizes the steps of ZNa-P synthesis.

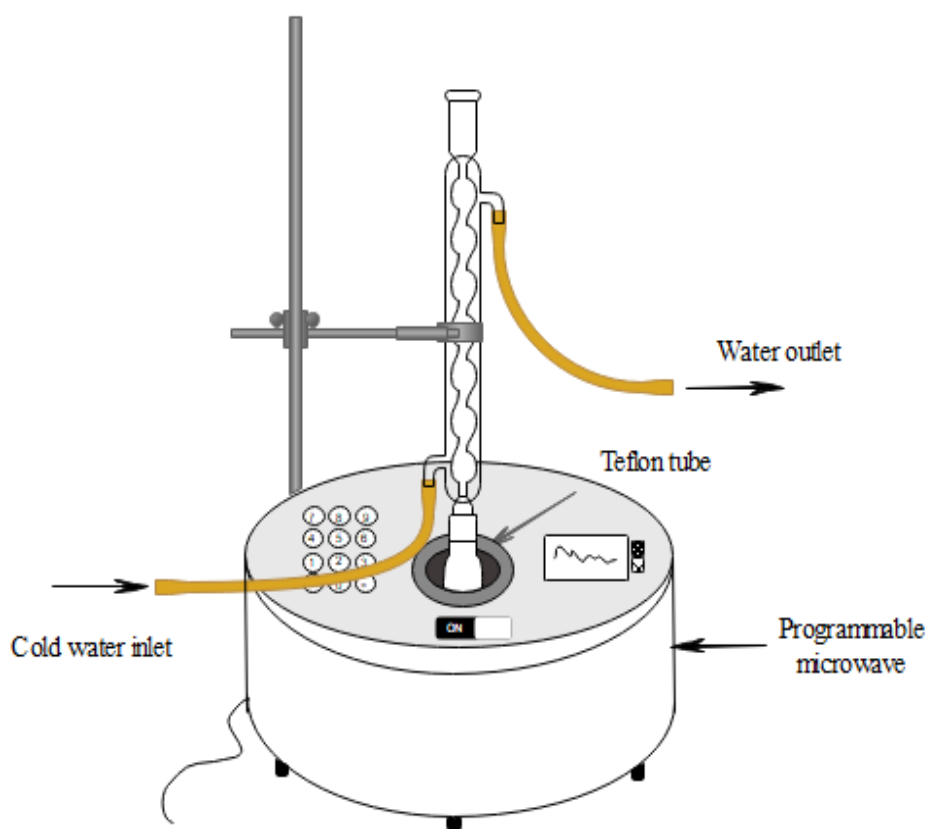


Figure.II.4. Schematic presentation of the experimental protocol used for ZNa-P synthesis

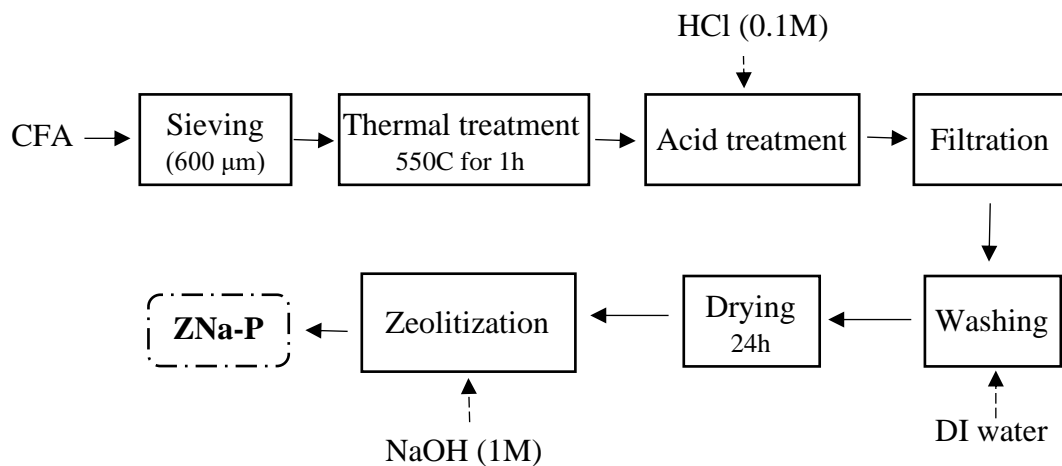


Figure.II.5. Schematic diagram of the experimental steps used for zeolite Na-P synthesis

II.4 Methods of analysis and characterization

II.4.1 X-ray diffraction analysis

All X-ray diffraction measurements were collected using the powder diffractometer Rigaku-Mini Flex (Japan) provided by the department of Chemical and Biochemical Engineering at Western University (Ontario, Canada). This non-destructive technique of analysis is commonly used for the crystal materials identification and for atomic spacing studies. The Rigaku-Mini Flex diffractometer is equipped with X Rays copper tube that regenerates $K\alpha$ radiation characterised by the wavelength $\lambda = 1.54059 \text{ \AA}$, sample holder and X ray detector which moves in a synchronized motion with the X-ray tube. The X-rays diffraction method consists on bombarding the sample with a monochromatic X-ray beam and measuring the X-ray intensity that is scattered according to the orientation in space. The signal coming from the sample is collected forming the diffraction diagram or "diffractogram". The characteristic peaks of the material were determined using the MDI-Jade v 7.5 software. Figure.II.6 shows a simplified schematic representation of the X ray diffraction phenomenon.

The fine powder sample (should not contain any large crystallite) is spread and flatten on a frosted glaze rectangular plate using a glass slide to make it suitably compressed and ready to be entered in the XRD machine. The operating conditions are set as following:

- Scan range (2θ): $2^\circ - 70^\circ$
- Step: 0.1°
- Scan speed: $1^\circ/\text{min}$

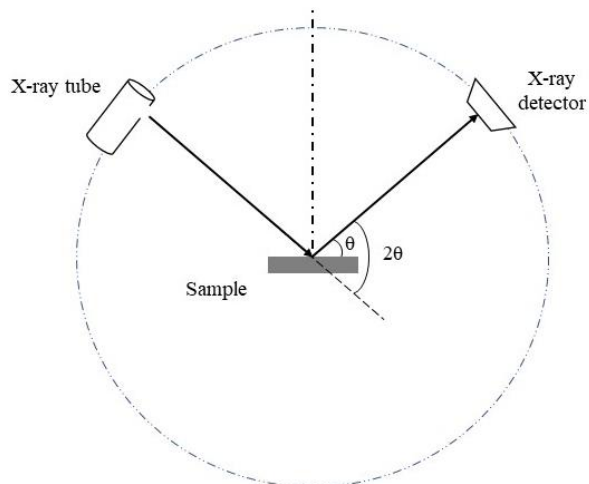


Figure.II.6. X-ray diffraction phenomenon inside a diffractometer

By the application of Bragg's law represented by equation II.1, the XRD analysis allows to determine the spacing between the atomic planes.

$$n \lambda = 2 d_{hkl} \sin \theta \quad \text{II. 1}$$

where n is an integer determined by the order of diffraction, λ (Å) is the wavelength of x-rays, θ (degree) is the diffraction angle (the angle between the incident ray and the scattering plane or between the scattering ray and the scattering plane as well),

II.4.2 Fourier-transform infrared spectroscopy (FT-IR)

Bruker vector 22 spectrometer was used to collect Fourier transform infrared spectra (FT-IR) of the synthesized materials adsorption in the range of wavenumber from 400 to 4000 cm^{-1} . The device is endowed with the software OPUS that allows to acquire and manipulate the spectrum. The IR spectroscopy is a method of spectroscopy that deals with infrared region of the electromagnetic spectrum. This method of characterization permits to identify the functional groups of the material molecule based on the produced spectrum.

The IR spectrum can be mainly divided into three zones identified in frequency (cm^{-1}) and wavelength (μm) respectively as follow: the far-IR ($400\text{--}10\text{ cm}^{-1}$, $25\text{--}300\text{ }\mu\text{m}$), The mid-IR ($4000\text{--}400\text{ cm}^{-1}$, $2.5\text{--}25\text{ }\mu\text{m}$) and the near-IR ($14,000\text{--}4000\text{ cm}^{-1}$, $0.7\text{--}2.5\text{ }\mu\text{m}$). The mid-IR region is the most commonly used in analysis in the fact that most compounds would have a signature absorption/emission in this region. The mid-IR region can be further divided into the fingerprint region ($400\text{--}1400\text{ cm}^{-1}$) and the functional groups' region ($1400\text{--}4000\text{ cm}^{-1}$).

This technique focuses on the nature of the bond vibrations between the atoms within the molecule. Each mode of vibration of an atomic bond is excited for a given frequency. These vibrations imply a variation of the dipole moment of the molecule and create a periodic electromagnetic field which absorbs the electromagnetic radiation of the same frequency. The absorption frequencies correspond to the frequencies of molecular vibrations. There are mainly two modes of molecular vibrations: stretching where the length of the bond is affected and bending where the angle between the two bonds is affected. Stretching mode can be symmetric or anti-symmetric depending on the motion of the two atoms. It is a symmetric if the two atoms simultaneously move towards and away from the central atom stretching and anti-symmetric if one of the atoms move towards the central atom while the other moves away from the central atom.

FTIR spectroscopy consists on irradiating the sample (solid, liquid or gas) with a multi-frequency infrared light beam and measure the amount of light absorbed or transmitted by the sample molecules. The obtained results are printed out on the screen in a form of graph called IR spectrum or spectrogram. The peak of absorption at each wavelength is characteristic to a specific chemical composition, thus the IR spectrum serves as a fingerprint of the molecule material which enables identification of the sample. Furthermore, the intensity or the absorption peak is a direct indication of the compound amount present in the material.

II.4.3 Wavelength dispersive X-ray Fluorescence (XRF)

X-ray fluorescence spectrometry (XRF) is a non-destructive quantitative analysis technique used to determine the chemical composition of different types of materials. The XRF is one of the simplest analytical methods that allow the determination of the elemental composition with high accuracy. XRF Spectrometer systems are generally divided into two main groups: Wavelength Dispersion Systems (WD-XRF) and Energy Dispersion Systems (ED-XRF). The difference

between the two is the detection system. The WD-XRF spectrometer consists of the following elements: a radiation source, a sample and a detection system. In the WD-XRF spectrometers, the X-ray tube (the source) directly irradiates a sample and the fluorescence from the sample is measured with a wavelength dispersion detection system. The characteristic radiation from each individual element can be identified by analyzing the crystals that separate the X-rays as a function of their wavelength. Such an analysis can be carried out either by measuring the intensity of X-rays at different wavelengths one after the other (sequential), or, in fixed positions, by measuring the intensities of X-rays at different wavelengths at the same time (simultaneous).

In this thesis, XRF analysis results were obtained using Rigaku ZSX Primus III+ WD-XRF spectrometer provided by the unity of research at Setif University. The powdered sample were first dried inside the oven at 110°C then they have been pressed into pellets before being loaded into the XRF system.

II.4.4 Scanning electron microscopy (SEM)

The surface imaging of the raw CFA and the zeolite were carried out by Hitachi S-3000N scanning electron microscope with a high-density frame memory of 1280x960 pixels and an advanced image capture and archiving system. The scanning electron microscopy (SEM) is a technique of electron microscopy that scans the surface of the sample with a focused beam of electrons to produce images of high resolution. In the scanning electron microscope, a thin electron beam is emitted by an electron gun. Electromagnetic lenses are used to control the electron's path and to focus the beam on the sample. The interaction between the electrons and the sample generates signals in the form of two types of electrons the backscattered (BSE) and the secondary electrons (SE). These signals are detected and converted into an electrical signal. This process is performed at each point of the sample by scanning the sample surface allowing the reconstruction of the sample typography and providing a relief image with a good resolution.

II.4.5 N₂ sorption-desorption analysis

Surface area, pore volume and pore size analysis were performed by an ASAP 2020M micromeritics instrument. The Brunauer–Emmett–Teller (BET) technique was adopted to measure the specific surface area (SSA) and the Barrett, Joyner, and Halenda (BJH) method, using the N₂ adsorption and desorption isotherms, was used to measure the pore sizes and the volumes. Before

performing the measurements, the samples were degassed overnight under vacuum at 130 °C. The mass of the sample after degassing is considered as the reference mass to calculate the amount of nitrogen adsorbed per gram of sample. BET theory aims to explain the physical adsorption of gas molecules on a solid surface and serves as the basis for an important analysis technique for the measurement of the specific surface area of a material, resulting from the interactions of this solid with a known pressure gas at a constant volume. Specific surface area (SSA) is a property of solids defined as the total surface area of a material per unit of mass. The method of BJH is a procedure for calculating pore size distributions from experimental isotherms. This technique characterizes pore size distribution independent of external area due to particle size of the sample.

II.4.6 Thermogravimetric and differential thermal analysis TGA/DTA

Mettler Toledo TGA/DTA 851e model (Switzerland) was used to record thermogravimetric and differential thermal data in the range of temperature: 25–800°C, under nitrogen atmosphere, with a heating rate of 10 °Cmin⁻¹. Thermal analysis is the analysis of a change in a property of a sample, which is related to an imposed change in the temperature. The sample is usually in the solid state and the changes that occur on heating include melting, phase transition, sublimation, and decomposition. The analysis of the change in the mass of a sample on heating is known as Thermogravimetric analysis (TGA). TGA measures mass changes in a material as a function of temperature (or time) under a controlled atmosphere. Its principal uses include measurement of a material's thermal stability and composition. In Differential thermal analysis (DTA), the temperature of a sample is compared with that of an inert reference material during a programmed change of temperature. The temperature should be the same until thermal event occurs, such as melting, decomposition or change in the crystal structure where a minimum will be observed on the curve if the event is endothermic and a maximum if the event is exothermic.

II.4.7 Zeta potential measurement

The zeta potential represents the charge that the particle acquires as a result of the ions surrounding it when it is being in solution. The zeta potential (ξ) of the material particles allows an estimation of their surface charges and, therefore, helps to interpret the results obtained during the adsorption of organic compounds. In this work, the Zeta potential was measured at different pH, using a 3000 zeta-analyzer. The samples were prepared by dispersing a mass of the material

powder in a volume of DI water. An ultrasound bath was used to ameliorate the particles dispersion in the aqueous solution.

II.5 Study of the adsorption

II.5.1 Ultraviolet–visible spectroscopy (UV/VIS)

In adsorption, when only one compound is to be determined, the UV/Visible spectrometry is the easiest method. It is a quantitative analytical method that measures the absorbance or optical density of a given chemical in solution

UV-visible spectrophotometry uses radiation in the range of ultraviolet (100-400 nm), visible (400-750 nm) or near infrared (750-1400 nm). This method allows a quantitative determination of the concentration of an analyte in solution. In UV-Vis spectrometer, a radiation beam with a wavelength varying between 180 and 1100 nm passes through the solution put in a cuvette. The sample in the cuvette absorbs this UV or visible radiation. The amount of the radiation that is absorbed by the solution depends on the concentration.

The relation of absorbance to the analyte concentration is given by Lambert-Beer's law (Beer's law)

$$A = \epsilon l C \quad \text{II. 2}$$

where A is absorbance (unitless), ϵ (epsilon) is molar absorption coefficient of the analyte for a certain wavelength ($\text{l mol}^{-1} \text{ cm}^{-1}$), l is path length (cm) through your cuvette and C is the concentration of the analyte (mol. l^{-1}).

The UV-Vis spectrum shows the absorbance of one or more sample component in the cuvette when we scan through various wavelengths in the UV/Vis region of the electromagnetic spectrum. The UV/Vis spectrometer gives a spectrum that shows the absorbance vs wavelength. By measuring and comparing a series of standard solutions -with known concentrations - of the analyte, the concentration of the analyte in the sample can be determined. The double beam UV–Vis spectrometer Varian Cary 100 Bio was used in this research to determine the concentration of the dye in the aqueous solutions.

To calculate the concentration of the dye remaining after adsorption, the calibration curves are used.

The calibration line: $A = f(C)$ (Lambert-Beer's law) was experimentally established using solutions of known concentrations of the compound to be analysed. After the adsorption, the absorbance of the solution is measured, and then the concentration of the dye solution is determined from its calibration curve.

The capacity of AR66 adsorption was determined using the Equation II.3.

$$Q_t = \frac{(C_0 - C_t)V}{m} \quad \text{II. 3}$$

The removal efficiency was determined by the Equation II.4.

$$\eta(\%) = \frac{(C_0 - C_e)}{C_0} * 100 \quad \text{II. 4}$$

Q_t (mg. g⁻¹): is the capacity of adsorption after t minutes.

C_0 (mg. L⁻¹): the initial dye solution concentration.

C_t (mg. L⁻¹): the dye solution concentration after t minutes.

η (%): the dye removal efficiency.

C_e (mg. L⁻¹): the dye solution concentration at equilibrium (final concentration).

V (L): the volume of the solution.

m (g): is the mass of the adsorbent.

II.5.2 Kinetics of adsorption

The adsorption was studied as a function of time to determine the equilibrium time. To study the kinetics as a function of the dye concentration, a measured volume of the dye solution is put in contact, at time $t = 0$, with a tared mass of the adsorbent and at natural or adjusted pH. The study was carried out for dye concentrations of 50, 100, 200 and 400 mg. L⁻¹ for the adsorption on LDH/CLDH and concentration ranging from 250, 500, 1000 and 2000 mg / L for the adsorption on ZNa-P. the experimental data of the adsorption kinetics was fitted to different mathematical models, mainly: pseudo-first-order, pseudo-second-order, Elovich, diffusion-chemisorption and intraparticle diffusion models

II.5.2.1 The pseudo-first-order model

The pseudo-first-order kinetic model given by Lagergren and Svenska [173] has been widely used to predict adsorption kinetics. This model gives the rate of adsorption of pollutant onto the adsorbent that is proportional to the amount of pollutant adsorbed from the solution phase.

$$\frac{dQ_t}{dt} = k_1(Q_e - Q_t) \quad \text{II. 5}$$

Where, k_1 is the rate constant of pseudo-first order adsorption, Q_e and $Q_t(\text{mg.g}^{-1})$ are the amounts of dye adsorbed at equilibrium and at a given time, t (mg/g). Integrating equation II.5 with applying boundary conditions $Q_t = 0$ at $t=0$ and $Q_t = Q_t$ at t the expression of Q_t becomes:

$$Q_t = Q_e(1 - e^{-k_1 t}) \quad \text{II. 6}$$

After linearization and simplification, II.6 becomes,

$$\ln(Q_e - Q_t) = \ln Q_e - k_1 t \quad \text{II. 7}$$

If experimental data satisfied a pseudo-first-order model, the plot of $\ln(Q_e - Q_t)$ vs t gives a linear relation. k_1 is the slope of the obtained line and Q_e is deduced from the intersection of the straight line at $t=0$ can be easily determined by extrapolation.

II.5.2.2 Pseudo-second-order model

The pseudo-second-order kinetic equation is also one of the models that are often applied to describe the sorption of pollutants onto adsorbents. The pseudo-second-order equation is given by the following equation II.8 [174],

$$\frac{dQ_t}{dt} = k_2(Q_e - Q_t)^2 \quad \text{II. 8}$$

Where, $Q_t(\text{mg.g}^{-1})$ and $Q_e(\text{mg.g}^{-1})$ are the quantity of pollutant adsorbed at time t (min), and at equilibrium, respectively; $k_2(\text{g.mg}^{-1}.\text{min}^{-1})$ is the pseudo-second-order rate. By applying the boundary conditions: $Q_t = 0$ at $t = 0$, and $Q_t = Q_t$ at $t = t \text{ min}$, integrating and rearranging the equation II.8, the Q_t for this model can be written as follows:

$$\frac{t}{Q_t} = \frac{1}{k_2 Q_e^2} + \frac{t}{Q_e} \quad \text{II.9}$$

If this model fits well the kinetics data, the plot of t/Q_t versus t should give linear plots with a slope of $1/Q_e$ and an intercept of $1/h$.

II.5.2.3 Elovich model

Elovich model or Roginsky–Zeldovich [175] is a rate equation usually used to study the kinetics of chemisorption capacity of pollutant on the adsorbate [176]. Generally, the Elovich model proposes the following linear expression for the capacity of adsorption (II.10).

$$Q_t = \frac{1}{\beta} \ln(\alpha \cdot \beta) + \frac{1}{\beta} \ln(t) \quad \text{II. 10}$$

where Q_t (mg.g⁻¹) is the amount of the pollutant adsorbed at time t (min), α (mg.g⁻¹min⁻¹) is the initial pollutant adsorption rate (mg/g.min) and β (g.mg⁻¹) is the desorption constant.

II.5.2.4 Diffusion-chemisorption model

The empirical diffusion-chemisorption model proposed by Clint Sutherland [177] can be also used to describe the adsorption of dyes on adsorbents, the equation of the model is given by the following expression (II.11)

$$\frac{t^{0.5}}{Q_t} = \frac{1}{k_{DC}} + \frac{1}{Q_e} t^{0.5} \quad \text{II. 11}$$

where k_{DC} (mg.g⁻¹min^{-1/2}) is the diffusion-chemisorption constant.

On the basis of $t^{0.5}/Q_t$ versus $t^{0.5}$ the plot of diffusion-chemisorption model can be obtained. Sutherland found that the initial slope of the experimental kinetic curve is a function of the diffusion-chemisorption constant k_{DC} and equilibrium sorption capacity Q_e . Assuming a linear zone when t tends to zero, the following empirical relationship was proposed (II.12) [177].

$$k_i = k_{DC}^2 / Q_e \quad \text{II. 12}$$

Where k_i (mg/g min).is the initial sorption rate.

II.5.2.5 Intraparticle diffusion model

The adsorption process of a solute on an adsorbent is generally described by the kinetics of adsorption; while the adsorption diffusion mechanism is mainly described by the intraparticle

diffusion model. The experimental results of the adsorption kinetics were used to study the diffusion mechanism of the AR66 adsorption on ZNa-P. Thus, the obtained parameters of the model can be used to predict the adsorption rate of the dye. The intraparticle diffusion model equation is given by Weber-Morris equation (II.13) [178],

$$Q_t = k_{id}t^{0.5} + C \quad \text{II. 13}$$

where k_{id} ($\text{mg/g.min}^{1/2}$) is the intraparticle diffusion rate constant obtained from the plot slope and C is the interception of the regression line that supplies information on the boundary layer thickness.

II.5.3 Isotherms models

Equilibrium studies or adsorption isotherms, as known, is an important aspect for adsorption studies, it helps to describe the adsorbent-adsorbate interaction and provides information on the maximum capacity of adsorption. This process is described at the equilibrium by means of some equations that quantify the amount of substance attached on the surface given the concentration in the fluid. These equations are called isotherms (the most famous are the Langmuir and the Freundlich equations). Adsorption phase equilibrium is an important theory to analyze the adsorption separation technology and is the basis of describing an adsorption capacity of adsorbed molecules in adsorbents and adsorptive selectivity.

The adsorption isotherms were performed at room temperature of 24 ± 1 °C and at natural pH for the adsorption on LDH/CLDH and at pH of 3 for the adsorption on ZNa-P. Weighed masses of the adsorbent were introduced to equal volumes of the dye solution with different initial dye concentrations. The flasks were put under agitation for a contact time at the end of which the equilibrium between the different phases is supposed to be reached. Then, the contents of the flasks were centrifuged and analyzed by UV-VIS.

Several models are used to analyse equilibrium data including tow parameters models, such as the Langmuir and Freundlich models, and three parameters models, such as the Sips and Toth models.

II.5.3.1 Langmuir model

Langmuir [179] defines the adsorption equilibrium as a dynamic process between the molecules arriving at the surface and those leaving the surface. Langmuir considers that the adsorption sites are equivalent, that the surface is homogeneous and that there are no lateral interactions between the adsorbed molecules.

Langmuir non-linearized equation is given by the equation II.14

$$\frac{Q_e}{Q_m} = \frac{K_L C_e}{1 + K_L C_e} \quad \text{II. 14}$$

where K_L ($L \cdot mg^{-1}$) K_L ($L \cdot mg^{-1}$) is the Langmuir adsorption constant related to the energy of adsorption, Q_e ($mg \cdot g^{-1}$) is the equilibrium adsorption capacity, Q_m ($mg \cdot g^{-1}$) the monolayer capacity of the adsorbent, C_e ($mg \cdot L^{-1}$) is the dye concentration at equilibrium.

An essential characteristic parameter, called the separation factor R_L , can be calculated for the Langmuir model. It predicts the feasibility of adsorption process: for $0 < R_L < 1$, the process is favorable, irreversible if $R_L = 0$, linear if $R_L = 1$ or unfavorable if $R_L > 1$. The R_L expression is given by the equation II.15 [180].

$$R_L = \frac{1}{1 + K_L C_0} \quad \text{II. 15}$$

Where K_L is Langmuir constant and C_0 is the highest initial concentration.

II.5.3.2 Freundlich model

Freundlich model [181] is based on adsorption on heterogeneous surfaces. Freundlich non-linearized equation can be described as follows (II.16).

$$Q_e = K_F C_e^{1/n} \quad \text{II. 16}$$

where K_F ($L \cdot mg^{-1}$) and n are empirical constants associated to sorption capacity and sorption intensity, respectively. Q_e ($mg \cdot g^{-1}$) is the capacity of adsorption at equilibrium, C_e ($mg \cdot L^{-1}$) is the dye concentration at equilibrium.

II.5.3.3 Sips model

Sips model is a combination between Langmuir and Freundlich isotherms; it can be expressed by the equation II.17 [36]:

$$\frac{Q_e}{Q_m} = \frac{(K_S C_e)^m}{1 + (K_S C_e)^m} \quad \text{II. 17}$$

where K_S ($L \cdot mg^{-m}$) is constant of Sips related to the energy of adsorption, m is the exponent of the Sips model related to the intensity of adsorption.

II.5.3.4 Toth model

Toth is another empirical modification derived from the Langmuir model that can be expressed by the following equation (II.18) [182]:

$$Q_e = \frac{K_T C_e}{[a_T + C_e]^{1/t}} \quad \text{II. 18}$$

where K_T ($mg \cdot g^{-1}$), C_e ($mg \cdot L^{-1}$), a_T ($L \cdot mg^{-1}$) and t are Toth isotherm constants.

The isotherms data were fitted to the different models on Origin software and the parameters of each applied model were determined using non-linear regression.

In order to evaluate the applicability of the mathematical models, the correlation coefficients R^2 and the Residual Mean Square Error (RMSE) were used. The R^2 and RMSE are given by the following equations [183].

$$R^2 = 1 - \frac{\sum_{i=1}^n (Q_{i \text{ exp}} - \hat{Q}_i)^2}{\sum_{i=1}^n (Q_{i \text{ exp}} - \bar{Q})^2} \quad \text{II. 19}$$

$$RMSE = \sqrt{\frac{1}{n} \sum_{i=1}^n (Q_{i \text{ exp}} - \hat{Q}_i)^2} \quad \text{II. 20}$$

n : the number of experiments

$Q_{i \text{ exp}}$: the i^{th} capacity of adsorption.

\hat{Q}_i : The i^{th} predicted capacity of adsorption using the mathematical model.

\bar{Q} : the average of the capacities of adsorption.

II.5.4 Thermodynamic study

The thermodynamic parameters reveal the possibility and the spontaneity of the process. The study of the variations of the constants of equilibrium with the temperature enables us to estimate the thermodynamic parameters, essentially the Gibbs free energy change (ΔG°), the enthalpy change (ΔH°) and the entropy change (ΔS°). ΔG° (kJ.mol⁻¹) are given by the equations (II.21, II.23, II.24) as reported by Milonjic [67].

$$\Delta G^\circ = -RT \ln(\rho K_C) \quad \text{II. 21}$$

$$K_C = \frac{Q_e}{C_e} \quad \text{II. 22}$$

ΔG° (kJ.mol⁻¹): Gibbs free energy change.

R: the gas constant R= 8.31J.mol⁻¹K⁻¹.

T (K): the temperature.

K_C (L.g⁻¹): the thermodynamic equilibrium constant given by

ρ (g L⁻¹): the water density.

$$\ln(\rho K_C) = -\frac{\Delta H^\circ}{RT} + \frac{\Delta S^\circ}{R} \quad \text{II. 23}$$

$$\Delta G^\circ = \Delta H - T\Delta S \quad \text{II. 24}$$

ΔH° : the enthalpy change (kJ mol⁻¹)

ΔS° : the entropy change ((J.mol⁻¹.K⁻¹)

$\Delta H/R$ and $\Delta S/R$, therefore ΔH and ΔS , were derived from the slope and the intercept of the linear graph: $\ln(\rho K_C)$ vs $1/T$, respectively.

II.6 Experimental Design software: Design-Expert 7

A part of our work consists on the application of an experimental design to investigate the adsorption experiments instead of applying the conventional method of “one variable at time”. In this thesis, the software used for that purpose is the Design Expert® version 7.0.0. Design Expert to help us with the design and the fitting of our experimental data and the interpretation of multi-factor experiments.

In order to establish the experimental design, first the experimental design wanted to be used was selected as shown in Figure.II. 7. The experimental design used in our study was the central composite design (CCD). Then the different of parameters of the studied system were defined, along with there names; codes, types (numeric or categoric) and unities. The range of variation of each parameter was also specified, where the lowest level is considered as level -1, the central level is level 0 and the highest is level 1. The response chosen in this study was the capacity of adsorption (mg. g^{-1}).

Based on the input information, the design software will propose a minimum optimized number of experiments that should be done for a full study of the wanted system (evaluation, analysis and optimisation). After performing the experiments, a complete study on the system is accomplished (individual effect of each parameter, interaction effects, modeling and optimisation) exploiting the different options provided by the software (Transform, fit summary, fitting models, ANOVA, diagnostics...)

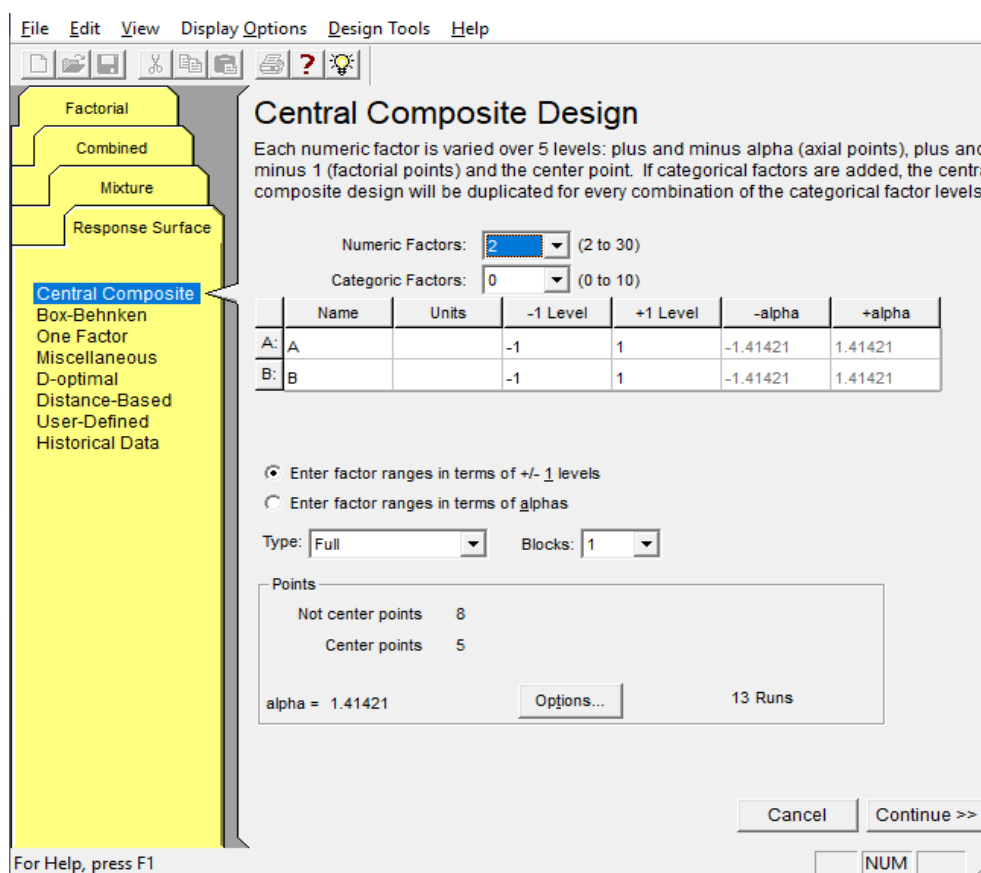


Figure.II. 7. The window of Design Expert software

Chapter III

Mg-Cu-Al-Fe LDH to enhance the adsorption of Acid Red 66 dye: characterization, kinetics and isotherm study

III.1 Introduction

Layered double hydroxides (LDHs) are, increasingly investigated as potential materials for wastewater treatment [9], [18]. The LDHs have been used as adsorbents for a large environmental wastewater pollutant, such as dyes [10], chlorophenols [17], heavy metals [9],[18] and monoatomic ions [19].

Along with magnesium and aluminium, large cations have been integrated in the synthesis of LDHs including zinc, iron, lithium, calcium, manganese, chromium, cobalt, nickel, copper and others [29, 31, 33]. To the best of our knowledge, LDHs used as adsorbents reported in literatures were mostly binary [14, 33, 34] or ternary LDHs [35–37] and rarely quaternary LDH [16].

In this work, a quaternary layered double hydroxide that contains magnesium, aluminum, copper and iron was synthesised by a co-precipitation method at constant pH. A portion of the resulting LDH was calcined under inert gas flow at a temperature of 550°C. Both the calcined and non-calcined LDH were applied to remove AR66 dye from aqueous solutions. XRD, FTIR, SEM, N₂ adsorption-desorption, and zeta potential were used for the characterization of the synthetic LDH. The results reported in this chapter were published in the Arabian journal for Science and Engineering.

III.2 Materials and Methods

III.2.1 Characterization

To study the different properties of the synthesised materials such as structural and morphological properties, many characterization methods have been used. Rigaku-MiniFlex powder diffractometer (Japan) was used to collect XRD data of the synthesised LDH and CLDH before and after adsorption under CuK α radiation ($\lambda = 1.54059\text{\AA}$).

Fourier-transform infrared (FT-IR) spectra were obtained using Bruker vector 22 spectrometer in a wavenumber range of 4000–400 cm⁻¹.

Surface area, pore volume and pore size analysis were performed by an ASAP 2020M Brunauer-Emmett-Teller (BET). The BET technique was adopted to measure the specific surface area (SSA) and the BJH method, using the N₂ adsorption and desorption isotherm, was used to measure the pore sizes and the pore volumes of LDH and CLDH. Before that the measurements are made, the samples were degassed overnight in vacuum at 130 °C.

The micro morphology of the samples was studied by SEM using Hitachi S-3000N. The elemental composition of LDH and CLDH was also recorded by XRF using RIJQU ZSX PRIMUS IV apparatus. The different elemental composition by XRF is given by mass %.

Mettler Toledo TGA/DTA 851e model (Switzerland) was used to record thermogravimetric and differential thermogravimetric data in the range of temperature: 25°C to 800°C, under nitrogen atmosphere, with a rate of heating rate of 10°C/min.

Zeta-potential for both LDH and CLDH was evaluated at different pH. For these measurements, 0.02 g of LDH was added to 25 mL of DI water. The pH of the suspension was set to different values in the range 2 to 12 by a dropping NaOH (1M) and/or HCl (1M) solutions. To obtain homogeneous suspensions, the latter were placed in Ultrasound bath for 1h. Then, each suspension was analyzed by a 3000 zeta-analyzer.

III.2.2 Adsorption experiments

All adsorption experiments were operated in batch mode using LDH or CLDH as adsorbent. The effects of different parameters on the adsorption capacity were examined: pH, adsorbent dosage, contact time, initial dye concentration and salts addition. For the pH effect study, the initial pH of the dye solutions was set to different values, from 2 to 12, with 1M HCl and 1M NaOH solutions. The effect of adsorbent dosage was examined by changing the solid/solution ratio between 0.2 g.L⁻¹ and 1g.L⁻¹. The effect of the ionic strength was performed by adding different salts NaCl, Na₂CO₃ and Na₂SO₄. Each salt was added to the solution samples in different amounts: 0.50 mg. L⁻¹ to 50 mg. L⁻¹. Samples were stirred over 24h using similar magnetic stirrers at room temperature T= 24±1°C and at the pH of the dye solution (pH=6.76).

For kinetic studies, 120 mg of adsorbent were added in 200 mL Erlenmeyer containing 150 mL of the dye solution with a pre-determined concentration, which were then stirred under constant speed of 250 rpm at room temperature (24±1°C) and natural pH. After every given contact time samples were taken until the equilibrium was established. Experiments were repeated for different dye solution concentrations (50 to 400mg. L⁻¹) to examine the effect of the initial dye concentration on the adsorption capacity on LDH and CLDH.

Isotherm experiments were accomplished at room temperature, where masses of 20 mg of adsorbent was added to dye solution volumes of 25 mL with different concentrations (from 50

mgL⁻¹ to 600 mg L⁻¹ for LDH and 50 mg L⁻¹ to 1200 mg L⁻¹ for CLDH); the suspensions were being agitated under 250 rpm for 24h. The capacity of dye adsorption at equilibrium (Q_e) and the dye concentration at equilibrium (C_e) were calculated then used to plot the isotherm graphs.

To explain the adsorption kinetic process, various models were adopted: pseudo-first order, pseudo-second order, Elovich and Intra particle diffusion models. These models are detailed in Chapter II, Section II.5.2.

Empirical data points of equilibrium adsorption were fitted to different bi- and tri- parameter models, often applied in the literature, such as Langmuir, Freundlich, Sips and Toth models provided in Chapter II Section II.5.3. These models describe the non-linear equilibrium between the adsorbed molecules of adsorbate (Q_e) and the adsorbate molecules which remain in the solution (C_e) at a steady temperature.

III.3 Results and Discussion

III.3.1 Characterizations of the adsorbents

The XRD patterns of LDH and CLDH (obtained after heat treatment of LDH at 550°C) are illustrated in Figure.III.1. Comparing with the diffractograms of layered double hydroxides described in previous literatures [77], [185], [186], sharp and symmetrical peaks of LDH (Figure.III.1 (a)) appeared at the same basal planes (003), (006) and (009) corresponding to $2\theta = 11.64^\circ$, 23.26° , and 34.54° respectively. Also, some asymmetrical peaks appeared at non-basal planes (012), (015), (018), (110) and (113) at higher angles (35.74° , 38.96° , 48.38° , 60.12° , and 61.56°). These peaks, characteristic of hydrotalcite phase, confirmed the formation of well crystalline layered structure. Applying Bragg's law at (003) diffraction peak, the basal spacing d_{003} of LDH was found to be 0.76nm. Similar d_{003} values for carbonate LDHs were reported previously [187]. CLDH diffraction patterns are represented by the plot b in Figure.III.1. it is noteworthy that hydrotalcite characteristic peaks (003) (006) and (009) disappeared indicating the collapse of the layered structure after calcination. In fact, high temperature leads to dehydration, dehydroxylation and interlayer anions release, which induces the decomposition of the layered structure [188].

Three major peaks for CLDH appeared at around 35.76° , 39° , 42.46° , 43.44° and 62.88° . These peaks can be attributed to the formation of mixed metal oxides mainly MgO, CuO, Fe₂O₃,

MgAl₂O₄ and probably MgFe₂O₄ [189] [190]. The XRD analysis of CLDH powder obtained after adsorption of AR66 dye (CLDH-AR66), represented by the plot d in Figure.III.1, showed the re-appearance of the characteristic peaks of layered hydroxides confirming the reconstruction of its structure after the adsorption process which is called the ‘memory effect’ [187]–[191].

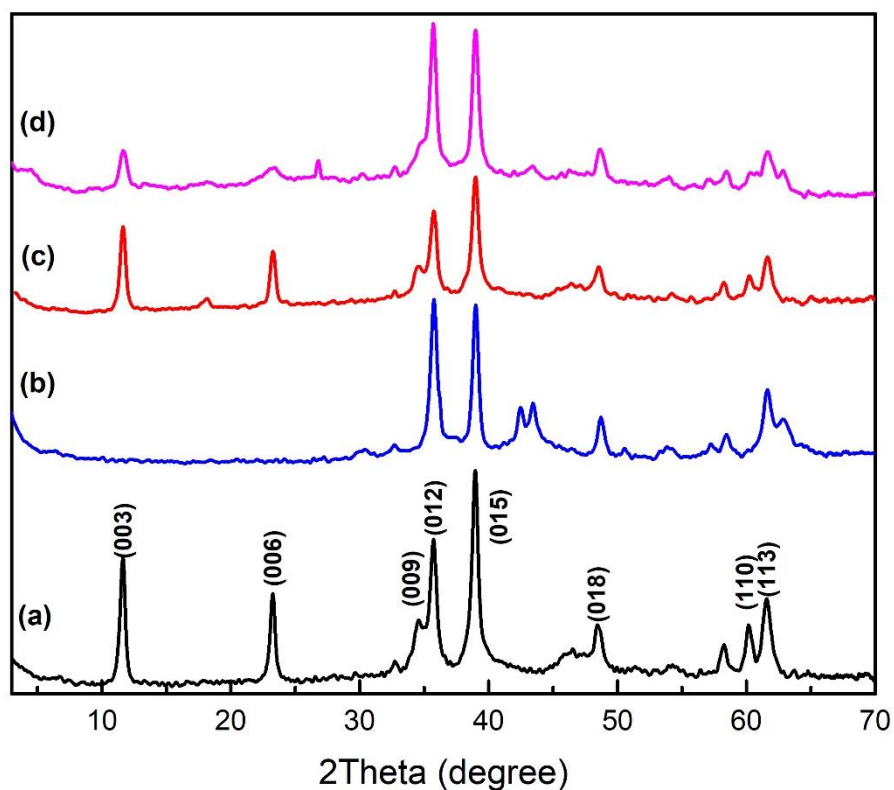


Figure.III. 1. XRD patterns of (a) LDH, (b) CLDH, (c) LDH-AR66 and (d) CLDH-AR66

The FT-IR spectra of the prepared samples are illustrated in Figure.III.2. A broad band was revealed at around 3470 cm⁻¹ in LDH spectrum which can be referred to the asymmetric and symmetric stretching mode of the O-H bond in the hydroxyl groups that compose the LDH layers and in the interlayer water [192]. This peak was strongly reduced in the FTIR spectrum of CLDH involving the departure of water molecules and confirming the XRD results that LDH structure has been destroyed after calcination. At around 1650 cm⁻¹ the weak band was ascribed to the bending vibration of the molecules of water in the interlayer spaces of the LDH [193]. Sharp and symmetric peak appeared at 1365cm⁻¹ which corresponded to the vibrations of CO₃²⁻

interlayer anions [194]. It can be observed in the CLDH FTIR spectrum that after calcination the peak at 1365cm^{-1} was weakened which may imply that a part of CO_3^{2-} molecules were removed [106].

The other absorbances at low frequencies in the range of $500\text{ cm}^{-1} - 1000\text{ cm}^{-1}$ can be associated to Metal -Oxygen vibration mode (M-O) where M could be one of the metal cations that forming the LDH [195]. Figure.III.2 revealed that a couple of peaks which are appropriate to AR66 dye appeared on FTIR spectra of LDH and CLDH after AR66 adsorption presented by the plot b and d, respectively. Also, it can be observed that the peaks of AR66 ($900\text{ cm}^{-1} - 1560\text{ cm}^{-1}$) are more obvious on CLDH-AR66 spectra then LDH-AR66 due to the high quantity adsorbed by CLDH.

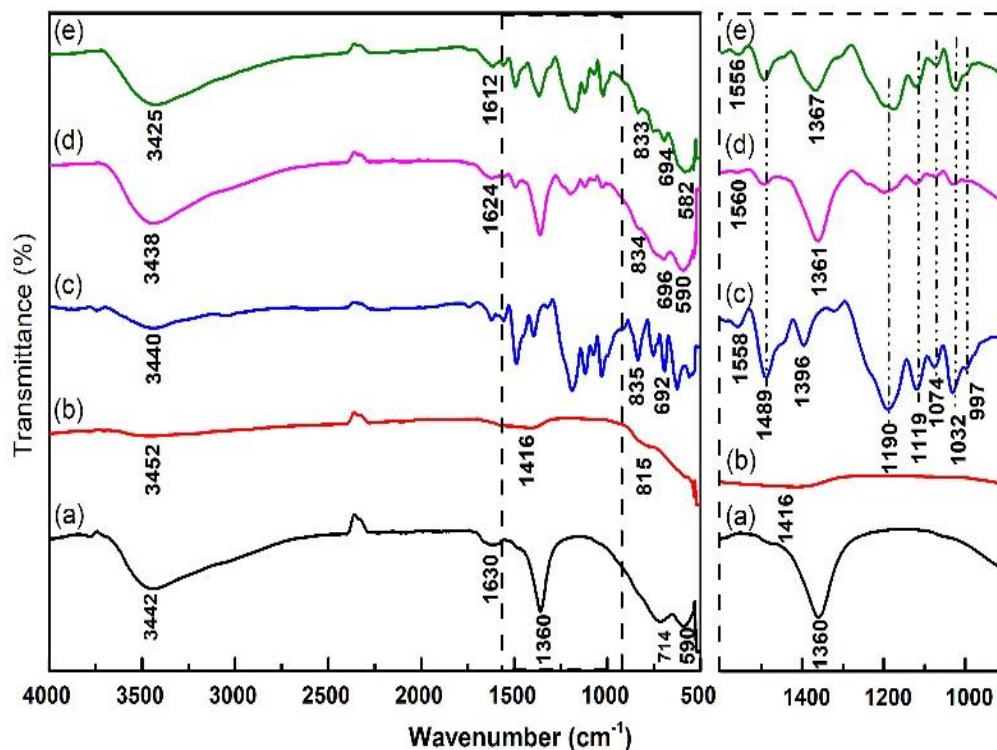


Figure.III. 2. FTIR spectra of (a) LDH, (b) CLDH, (c) AR66, (d) LDH-AR66 and (e) CLDH-AR66

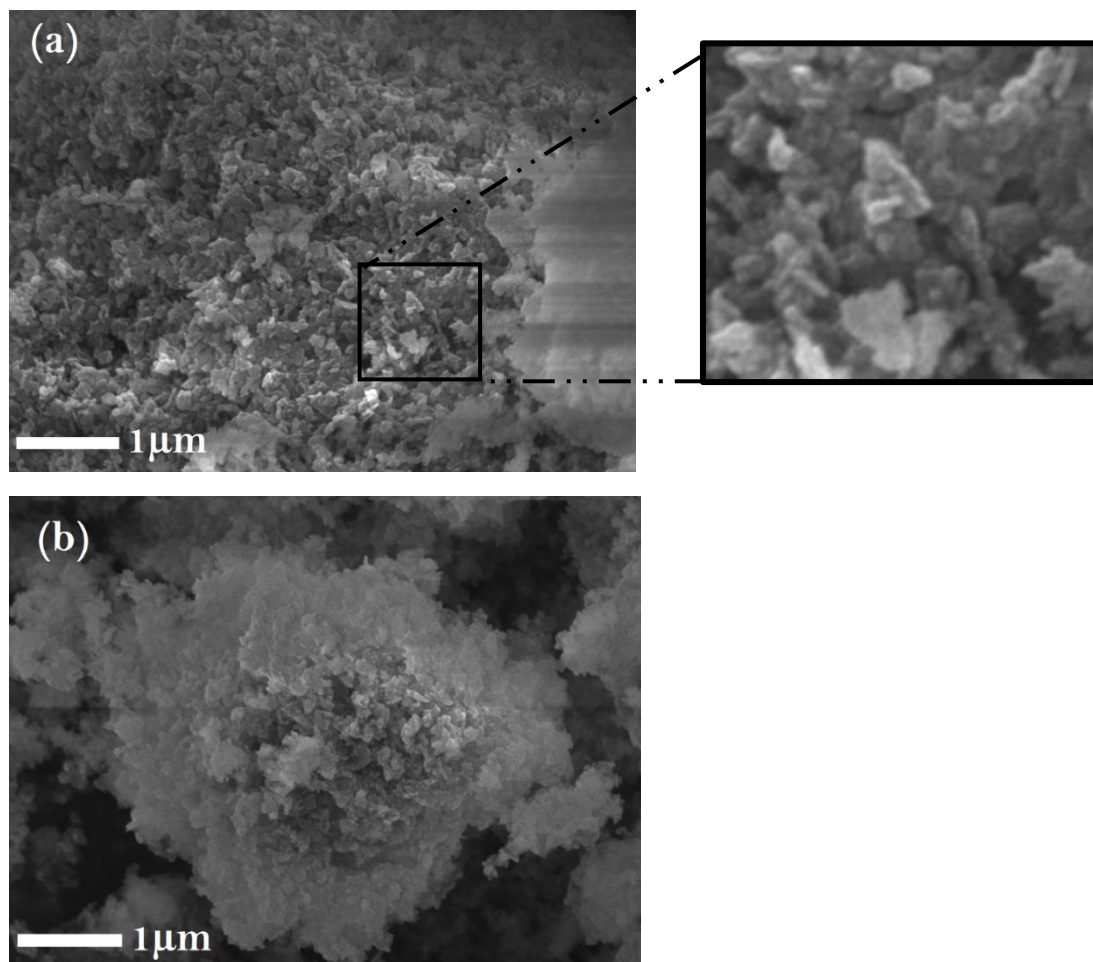


Figure.III. 3. SEM micrographs of (a) LDH, (b) CLDH

The SEM images of the samples LDH and CLDH are shown in Figure.III.3. From LDH scanning microscopy figure (Figure.III.3 (a)) it can be observed that homogenous nanosheet shapes have been formed with a length of 100nm-200nm. After calcination at temperature of 550°C the hole structure was broken to smaller parts and a sintering of the sample can be observed which can be due to the collapse of the layered structure after calcination [196].

Table.III. 1 and Figure.III.4 exhibit the elemental composition results of LDH and CLDH. It could be seen obviously that the chemical composition results confirm that the four metal cations were involved in the formation of the LDH which was first synthesized in this paper. In addition, the experimental value of the ratio x used for the preparation precursor LDH ($x=3$) is very closed to the x value determined by XRF ($x=2.89$) concluding that the LDH has been

synthesized with the wished composition. For CLDH, it can be revealed from Table.III. 1 that there is a slight difference between the mass% of each element of the two materials LDH and CLDH which could be explained by the presence of the same metals in a form of metal oxides as demonstrated by XRD patterns.

Table.III. 1. Elemental analysis of LDH and CLDH

	Cu (%)	Mg (%)	Al (%)	Fe (%)
LDH	62.9	13.6	7.53	14.6
CLDH	60.1	16.3	6.48	15.5

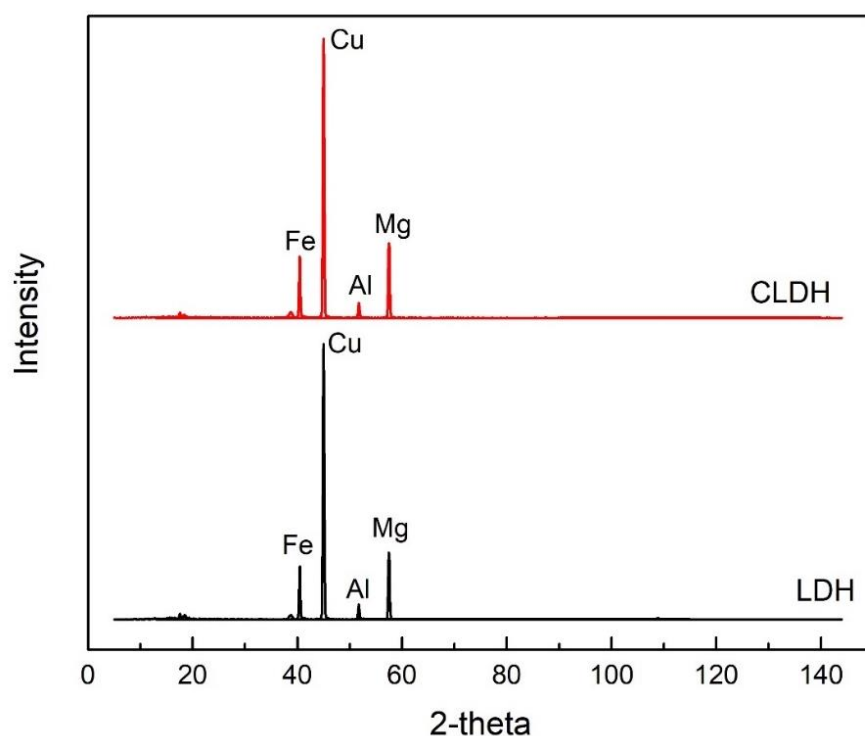


Figure.III.4. XRD patterns of LDH and CLDH

The results of N₂ adsorption-desorption isotherms of LDH and CLDH are represented in Figure.III.5; while the SSA, pore volumes and pore sizes are included in Table.III. 2. In accordance with the isotherms classification of Sing et al. [197], the isotherms of the prepared materials can be classified as type II presenting H3 type hysteresis loops at high relative pressures P/P° ; which signifies the existence of mesoporous structure with non-rigid aggregates of particles with plate-like form creating slit-shaped pores with varying shape and size [197],

[198]. The condensation step of the isotherm measured on CLDH presented a shift to higher relative pressure comparing to LDH isotherm which suggested that CLDH had larger pores than LDH, which was confirmed by the PSD curves.

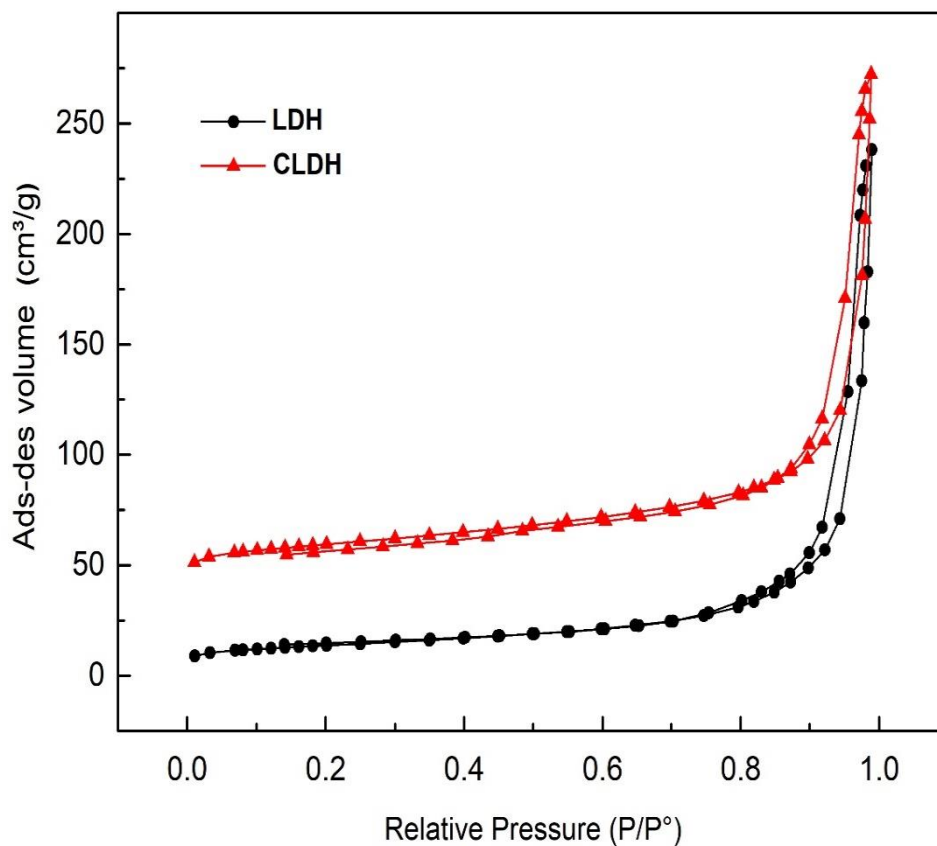


Figure.III.5. N₂ adsorption desorption isotherms of LDH and CLDH

Table.III. 2. BET textural properties of LDH and CLDH

Sample	BET Surface area (m ² .g ⁻¹)	Pore size (Å)	Pore volume (cm ³ .g ⁻¹)
LDH	48.5	203.1	0.36
CLDH	69.7	305.4	0.36

The pore size distribution (PSD) for LDH and CLDH are shown in Figure.III.6. The PSD curves of both adsorbents present two broad peaks for each. The first peak was observed at small pore diameters reflecting the presence of pores within nanosheets, centered at 4nm for LDH and 10nm for CLDH. The other peak was shown at higher pore diameters, centered at 40nm and 45nm for LDH and CLDH respectively. This latter peak can be assigned to the pores created between the piled nanosheets [199]. CLDH, treated at high temperature 550°C, presented higher specific area of $69.67\text{m}^2.\text{g}^{-1}$ compared to that of LDH which was about $48.5\text{m}^2.\text{g}^{-1}$. The pore volume and the average pore size also increased after calcination from $0.360\text{ cm}^3.\text{g}^{-1}$ to $0.369\text{ cm}^3.\text{g}^{-1}$ and from 208.29 \AA to 321.27 \AA , respectively. This increase in the SSA and the other pore parameters can be interpreted by the removal of the interlayer water, the intercalated ions and carbon dioxide of the starting synthesized LDH leading to the formation of channels and pores [200].

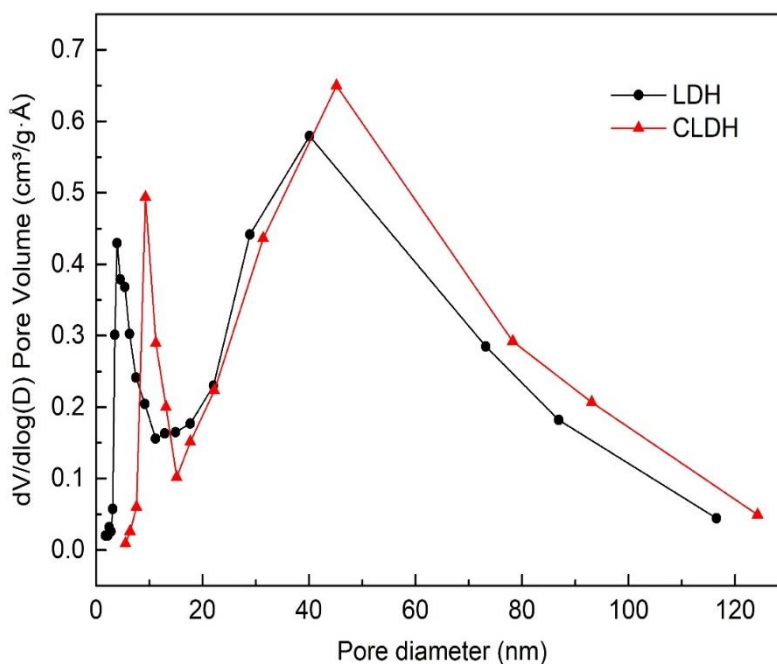


Figure.III.6. The pore size distribution for LDH and CLDH

The Thermogravimetric and Differential Thermogravimetric Analysis (TGA/DTA) of LDH and CLDH samples, corresponding to the monitoring of the weight loss as a function of temperature, are plotted in Figure.III.7. For LDH samples, a thermal decomposition profile

identical to layered hydroxides materials was shown [201]. It can be seen that the total weight loss was about 44%, which occurred in three main endothermic steps. The first step took place at temperatures below 210°C where the weight loss was estimated to be about 14%. In this temperature range an endothermic peak at is observed at 167.5°C preceded by a shoulder at around 68°C which are be attributed to the departure of the interlayer and superficial water molecules, respectively [111].

The second step took place at a temperature range of 210°C – 425°C. In this range, the 19% of weight lost can be related to the decomposition of hydroxide layers by dihydroxylation producing metal oxides and the expulsion of intercalated carbonate anions in the form of carbon dioxide [74].

Finally, the third weight loss was about 11%; it occurred at temperature above 480°C and can be attributed to the continuous decomposition that started in the second step, dihydroxylation and the destruction of the lamellar structure with the formation of mixed oxides [13].

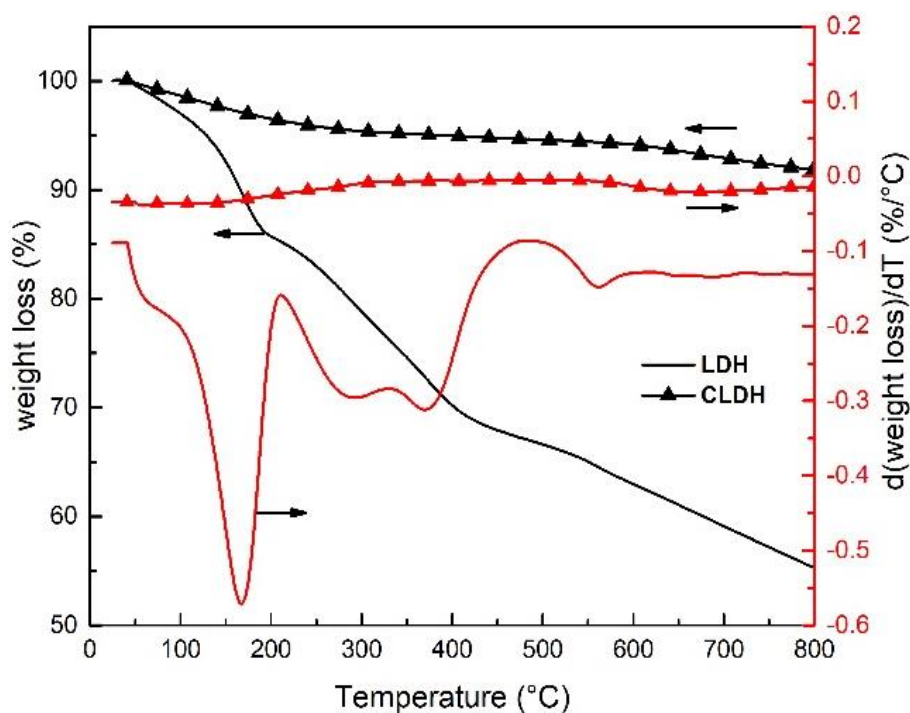


Figure.III. 7. TGA and DTA curves of LDH and CLDH (heating rate = 10°C/min, under 40 mL/min N₂)

Otherwise, the CLDH sample shows a different expected behavior, in comparison with LDH sample, since no significant change was observed along the overall temperature range (25°C-800°C). The total weight loss was only about 10% that can be caused by the release of water adsorbed during storage, or dihydroxylation of hydroxides and liberation of carbonate remaining after calcination leading to an amorphous material [202].

III.3.2 Adsorption behavior

III.3.2.1 Effect of the initial solution pH on the dye adsorption

As it is known, the adsorption process is highly affected by the pH since it changes the charge surface of adsorbents and the ionization of dyes [185]. The impact of the initial pH on the adsorption capacities was studied for both adsorbents LDH and CLDH. The results of the amount adsorbed on LDH and CLDH at several pH values are displayed in Figure.III.8.

For both of adsorbents, it could be observed that the highest capacities of adsorption were obtained in acidic conditions. A maximum of adsorption was found for an initial pH of 2 corresponding to 54% and 99.5% of removed dye for LDH and CLDH, respectively. Then the amount adsorbed decreased for increasing pH values until reaching a minimum in alkaline conditions. The same observations were noticed by Guo et al. [10], [16], [101], [203].

It is noteworthy that even at alkaline pH, the capacity of adsorption on CLDH remained relatively high, with a dye removal yield above 70%; while for LDH, the uptake percentage decreased remarkably to less than 30% in alkaline conditions. The pH of the initial AR66 solution (pH=6.8) was considered thereafter.

The influence of pH can be justified by its relation to the charge of the adsorbent surface and the nature of the physicochemical interactions between the adsorbate and the adsorptive sites. Hence, to elucidate that, zeta potential (ζ -potential) of LDH and CLDH was performed at different pH between 2 and 12 and the point of zero charge (pH_zc) was determined. The corresponding results are revealed in Figure.III.9.

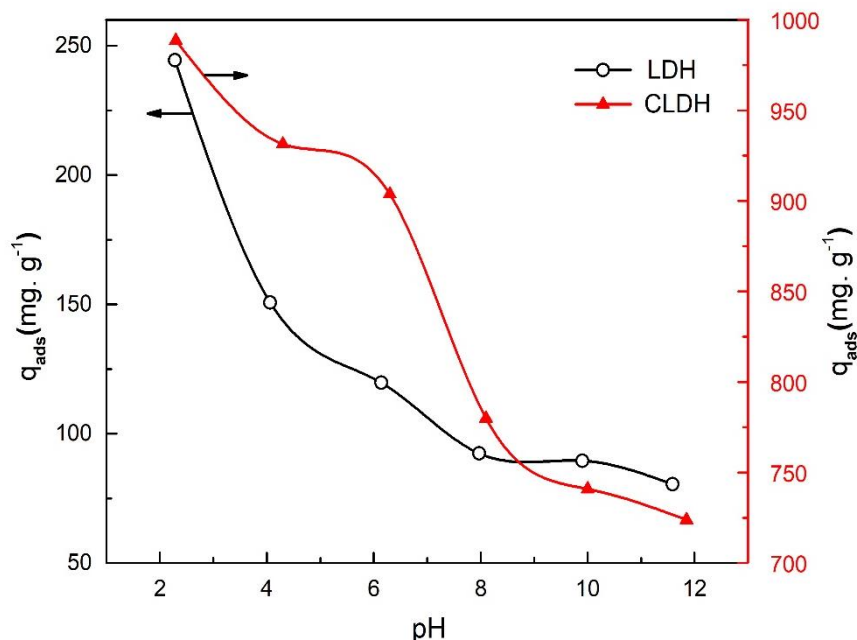
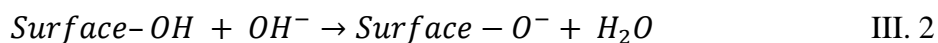
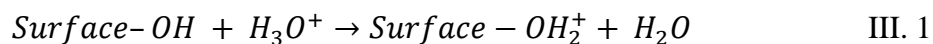


Figure.III.8. Initial pH effect on AR66 adsorption onto LDH ($C_0= 200 \text{ mg.L}^{-1}$, $T=23^\circ\text{C}$, speed= 250rpm) and CLDH ($C_0= 800 \text{ mg.L}^{-1}$, $T=23^\circ\text{C}$, spd= 250rpm).

Theoretically, for pH under the pH_{zc} , superficial area of the adsorbent is protonated (equation III.1), and hence acquiring a positive charge, which promotes the adsorption of anionic dyes that are negatively charged due to the electrostatic attraction forces. However, for pH above the pH_{zc} the superficial area of the adsorbent particles is deprotonated, so a negative charge is acquired (equation III.2) and that will reduce the adsorption of the anionic dyes which because of the repulsive forces [204].



In our case, the pH_{zc} were found to be 10.45 for LDH and 11.73 for CLDH. The highest capacities of adsorption were found in acidic medium that corresponds to the highest ζ -potential values (above 35mV). In alkaline conditions, the capacity of adsorption decreases due to the decrease of the zeta potential until reaching the lowest values.

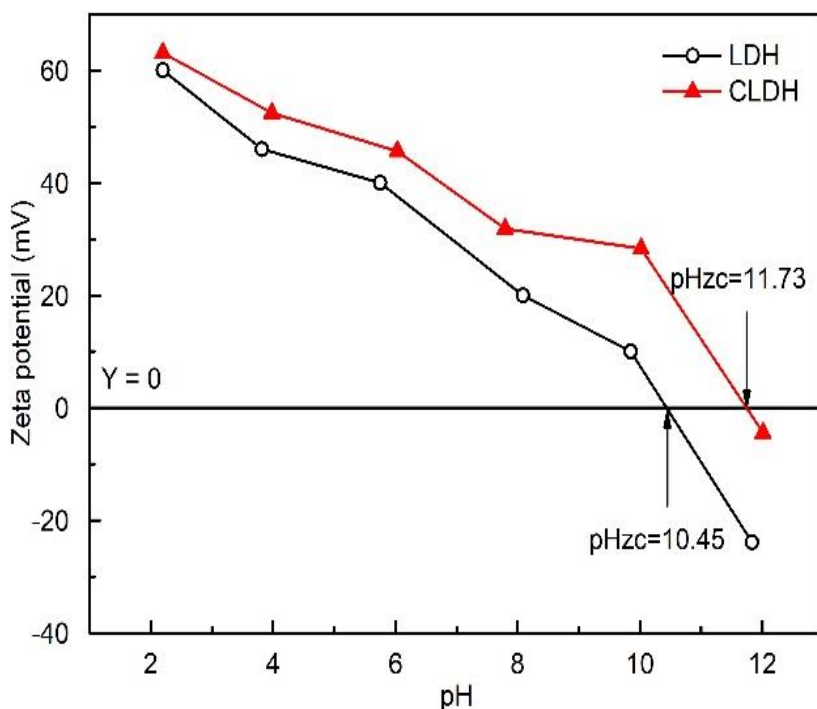


Figure.III.9. Zeta potential distribution of LDH and CLDH.

III.3.2.2 Effect of the adsorbent dosage

Figure.III.10 and Figure.III.11 present the variation of adsorption capacity and the removal yield of AR66 on LDH and CLDH, respectively, with adsorbents dosage varying from 0.2g.L^{-1} to 1g.L^{-1} . It can be observed that the adsorbent dosage affects strongly the efficiency of adsorption. As expected, the removal percentage of AR66 by the two adsorbents LDH and CLAH increased with the mass of adsorbent due to the more available active sites for adsorption (Figure.III.10). Whereas the capacity diminishes with the raise of the mass of adsorbent as the result of being calculated per mass unit, considering that the same quantity of AR66 is adsorbed on a larger adsorbent surface (Figure.III.11) and also may be due non-saturation of the active sites available for adsorption.

More than 75% of AR66 were removed using only 0.4g.L^{-1} of CLDH as adsorbent, while only an uptake of 30% was found for the same LDH dosage. A total dye removal was obtained using 0.8g.L^{-1} of CLDH while only 50% of dye removal was reached for the same dosage of LDH. This adsorbent dosage of 0.8g.L^{-1} was, therefore, subsequently considered.

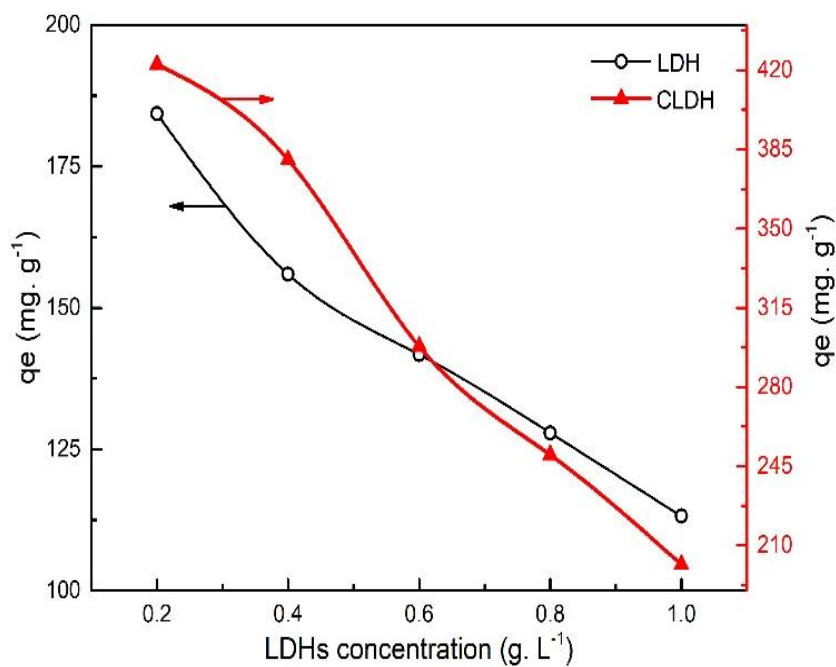


Figure.III.11. Effect of adsorbent dosage on dye adsorption capacity on LDH and CLDH.

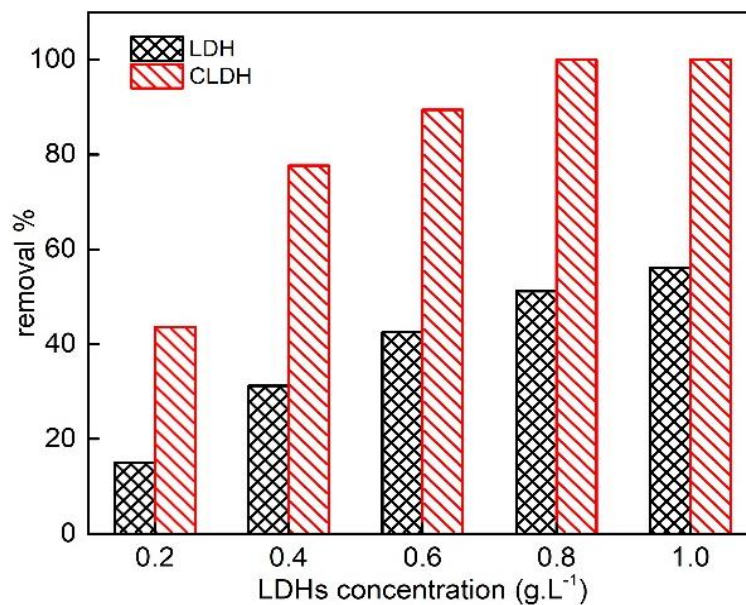


Figure.III.10. Variation of the removal percentage with the adsorbent dosage onto LDH ($C_0 = 200\text{mg L}^{-1}$) and CLDH ($C_0 = 800\text{mg L}^{-1}$) at $T = 23^\circ\text{C}$, speed = 250 rpm

III.3.2.3 Effect of the initial concentration and the contact time

Figure.III.12 displays the influence of the contact time on the adsorption capacity of AR66 onto LDH and CLDH at diverse initial concentrations of dye solution. It can be noticed that the amount of AR66 adsorbed increased rapidly in the beginning of the experiment; then the rate of adsorption decreased until the adsorption capacity reached equilibrium after a certain contact time which depends on the initial concentration (50 to 420 minutes). Moreover, as the initial

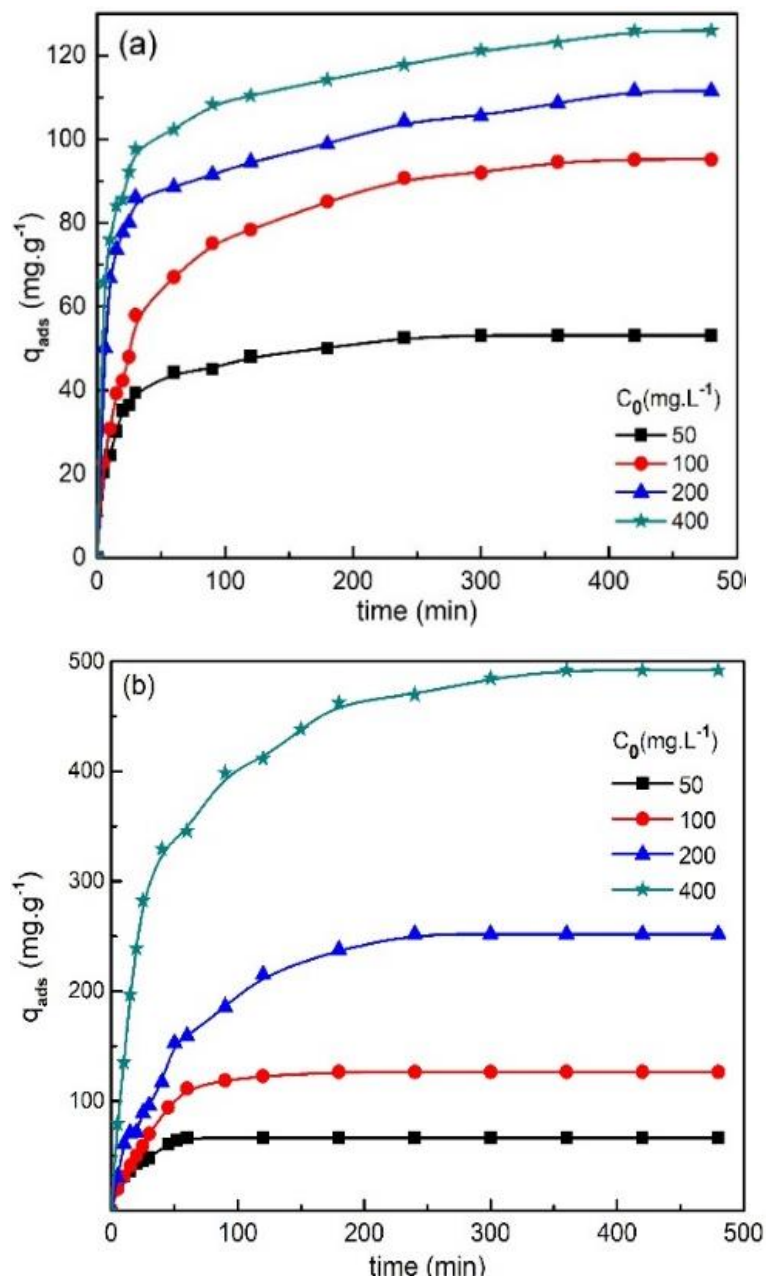


Figure.III. 12. Effect of contact time and initial dye concentration on dye adsorption on (a) LDH, (b) CLDH. (pH= 6.87, T= 23°C, speed= 250rpm)

concentration of the dye solution increased, the adsorption capacity of AR66 increased, taking more time to attain the equilibrium. This behavior can be demonstrated by the fact that at the beginning of the adsorption process, the adsorbent surface contains free active sites which are then progressively occupied by the dye molecules. Then, as the contact time increases, the adsorbent has less available active pores compared to the dye molecules. This latter starts to compete for the remaining active pores, accounting for the increase of the equilibrium time increases with the dye concentration.

III.3.2.4 Effect of coexisting ions on dye removal

In textile industries, during the dyeing process, different salts are being added [60]. For the reason that the ionic strength affects highly the properties of the solution, in this study, it was chosen as a one of the factors that have been taken into consideration. This factor (ionic strength) can affect positively or negatively the capacity of adsorption. Its influence relies on the behaviour of the adsorbent and the adsorbate towards the salt added. the effect of the different salts added (NaCl, Na₂CO₃, and Na₂SO₄) on the adsorption capacity of AR66 on LDH and CLDH is shown in Figure.III.13. It can be noticed that the capacity of adsorption on both adsorbents is affected by the addition of salt. The results show that the addition of salts promotes the capacity of adsorption as demonstrated by Figure.III.13. Many studies reported that the addition of salts decreases the capacity of adsorption because of the competition generated between the salt anions and the dye molecules [205]. It was reported by Wang et al.[206] that, theoretically, the increase in the ionic strength is supposed to decrease the adsorption capacity in adsorbent/ adsorbate system where the electrostatic forces attractive. However, the results in this study does not follow the theory. Similar cases were reported in several studies by Alberghina et al.[207] and Ip et al.[208] where the ionic strength had a positive effect on the capacity of anionic dyes adsorption. The increase in the capacity of adsorption with the increasing ionic strength could be due to the aggregation of the dye molecules which could be caused by different forces as reported in several studies [207], [208].

It has been reported by Alkan et al.[209] that for pH value lower than pH_{zc} (point of zero charge) the increase in the salt concentration and then the ionic strength promotes the capacity of adsorption. however, for pH higher than pH_{zc} the adsorption capacity is reduced [209].

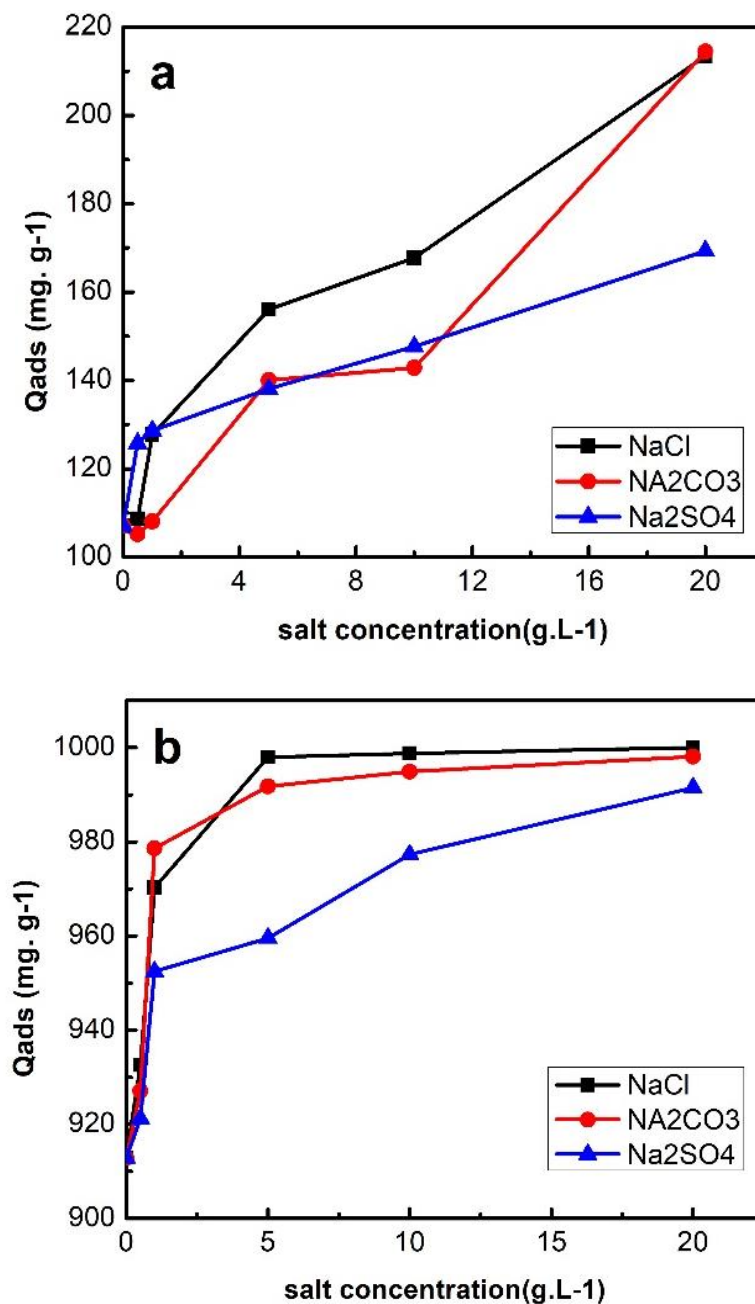


Figure.III.13. Effect of coexisting ions on dye removal by (a) LDH, (b) CLDH

III.3.3 Kinetic modeling

For each of the kinetic models applied (that are mentioned previously), the parameters were calculated to fit the kinetic data of the adsorption onto LDH and CLDH. These parameters as well as the coefficients of correlation of each model R^2 are reported in Table.III.3.

From Table.III.3, It can be observed that the pseudo-first order and Elovich models gave lower coefficients of correlation R^2 , for both LDH and CLDH, compared to the pseudo-second order model which presents very high correlation coefficients (above 0.99) showing the high accuracy of the pseudo-second order model to fit the empirical data.

Moreover, the calculated capacities of adsorption given by the pseudo-second order model (Q_e) were very close to the empirical capacities of adsorption (Q_{exp}) for all the concentrations considered; while pseudo-first order and Elovich models showed a large discrepancy between fitted and experimental data indicating a poor linear fitting. Therefore, the pseudo-second order is the most convenient model to define the adsorption kinetics of AR66 on LDH and CLDH with R^2 close to 1.

III.3.4 Adsorption mechanism

Figure.III.14 shows the plots of Q_t versus $t^{0.5}$ for LDH and CLDH. It could be seen that the intraparticle fitting plots for LDH present three straight lines all over the contact time range indicating that the adsorption process occurs in three main stages. The first region is ascribed to the external adsorption (boundary layer diffusion) where a diffusional transport of dye particles from the solution to the exterior surface of the LDH or CLDH occurred within the first moments of the adsorption process. The second stage is associated to the gradual intraparticle diffusion for which the rate controlling step is the intra-particle diffusion.

The intra-particle diffusion coefficients k_d and the coefficients of correlation R^2 of the intra-particle diffusion model fitting were calculated and summarised in Table.III.3. It can be revealed that the lines have non-zero intercept which proposes that the intra-particle diffusion is not the unique process controlling step. Furthermore, the intercept C increases with the initial concentration giving information about the boundary layer effect (as the intercept increases, the boundary layer effect increases).

The last region is assigned to the equilibrium stage where less adsorbate particles are remained in the solution with less available adsorbent active sites thus the intraparticle diffusion is slowing down. For the adsorption of AR66 on CLDH, the plots of q_t versus $t^{0.5}$ for the high concentration (200 and 400mg.L⁻¹) showed the same profile as those of LDH.

For lower concentrations (100mg.L^{-1} and 50mg.L^{-1}) the adsorption profile of AR66 on CLDH presented only two stages, a straight line followed by a plateau which indicates that the adsorption process for the low concentrations is a single step mechanism that can be restricted in the external surface adsorption followed by the equilibrium. Similar results were reported by Santos et al. [111].

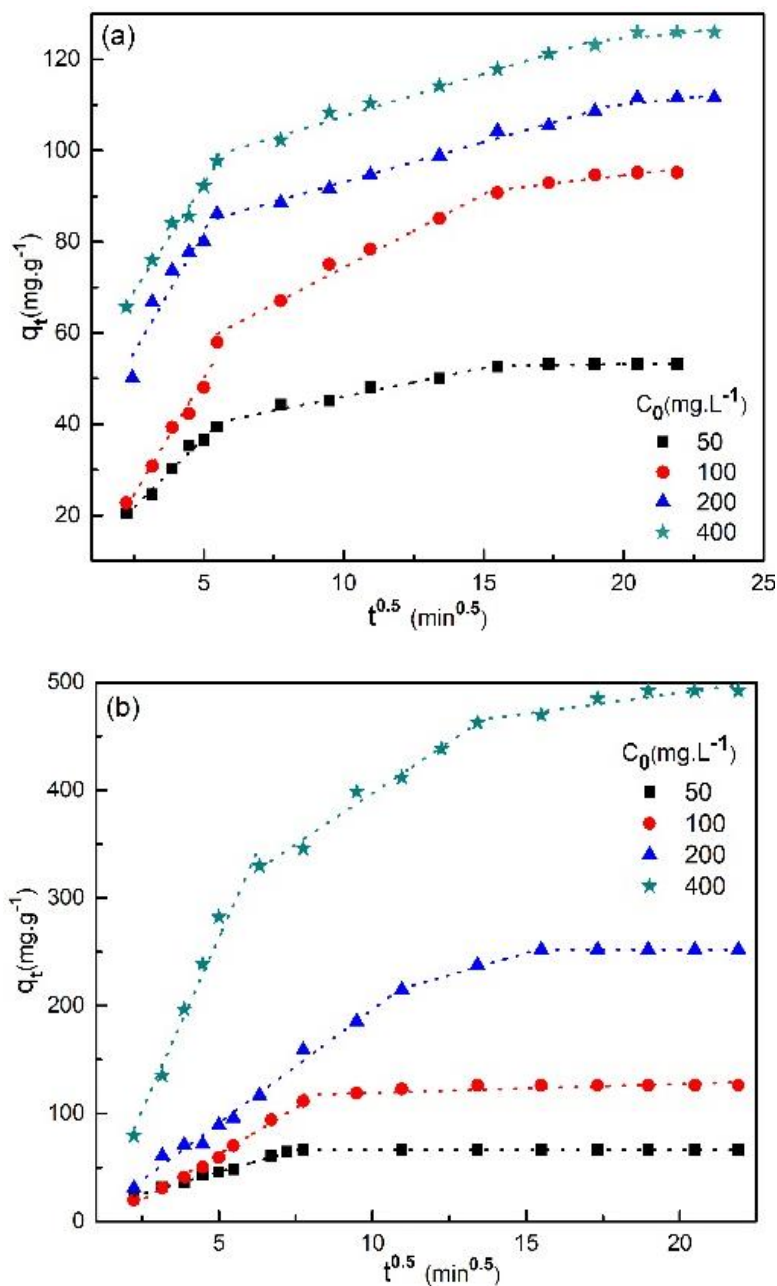


Figure.III.14. Data fitting of the AR66 adsorption kinetics by intra-particle diffusion model (a) LDH, (b) CLDH.

Table.III.3. Kinetics model parameters for AR66 adsorption and coefficient of correlation R^2

T= 24±1°C (room temperature), pH ≈ 6.80					
	C (mg. L ⁻¹)	50	100	200	400
LDH	Experimental data				
	$q_{exp}(mg.g^{-1})$	53.16	95.17	111.55	125.95
	Pseudo-first order model				
	$k_1 (min^{-1})$	0.0155	0.0111	0.0082	0.0082
	$q_e (mg.g^{-1})$	30.54	66.19	48.99	51.80
	R ²	0.9414	0.9664	0.9470	0.9517
	Pseudo-second order model				
	$k_2 (g.mg^{-1}min^{-1})$	1.43 10 ⁻³	3.96 10 ⁻⁴	6.67 10 ⁻⁴	6.84 10 ⁻⁴
	$q_e (mg.g^{-1})$	54.64	99.01	112.36	126.58
	R ²	0.999	0.999	0.998	0.999
	Elovich model				
	$\alpha (mg.g^{-1}min^{-1})$	24.70	12.52	69.09	89.13
	$\beta (g.mg^{-1})$	0.124	0.059	0.066	0.058
	$q_e (mg.g^{-1})$	68.87	110.10	127.23	144.88
	R ²	0.971	0.987	0.911	0.899
	Intra-particle diffusion model				
	$K_i(mg.g^{-1}min^{-0.5})$	1.25	3.2	1.75	1.87
C	33.5	42	75.62	88.79	
R ²	0.96	0.98	0.99	0.98	
CLDH	Experimental data				
	$q_{exp}(mg.g^{-1})$	66.25	126.64	256.36	499.05
	Pseudo-first order model				
	$k_1(min^{-1})$	0.0674	0.023	0.0259	0.0259
	$q_e (mg.g^{-1})$	80.37	99.64	297.91	521.96
	R ²	0.950	0.941	0.962	0.707
	Pseudo-second order model				
	$k_2 (g.mg^{-1}min^{-1})$	1.83 10 ⁻³	3.14 10 ⁻⁴	7.88 10 ⁻⁵	7.1610 ⁻⁵
	$q_e (mg.g^{-1})$	67.57	133.33	271.78	516.32
	R ²	0.999	0.997	0.998	0.999
	Elovich model				
	$\alpha (mg.g^{-1}min^{-1})$	12.08	9.76	13.34	57.14
	$\beta (g.mg^{-1})$	0.062	0.030	0.016	0.011
	$q_e (mg.g^{-1})$	95.29	163.06	287.73	547.30
	R ²	0.940	0.925	0.911	0.978
	Intra-particle diffusion model				
	$K_i(mg.g^{-1}min^{-0.5})$	/	/	8.17	19
C			126.26	207.17	
R ²			0.99	0.98	

III.3.5 Equilibrium modeling

Experimental isotherm data of AR66 adsorption on LDH and CLDH at room temperatures are represented in Figure.III.15. It could be seen that the capacity of adsorption Q_e rises with the raise of dye concentration C_e until reaching an equilibrium (called plateau of isotherm) that corresponds to the maximum of adsorption for which the surface of adsorption is saturated. The maximum adsorption capacity obtained was around 125 mg. g^{-1} for LDH, while it is noteworthy

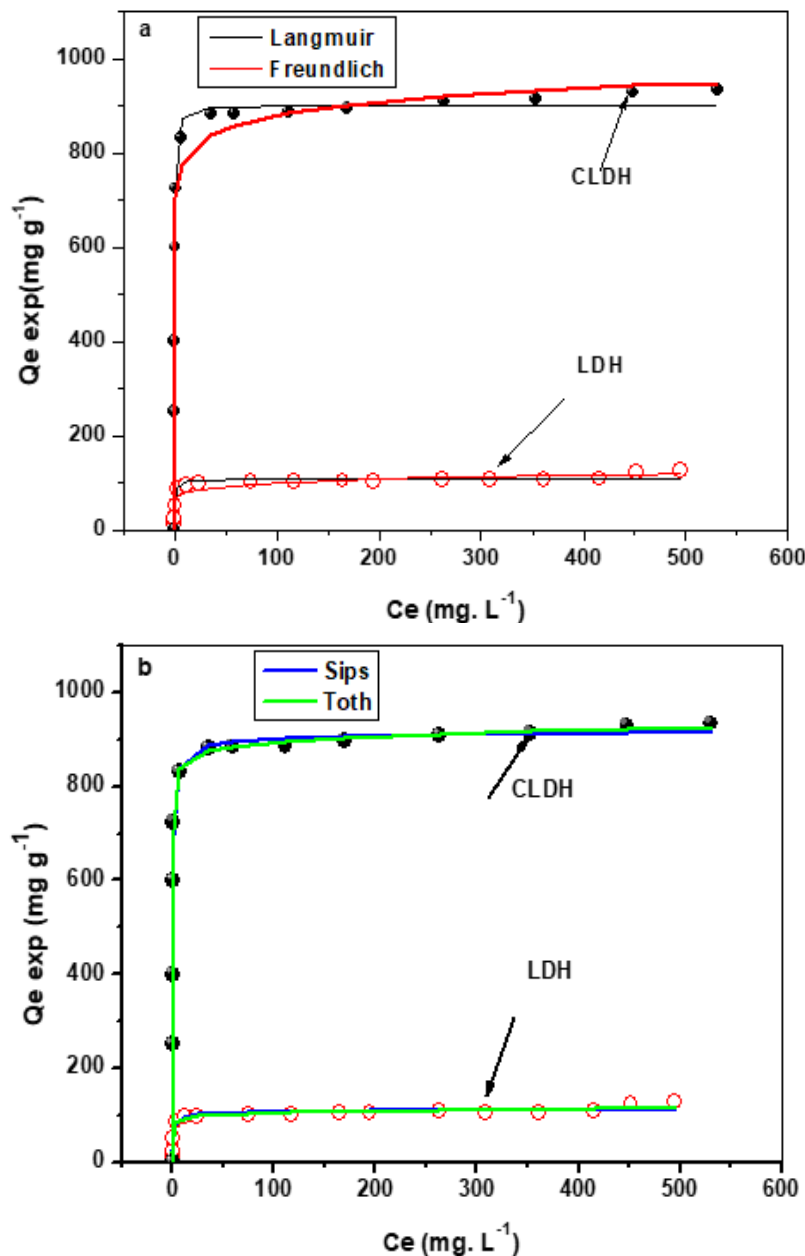


Figure.III. 15. Non-linear regression of isotherm experimental data with: (a) Langmuir, and Freundlich and models (b) Sips and Toth models.

that much higher values was reached for CLDH with a maximum estimated to be more than 930 mg.g⁻¹. Experimental data were fitted to Langmuir, Freundlich, Sips and Toth models (Figure.III.15).

The parameters of each model were calculated as well as their coefficients of correlation R² and Residual Mean Square Error (RMSE). The results are summarized in Table.III. 4. According to the R² values, it can be noticed that the Freundlich model exhibited the lowest coefficient of correlation and the highest RMSE leading to a poor regression in comparison with the other models.

Table.III. 4 Langmuir, Freundlich, Sips and Toth parameters for AR66 adsorption on LDH and CLDH

Model	parameter	LDH	CLDH
Experimental	q _m (mg. g ⁻¹)	125.22	931.24
	K _L (L. mg ⁻¹)	1.759	4.908
Langmuir	q _m (mg. g ⁻¹)	107.31	901.54
	R _L	0.0014	0.0002
	R ²	0.935	0.994
	RMSE	61.14	36.46
Freundlich	K _F (L. mg ⁻¹)	61.86	711.46
	n	9.563	21.67
	R ²	0.887	0.972
	RMSE	76.75	49.3
Sips	K _S (L. mg ^{-m})	1.488	9.255
	q _m (mg. g ⁻¹)	105,51	922.51
	m	0.604	0.552
	R ²	0.958	0.997
	RMSE	58.62	32.13
Toth	K _T (mg. g ⁻¹)	83.99	823.87
	a _T (L. mg ⁻¹)	0.264	0.1331
	t	1.0502	1.0187
	R ²	0.960	0.999
	RMSE	52.55	21.24

Langmuir model showed relatively higher R^2 and lower RMSE suggesting a better fit to experimental data. The separation factor (R_L) was less than the unit indicating a favorable monolayer adsorption of AR66 on homogenous surface of LDH and CLDH.

For LDH, the Sips and Toth models showed the highest R^2 values ($R^2 > 0.95$) that correspond to the lowest RMSE suggesting that the Sips and Toth were the most suitable models to describe the adsorption of AR66 on LDH. Regarding CLDH, even if all models except the Freundlich model, showed high R^2 values, the Sips and Toth models led to the highest R^2 values and exhibited the lowest RMSE confirming that they were the most adequate models to fit adsorption isotherm data of AR66 on LDH and CLDH adsorbents. The adsorption on CLDH can be also described by Langmuir model.

Table.III. 5 reports few adsorption capacity maximums of various dyes on different adsorbents that have been reported previously. From Table.III. 5, It could be seen that, in comparison to other adsorbents, CLDH synthesized in this work can be considered as a promising adsorbent to remove anionic dyes, including AR66, from wastewater. Indeed, the CLDH gives an extremely high capacity of adsorption of AR66.

Table.III. 5. Comparison of the maximum of adsorption capacities reported for dye adsorption on CLDH

Material	dye	pH	Initial concentration	Q_{\max} (mg. g ⁻¹)	Reference
Mg-Fe	Acid brown 14	6	80	59.4	[101]
Mg-Al	Acid Red 66	5	50	99.9	[13]
Mg-Al	Congo red	6.5	200	143.27	[106]
Mg-Al	Acid Green 68:1	7	600	154.8	[103]
Ni-Fe	Congo red	6	50	330	[210]
Mg-Fe	Orange G	5.4	400	378.8	[74]
Mg-Al	Remazol Golden Yellow	7	400	657.2	[211]
Mg-Cu-Al-Fe	Acid Red 66	6.76	500	931.24	This work
Mg-Al	Acid Yellow 42	4	1000	1265.9	[111]

III.3.6 Adsorption thermodynamics

The thermodynamic parameters reveal the possibility and the spontaneity of the process. The study of the variations of the constants of equilibrium with the temperature enables us to estimate the thermodynamic parameters, essentially the Gibbs free energy change (ΔG°), the enthalpy change (ΔH°) and the entropy change (ΔS°).

ΔH and ΔS were derived from the slope and the intercept of the linear graph of $\ln (\rho K_C)$ vs $1/T$, respectively. Table.III. 6 gives the obtained ΔG° , ΔH° and ΔS° . The ΔH° obtained was positive, for both LDH and CLDH, demonstrating that the dye is endothermically adsorbed on LDH and CLDH. However, ΔH° obtained for LDH was lower than the enthalpy found for CLDH, suggesting that the adsorption of AR66 on LDH was less endothermic compared to the AR66 adsorption on CLDH. Furthermore, the ΔG° for both adsorbents at different temperatures was found to be negative, which confirms the spontaneity of the process. $\Delta S^\circ > 0$ revealed a raising randomness at the interface between the solid and the liquid during the sorption of AR66.

Table.III. 6. Thermodynamic parameters of AR66 adsorption onto LDH and CLDH.

	ΔH° (kJ.mol ⁻¹)	ΔS° (J.K ⁻¹ mol ⁻¹)	ΔG° (kJ.mol ⁻¹)			
			10°C	20°C	30°C	40°C
LDH	11.79	67.79	-13.40	-14.08	-14.76	-15.44
CLDH	19.49	126.53	-16.34	-17.60	-18.87	-20.13

III.4 Conclusion

In conclusion, a new layered double hydroxide composed of four metals; Mg-Cu-Al-Fe - LDH was successfully synthesized using the coprecipitation method at constant pH. It has been demonstrated that LDH is an efficient adsorbent for the anionic dye AR66. The textural properties obtained for LDH and CLDH demonstrate that the calcination increased the specific surface area by the release of water and carbon dioxide forming larger pores and free surfaces. The adsorption yield of AR66 on both LDH and CLDH was affected by the experimental conditions, mainly the solution pH, the adsorption dosage, the contact time and the initial dye concentration. The calcination of Mg-Cu-Al-Fe-LDH has greatly improved the capacity of adsorption giving a competitive adsorbent (CLDH) with very high capacity of adsorption

compared to the CLDHs reported in the literature. The maximum adsorption capacity of CLDH was found to be seven times higher than that of LDH (931.5 mg. g⁻¹ vs 125.2 mg. g⁻¹). Indeed, the thermal treatment results in more and larger pores. Adsorption kinetic data were found to follow a pseudo-second order model. Sips and Toth models defined accurately the isotherm data. The thermodynamic parameters revealed that the adsorption of AR66 on both LDH and CLDH is spontaneous and endothermic. The electrostatic forces are the main forces responsible for the AR66 adsorption on LDH and CLDH. The low values of ΔH° obtained are in agreement with the proposition that the adsorption process on LDH and CLDH is physisorption. The thermodynamic study revealed that the adsorption is endothermic and spontaneous.

Chapter IV

The removal of anionic dyes from wastewater onto zeolite Na-P synthesized from waste coal fly ash

IV.1 Introduction

Recently, there has been a growing interest in the use of industrial waste to synthesis ecofriendly materials used as effective adsorbents [20]. The valuation of these unused sources (industrial waste) is of great interest since it contributes to diminish environmental pollution by reducing the pile of industrial waste and, then, exploiting that waste for water treatment purposes. The coal fly ash is a by-product generated from coal burning in combustion power plants. It constitutes more than 70% of the combustion solid residues [21]. One of the best ways to recycle the coal fly ash collected after the combustion process is its use for the synthesis of new materials useful in other fields such as pollutants removal.

In this study the zeolite Na-P was synthesised by the microwave assisted conversion of a CFA that has been undergone a double pre-treatment before being subjected to the microwave. The obtained product was characterized by XRD, FTIR, TGA/DTA, SEM, XRF, BET and Zeta potential. The obtained zeolite was applied to remove the anionic dye Acid Red 66 (AR66) from wastewater. An experimental design methodology was adopted to explore the adsorption of the AR66 on the zeolite Na-P and to optimize the experimental conditions to maximize the dye removal. For a thorough study, the kinetics, isotherms and thermodynamic adsorption studies were realized, and different mathematical models were tested to fit experimental data to better understand the adsorption mechanism. A part of this work has been published in the proceeding of the international chemical and biochemical engineering conference which took place in Stockholm, Sweden (December 2018) and has been chosen as the best conference paper (trophy of excellence).

IV.2 Materials and methods

IV.2.1 Characterization

The scanning electron microscopy (SEM) of the raw CFA particles was obtained by JSM 600F microscope (Joel, Japan) at an acceleration voltage of 10 keV. The X-ray diffraction data (XRD) of the raw CFA and the prepared zeolite were obtained, in the range of 2θ from 0° to 40° , by mean of Rigaku-MiniFlex powder diffractometer (Japan) under $\text{Cu(K}\alpha\text{)}$ radiation ($\lambda = 1.54059 \text{ \AA}$). Bruker vector 22 spectrometer was used to collect Fourier transform infrared spectra (FT-IR) of the zeolite before and after adsorption in the range of wavenumber from 400

to 4000 cm^{-1} . The surface imaging of the raw CFA and the zeolite were carried out by Hitachi S-3000N scanning electron microscope (SEM). The thermogravimetric and differential thermal analysis (TGA/DTA) were recorded on Mettler Toledo analyzer (851e model, Switzerland) equipped by the software 6.1 Stare. For the thermal analysis, a weighed mass of the zeolite was heated inside the analyzer furnace from ambient temperature to 600°C under a nitrogen purge of $30\text{ mL}\cdot\text{min}^{-1}$ with a heating speed of $10^{\circ}\text{C}/\text{min}$. The point of zero charge (pH_{ZC}) of the zeolite was determined by the Zeta potential measurements at different pH. For this purpose, fixed amounts of the zeolite particles were dispersed in 20 ml of DI water at different pH (2-10). The Malvern Zeta Sizer 3000 (UK) was used to analyses the zeta potential of each suspension. Then, the pH_{ZC} that corresponds to the pH value for which the zeta potential is nil was determined.

IV.2.2 Adsorption experiments

For the adsorption of AR66 on ZNa-P, the batch mode was adopted to perform the adsorption experiments following an experimental design. The experiments were performed by adding a given adsorbent mass ($0.2\text{-}0.5\text{ g}\cdot\text{L}^{-1}$) to 50 mL of the dye solution with a known concentration ($200\text{-}1000\text{mg}\cdot\text{L}^{-1}$) and a controlled pH (2-4). The adsorption experiments were conducted on a magnetic stirrer under a controlled speed of 200 rpm. After the predetermined time of the experiment was achieved (5-25min), the solution was centrifuged to separate the solid from the liquid and stop the adsorption progress. All experiments were carried out at room temperature ($T\approx 24\pm 1$) except for the experiments where the effect of the temperature was considered.

While the adsorption of AR66 on ZNa-P was performed using an experimental design, the investigation of the effect of the different parameters on the adsorption of CR on ZNa-P was carried out using the conventional method.

The kinetics of the adsorption was also studied for different initial dye concentrations ($250\text{-}2000\text{mg}\cdot\text{L}^{-1}$) at room temperature. A mass of 80 mg of ZNa-P was put in contact with 200 mL of the dye solution. The mixture was magnetically stirred at 200 rpm and room temperature. Samples (1mL) were regularly taken from the mixture until the equilibrium was established. The adsorption isotherms were also investigated by adding 20 mg of ZNa-P to 50 mL of dye solutions with different initial concentrations ($50\text{-}3000\text{ mg/L}$), at room temperature and fixed

stirring speed of 200 rpm. The adsorption was also thermodynamically studied by the investigation of the effect of the temperature (10-40°C); a mixture of 50 mL of dye solution (1000 mg.L⁻¹) and 20 mg of ZNa-P were stirred on a magnetic stirrer equipped with a thermostat to keep the temperature fixed at the desired value (10-40°C).

IV.2.3 Experimental design

While the investigation of the effect of different parameters of the CR adsorption on ZNa-P was performed using the conventional method a Design-Expert 7.0.0 software was applied to perform a design of experiment (DOE) for the study of AR66 adsorption onto ZNa-P. The central composite design (CCD) was the RSM design applied to realise the DOE followed throughout this study. The CCD proposes five variation levels for each independent experimental factor: $-\alpha$, -1, 0, 1 and $+\alpha$. For n experimental factors, the CCD is characterized by a total number of experiments N (IV.1), divided in three series of points: 2^n factorial points, $2n$ axial points and 6 replicated center points.

$$N = 2^n + 2n + 6 \quad \text{IV. 1}$$

In this study, four independent numeric variables were selected, namely the initial pH of the solution (2-4), the initial concentration of dye solution C_0 (200-1000mg/L), the adsorbent dosage m (0.2-0.6mg/g), and the contact time t (5-25min) as it is displayed in Table.IV.1. The variables were coded X_1 , X_2 , X_3 and X_4 respectively. The response (R) studied and to be optimized, in this work, was the adsorption capacity of the dye on ZNa-P.

The CCD allows to develop a regression between the response R and the different parameters X_1 , X_2 , X_3 and X_4 . To evaluate the quality of the regression, the analysis of variance ANOVA was applied. The correlation coefficients R^2 and adjusted R^2 are also useful parameters to check the fitting quality. The model statistical significance was demonstrated based on the obtained F-value (Fisher variation ratio) and P-value (probability). The significance of each independent factor as well as the interaction factors was assessed using the P-value obtained for the corresponding term. For a better understanding of the response – variables relationship, the RSM offers 2D and 3D graphical plots to express the single and coupled effects of the variables on the measured response.

Table.IV.1 The independent variables and their coded levels using CCD

Factor	- α Level	-1 Level	0 Level	1 Level	+ α Level
X ₁ : pH	2	2.5	3	3.5	4
X ₂ : C ₀ (mg/L)	200	400	600	800	1000
X ₃ : m (g/L)	0.2	0.3	0.4	0.5	0.6
X ₄ : t (min)	5	10	15	20	25

IV.3 Results and discussion

IV.3.1 Characterization of the adsorbent

The XRD patterns of the raw CFA and the synthesized ZNa-P were collected and presented in Figure.IV.1. It can be observed that the CFA contained mainly crystalline phases: quartz (Q), mullite (M), hematite (H) and calcite (C). The comparison of the XRD patterns of the raw CFA and the obtained product evidently shows that a new product was formed. In fact, the peaks corresponding to some of the CFA crystalline phases disappeared ($2\theta = 9.4^\circ, 15.92^\circ, 21.01^\circ$,

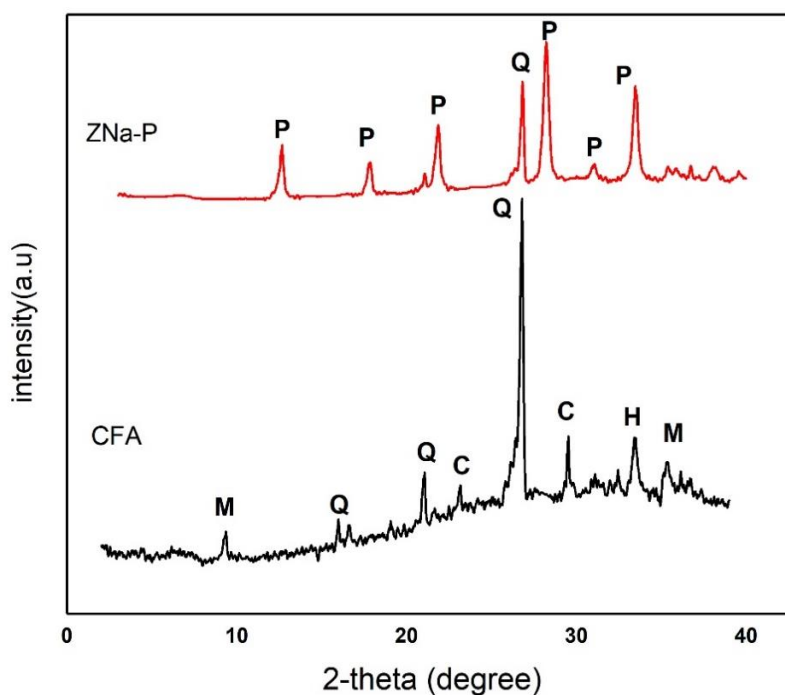


Figure.IV.1. The XRD patterns of CFA and ZNa-P (Q: Quartz, M: Mullite, H: Hematite, C: Calcite, P: zeolite P)

23.12° and 29.54°), while the appearance of other crystalline phases specific peaks can be noted, as for instance at $2\theta = 12.68^\circ$, 17.86° and 28.26° . The decrease in the intensities of some peaks may be due to the dissolution of the corresponding phases in the alkaline solution during the conversion. The identification of the XRD patterns of CFA after the conversion was made by comparison with the zeolite database [212]. The characteristic peaks of ZNa-P appeared at $2\theta = 12.68^\circ$, 17.86° , 21.86° , 28.22° , 31.08° and 33.48° (JCPDS file no. PDF#97-000-9550) confirming that the zeolitization successfully occurred and the zeolite obtained was a zeolite P.

The FT-IR of the raw CFA and ZNa-P before and after dye adsorption are represented in Figure.IV.2. The changes in the peaks observed on the ZNa-P FT-IR pattern in comparison with the raw CFA pattern showed that the CFA successfully underwent a conversion as demonstrated previously by the XRD results. Most of the peaks observed in CFA pattern are still present in the ZNa-P pattern with a decrease in their intensities and a slight shifting in their position which is the case for the peaks at 1216.86 , 1367.28 and 1741.41 cm^{-1} . The peak at 3761 cm^{-1} may be attributed to the O-H stretching vibration arising from the Si-OH groups in the mullite phase [213]. The peaks in ZNa-P FT-IR spectrum were similar to the peaks reported previously by

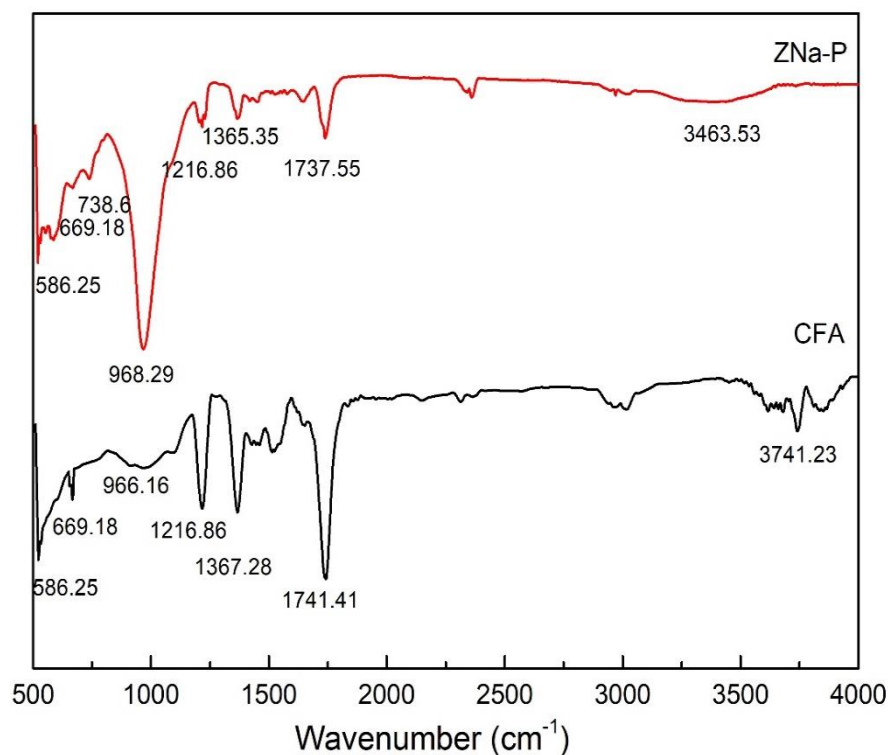


Figure.IV.2. The FT-IR spectrum of the raw CFA and the ZNa-P

Flanigen et al. [214]. The main vibration peak appeared at 968.29cm^{-1} corresponded to the asymmetric stretching of internal tetrahedra $\text{SiO}_{4/2}$ and $\text{AlO}_{4/2}$ [215]. The double ring external linkage vibration gave rise to a peak at the wavenumber 586.25cm^{-1} . The peaks at 669.18cm^{-1} and 738.6cm^{-1} can be assigned to the internal and the external tetrahedral symmetrical vibration of (Si-O and Al-O), respectively. The peak observed at 1646cm^{-1} and the weak broad peak at 3463.53cm^{-1} were attributed to the H-O-H bending of the adsorbed water molecules.

The results of the elemental composition analysis of the ZNa-P are represented in Table.IV.2. It could be observed from Table.IV.2 that the major components of the ZNa-P are silicon dioxide (SiO_2) and aluminium oxide (Al_2O_3) forming aluminum silicate compound. A big similarity is observed when comparing the chemical composition of ZNa-P (Table.IV.2) with the composition of raw CFA (Table.II.1) where almost the same compounds appeared in both materials. The XRF results show that the major component present in ZNa-P structure, after SiO_2 and Al_2O_3 , is Na_2O demonstrating that the exchangeable ions are sodium cations Na^+ .

Table.IV.2. Chemical composition of the synthesized ZNa-P

Element	Na_2O	MgO	Al_2O_3	SiO_2	CaO	Fe_2O_3	SrO	ZrO_2
wt. %	11.7	1.05	27.0	51.4	4.94	3.74	0.137	0.0344

The thermal stability of ZNa-P was studied using the thermal analysis. The thermogravimetric analysis (TGA) and the differential thermal analysis (DTA) are displayed in Figure.IV.3. The results of TGA/DTA were obtained in the range of temperature of $23\text{--}700^\circ\text{C}$. The TGA results show that the weight loss occurred in three main steps. In the range of temperature from 23°C to 700°C the ZNa-P lost around 20% from its total initial weight, while only 5% of weight loss was recorded for the raw CFA [26] indicating the high holding capacity of ZNa-p in water in comparison with CFA. The DTA thermogram revealed that in the temperature range of $50\text{--}160$ there was two weight losses: the first corresponds to the shoulder at 66.75°C and the second is the endothermic peak clearly observed at the temperature of 121.67°C . The weight loss in this range ($50\text{--}160^\circ\text{C}$) is associated to the loss of the weakly bound water and the water located in the zeolite cavities [216]. Another endothermic peak is observed at 473.33°C which may be caused by the destruction of the zeolite structure.

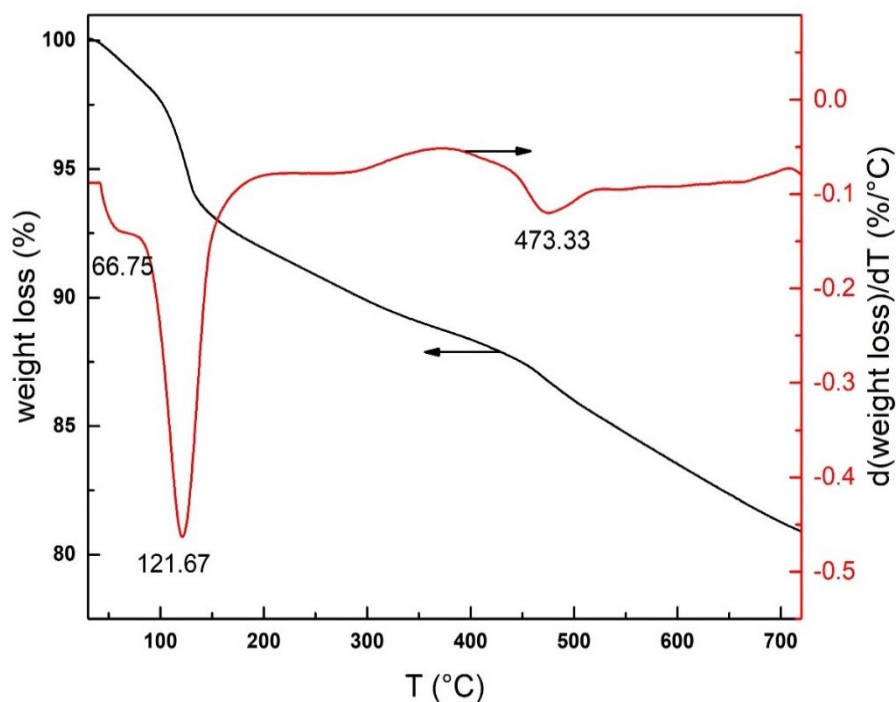


Figure.IV.3. The thermogravimetric and the differential thermal analysis of ZNa-P

The nitrogen adsorption-desorption results of the ZNa-P sample are represented in Figure.IV.4 and the structural properties are displayed in Table.IV. 3. The specific area of the ZNa-P was found to be $378 \text{ m}^2/\text{g}$ much higher than the surface area of the raw coal fly ash which is about $15.47 \text{ m}^2/\text{g}$. That means that the method of synthesis used in this study allows to obtain a product with a surface area ~ 24 times higher than the starting raw material. The N_2 adsorption desorption isotherm is of type II according to the International Union of Pure and Applied Chemistry (IUPAC) isotherm classification [162]. Moreover, the figure.IV.4 shows H3 hysteresis loop which is typical of plate-shaped particles aggregates giving rise to slit-shaped mesopores. The pore volume and the pore size of the ZNa-P were $1.63 \text{ cm}^3/\text{g}$ and 199.65 \AA respectively. The structure of zeolites consists on tetrahedral units formed by Si and Al surrounded by four atoms of oxygen. Since the Si-O and Al-O do not occupy fully the space, the porosity increases by the formation of cavities resulting in higher surface area. The textural properties of the ZNa-P synthesized after heat and acid treatments of the CFA were found to be greater than the structural properties of zeolites P obtained by other methods such as conventional method [138] or after only an acid treatment [217].

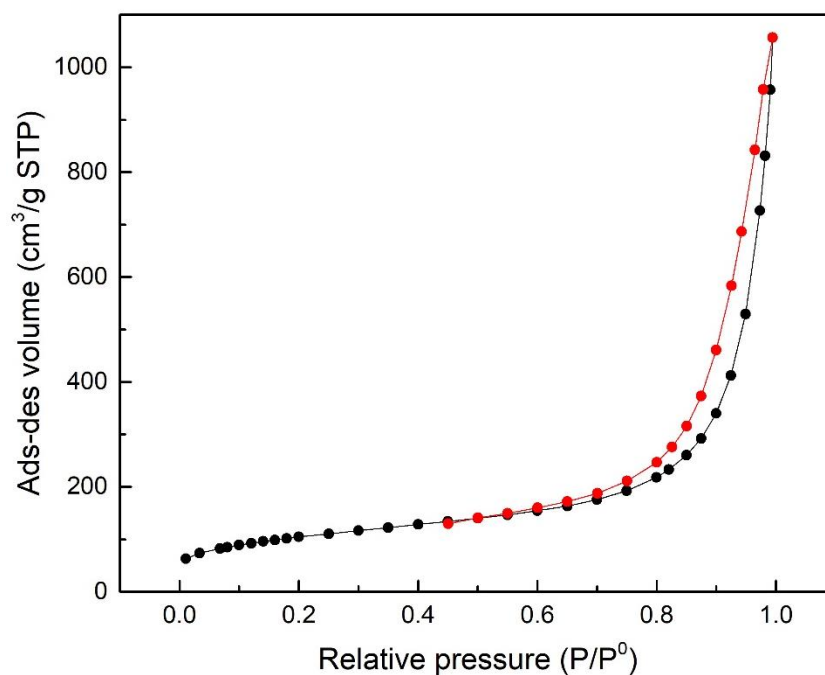


Figure.IV.4. N₂ adsorption-desorption isotherms of ZNa-P

Table.IV. 3 Textural properties of ZNa-P

Surface area (m ² /g)	Pore size (Å)	Pore volume (cm ³ /g)
378.06 m ² /g	199.65 Å	1.63 cm ³ /g

The scanning electron microscopy (SEM) images of the raw CFA and the ZNa-P are presented in Figure.IV.5. The surface morphology of the CFA showed spherical particles of different sizes with smooth surfaces (Figure.IV.5 (a)) while the observation of ZNa-P under SEM (Figure.IV.5 (b and c)) exhibited a rugged surface with the formation of protrusions homogeneously scattered on the surface.

Figure.IV.5 (a) reveals that the ZNa-P crystals were formed on the surface of the CFA particles with uniform distribution. The changes observed in the surface morphology approved the formation of zeolitic substances as demonstrated by XRD patterns. The structure of ZNa-P obtained from CFA conversion consisted of polycrystals formed of small plates and appeared under SEM in pseudo spherical forms [154].

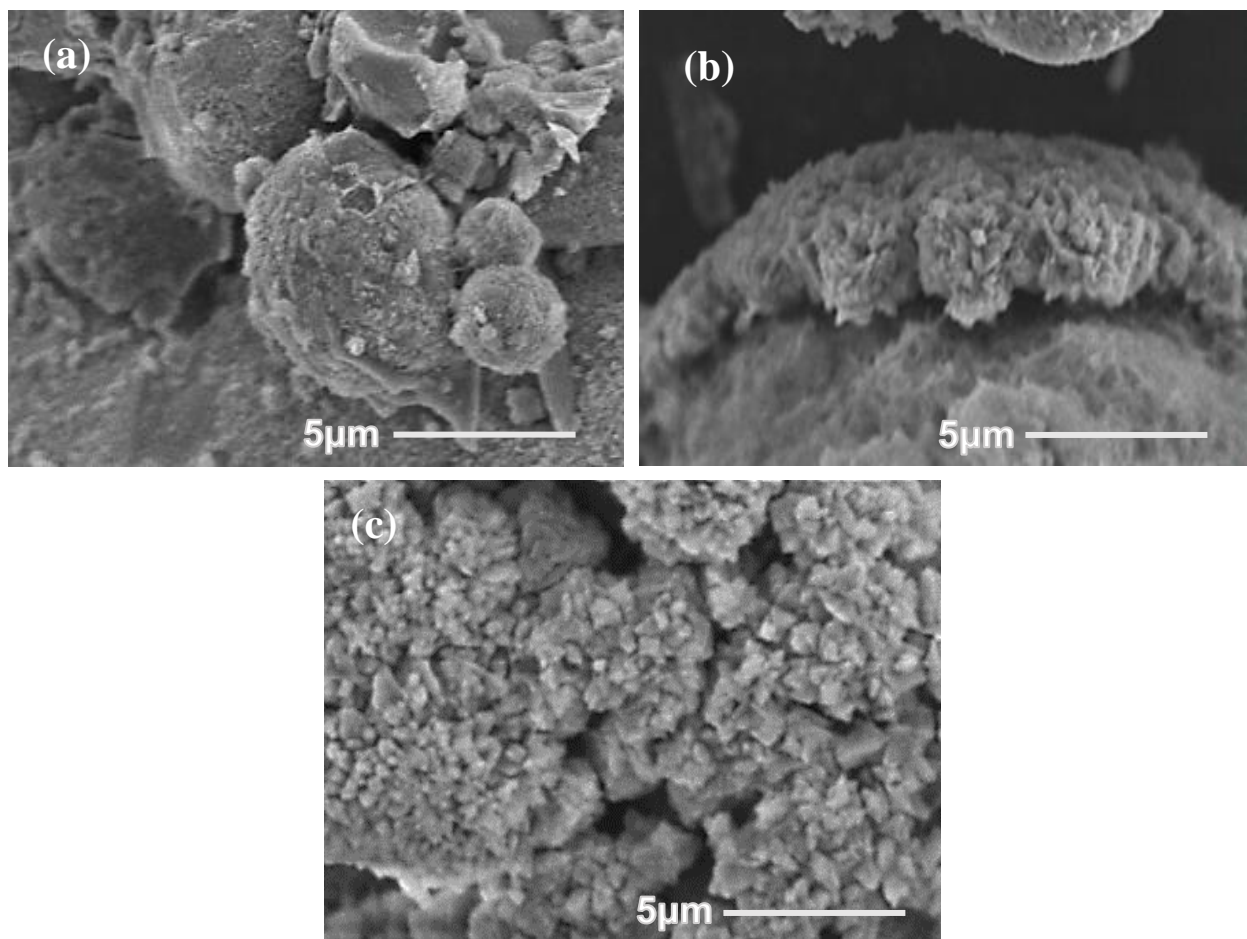


Figure.IV.5. SEM images of (a) CFA, (b) and (c) ZNa-P

IV.3.2 Study of the Adsorption of CR on ZNa-P

IV.3.2.1 The effect of the pH

The pH of the solution is an important factor in adsorption. It has a strong effect on the capacity of adsorption as it can change the charge of the adsorbent surface by changing the degree of dissociation of the functional groups (active sites) and/or changing the degree of ionization of the adsorbate. As a result, the adsorbed quantity will depend strongly on the pH of the solution.

The effect of the pH on the adsorption of CR on ZNa-P is represented in Figure.VI.6. It is obvious that the capacity of adsorption of CR on ZNa-P is highly affected by the pH of the solution. The capacity of CR adsorption is promoted at very acid solution where it can reach 2500mg.g⁻¹ which corresponds to a total removal of CR from the aqueous solution (C_0

$=1000\text{mg.L}^{-1}$). The capacity of adsorption decreases while the pH increases, and the lowest capacities of adsorption were reached at pH higher than 6. The alkaline solution is not favorable for a good removal of CR on ZNa-P.

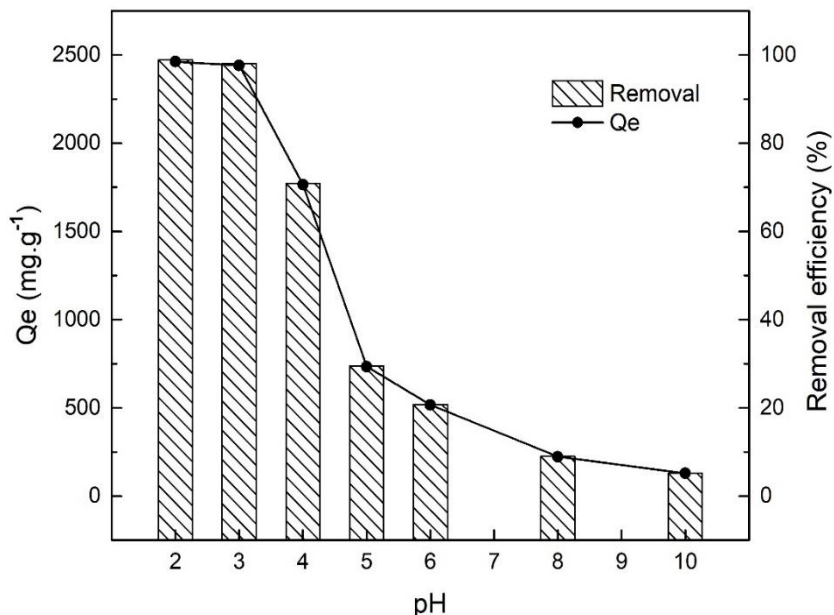


Figure.IV.6. The effect of pH on the capacity of adsorption of CR on ZNa-P

These results can be explained by considering the surface of the ZNa-P as well as the structure of the CR. The surface charge of the adsorbent has a direct relation with its point of zero charge (pH_{zc}). The pH_{zc} of the ZNa-P was found to be 5.65, thus the ZNa-P surface, at pH < pH_{zc} is positively charged while for pH > pH_{zc} the ZNa-P surface is negatively charged. Moreover, at pH > pK_a, the CR molecules exist in their anionic form whereas for pH < pK_a the CR molecules take the cationic form. It is of great interest to mention that during experiments, it was observed that the zeolite at acidic medium tends to increase the pH of the solution. The increase in the pH of the solution, generated by the zeolite in acid medium, is attributed to the ion exchange property of zeolites. Where the protons are exchanged with the Na⁺ cations of the ZNa-P structure [218]. As the pK_a of the CR is around 3.7 [219], the pH of the medium where the adsorption is conducted was always higher than the pK_a of the CR. Therefore, the adsorption which occurs between the positively charged surface and the anionic form of the CR is favored at acid pH. As the pH increases, the number of negative sites increases, and the surface becomes negatively charged. Then, the electrostatic repulsion of the anionic dye with negative charges

can be favored leading to the decrease in the adsorption capacity of CR. Similar behavior was observed by Vimonses et al. [220]. The pH of the solution used to study the adsorption of CR on ZNa-P in further experiments was fixed at pH=3.

IV.3.2.2 The effect of the adsorbent mass

The effect of the mass adsorbent on the capacity of adsorption of CR on ZNa-P was investigated by changing the mass of ZNa-P from 0.1 to 0.5 mg.L^{-1} . The experiments were carried out using an initial dye concentration of 1000mg.g^{-1} at pH=3 and room temperature. The capacities of adsorption obtained after equilibrium for different adsorbent masses are displayed in Figure.IV.7. It could be observed from Figure.IV.7 that the removal of the CR increases with the increase of the adsorbent mass which can be easily explained. In fact, using larger mass of adsorbent means increasing in the surface and therefore more active sites are available to adsorb more dye molecules. However, the increase in the mass of adsorbent decreases the capacity of adsorption which is calculated per unit of mass. This may be due to the non-saturation of the active sites available for adsorption. The adsorbent dosage of 0.4g.L^{-1} was adopted to accomplish the adsorption study of the CR on ZNa-P

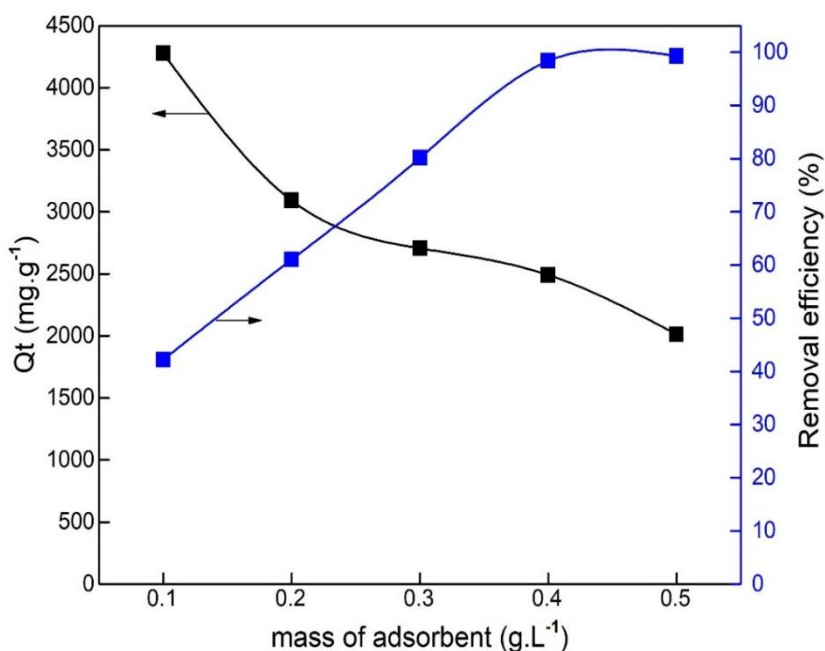


Figure.IV.7. The effect of the adsorbent mass on the adsorption of CR on ZNa-P

IV.3.2.3 The effect of the initial concentration and the contact time

The effect of the initial dye concentration along with the effect of the contact time can be observed from the kinetics of the adsorption performed using different initial concentrations of CR solution at pH of 3, room temperature and adsorbent dosage of 20mg. 50mL⁻¹. The results are shown in Figure.IV.8. The capacity of adsorption increases with increasing time. The rate of adsorption for the first minutes of contact is fast, then it slows down because of the continuous decrease in the concentration (decrease of the driving force) until it reaches gradually the plateau of equilibrium [221]. The equilibrium time was 8, 15, 18 and 22 minutes for the initial dye concentrations of 250, 500, 1000 and 2000 mg.L⁻¹, respectively. The equilibrium time increases with the increase of the initial concentration of the CR solution. In fact, at the beginning of the adsorption, all the active sites were free so a large active surface is available to fix considerable amount of dye molecules, as the adsorption progresses there will be less available active sites which generates a competition between the adsorbate molecules taking longer time to reach the equilibrium. Moreover, the capacity of adsorption increases for increasing initial dye concentration as a result of the increase in the mass gradient and thus the driving force that transfers the dye molecules from bulk solution to the adsorbent surface [222].

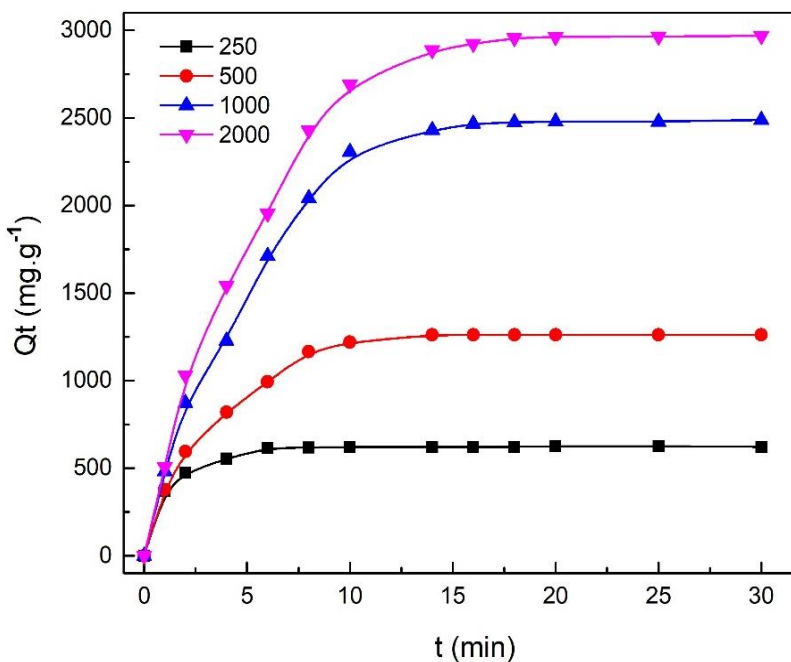


Figure.IV.8. Kinetics of adsorption of CR on ZNa-P at different concentrations

IV.3.2.4 Modeling of the kinetics of CR adsorption on ZNa-P

The adsorption kinetics of CR on ZNa-P was analyzed by the pseudo-first order, the pseudo-second order, Elovich and chemisorption-diffusion equations, using the linear analysis method. The correlation coefficient (R^2) was used to evaluate the applicability of the different kinetic models. Table IV.4 summarizes the results of the kinetic models of the adsorption of CR on ZNa-P. It could be observed that the highest coefficient of correlation is displayed by the pseudo-second-order model (0.95-0.999). The pseudo-first order and Elovich models give R^2 ranging from 0.8-0.95 while the lowest R^2 is given by diffusion-chemisorption model. In addition, the calculated values of the adsorption capacities (Q_{cal}) given by the pseudo-second order are the close to the experimental adsorption capacities (Q_{exp}) comparing to the other models. The linear regression using the pseudo-second order is displayed in Figure.IV.9 where it could be observed that the data points form straight lines. These observations indicate that the adsorption of CR on ZNa-P follows the pseudo-second order kinetic model. Therefore, the results suggest that the pseudo-second-order model is the most suitable model to predict the adsorption behavior of CR on ZNa-P. The same results was obtained for the adsorption of CR on clinoptilolite (natural zeolite) [223].

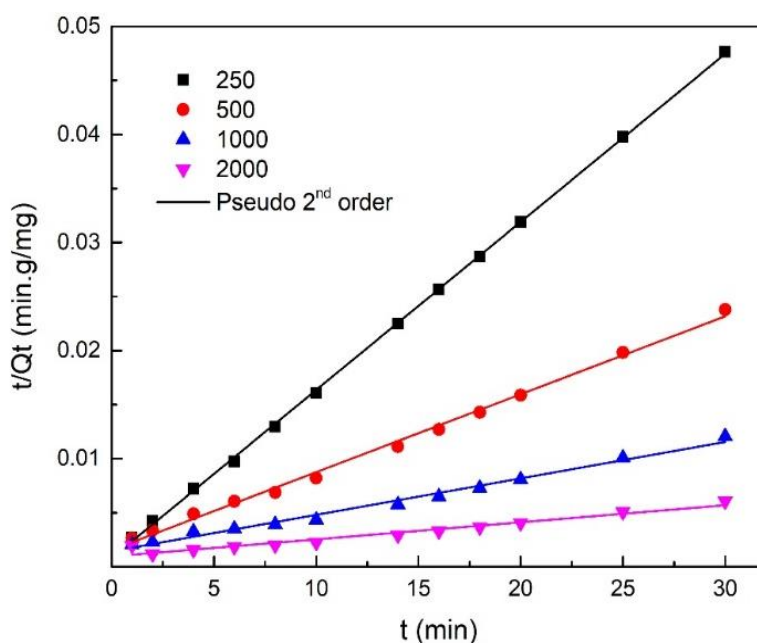


Figure.IV.9. Plots of the pseudo-second-order kinetics of CR on ZNa-P

Table.IV. 4 Comparison of pseudo first order, pseudo second order, Elovich and Diffusion- Chemisorption models for CR adsorption on ZNa-P

C_0 (mg. L ⁻¹)	250	500	1000	2000
Experimental data				
Q_{exp} (mg. g ⁻¹)	629.57	1260.75	2239.96	2967.51
Pseudo-first order model				
k_1 (min ⁻¹)	0.7912	0.2903	0.1951	0.1913
Q_e (mg. g ⁻¹)	657.06	1445.86	3074.86	3678.18
R^2	0.855	0.9521	0.954	0.923
Pseudo-second order model				
k_2 (g. mg ⁻¹ min ⁻¹)	$2.08 \cdot 10^{-3}$	$2.61 \cdot 10^{-4}$	$6.99 \cdot 10^{-5}$	$5.68 \cdot 10^{-5}$
Q_e (mg. g ⁻¹)	620.32	1267.20	2546.84	3036.05
R^2	0.999	0.999	0.999	0.995
Elovich model				
α (mg. g ⁻¹ min ⁻¹)	$3.26 \cdot 10^4$	$1.41 \cdot 10^3$	$1.42 \cdot 10^3$	$1.62 \cdot 10^3$
β (g. mg ⁻¹)	$1.42 \cdot 10^{-2}$	$3.58 \cdot 10^{-3}$	$1.50 \cdot 10^{-3}$	$1.24 \cdot 10^{-3}$
R^2	0.802	0.923	0.942	0.952
Diffusion-Chemisorption Model				
Q_e (mg. g ⁻¹)	591.72	1214.25	2498.79	3911.66
K_{DC} (mg/g. min ^{1/2})	1124.2	574.51	640.49	1183.10
R^2	0.992	0.772	0.021	0.074

IV.3.2.5 Adsorption mechanism of CR on ZNa-P

The kinetics experimental data were also fitted the intraparticle diffusion model. The plot of intraparticle diffusion model expresses the capacity of adsorption Q_t (mg/g) versus square root of time ($t^{0.5}$) where the slope of the linear curve is the diffusion rate (k_i) and the intercept (C) gives information on the thickness of the boundary layer. The intraparticle diffusion model is the most commonly used technique to identify the mechanisms involved in the adsorption process. The plot of the amount adsorbed as a function of $t^{0.5}$, the curve is linear if the adsorption process is only controlled by intraparticle diffusion. However, if the Q_t vs $t^{0.5}$ exhibits multi-linearity, then, two or more steps are involved in the adsorption process. The kinetics data fitted to intraparticle diffusion model are shown in Figure.IV.10. The values of k_1 , k_2 and k_3 for the different steps were determined from the slopes of the linear curves and presented in Table.IV.5.

It is obvious that Figure.IV.10 presents a multilinearity that could be divided in two main steps for the lower concentration (250 and 500mg.L⁻¹) and three steps for the higher initial dye concentrations (1000 and 2000 mg.L⁻¹).

The first step describes the instant adsorption phase where the adsorption rate of CR is the highest due to the large specific surface area and low competition between adsorbates molecules.

The intermediate step, for the concentration 1000 and 2000 mg.L⁻¹, is attributed to the slower and gradual diffusion of the dye molecules to the internal surface of the ZNa-P particles.

The last linear portion for the concentrations 250, 500, 1000 and 2000mg. L⁻¹, is the final step that represents the adsorption equilibrium.

According to the results, this model cannot describe the experimental data. The plots, for all initial concentrations, (Figure.IV.10) do not represent straight lines over the entire time range. This multilinearity indicates that the adsorption process involved more than one mechanism in addition to the intraparticle diffusion. Moreover, the lines do not pass through the origin, then the intraparticle diffusion is not the rate controlling step.

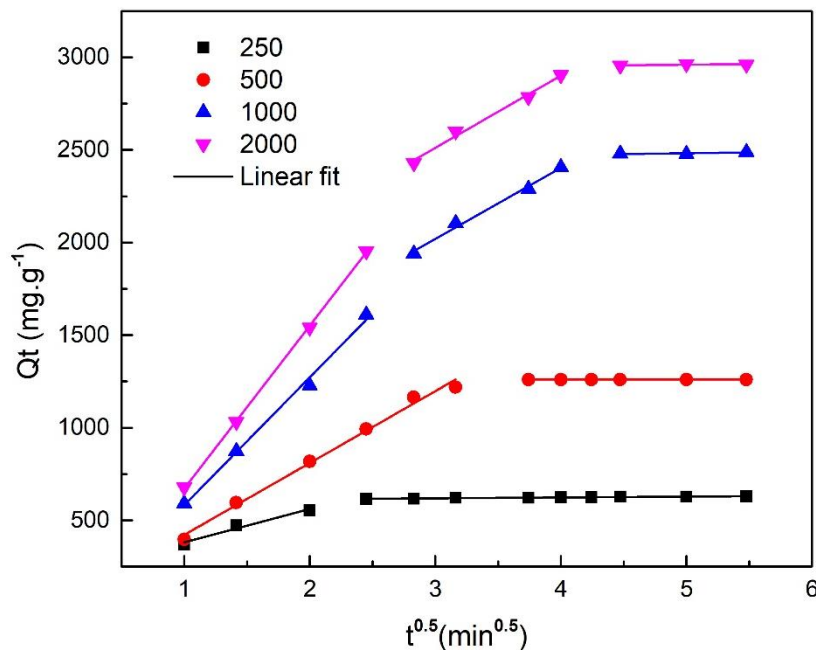


Figure.IV.10. Intraparticle diffusion plots for the adsorption of CR on ZNa-P

Table.IV.5. Intraparticle diffusion model parameters

C_0 (mg.L ⁻¹)	K_{d1} mg g ⁻¹ min ^{-0.5}	R^2	K_{d2} mg g ⁻¹ min ^{-0.5}	R^2	K_{d3} mg g ⁻¹ min ^{-0.5}	R^2
250	180.37	0.945	/	/	4.52	0.952
500	388.1	0.991	/	/	1.19	0.314
1000	690.35	0.999	383.06	0.989	8.62	0.77
2000	879.57	0.999	389.98	0.987	6.67	0.69

IV.3.2.6 Study of the isotherms of adsorption

The investigation of the adsorption isotherms is an important step for the study of adsorption process. In fact, it allows to obtain information on the adsorbent-adsorbate affinity, to understand certain mechanisms related to the adsorption and to determine the maximum capacity of adsorption of the adsorbent. The isotherm of CR adsorption on ZNa-P has been investigated at room temperature of $23 \pm 2^\circ\text{C}$. The results of the isotherm of CR adsorption on ZNa-P is represented in Figure.IV.11.

The amount of adsorbed dye increases with increasing residual concentration until reaching the equilibrium. The form of the adsorption isotherm is of type H according to the classification of Giles et al.[224]. This isotherm indicates that CR has a high affinity for all adsorbent surface, particularly at low concentrations, and represents a system where the dye is strongly attracted to the adsorbent. The maximum capacity of adsorption for CR on ZNa-P was found to be 4672mg.g^{-1} which is a very high capacity of adsorption. to the best of our knowledge it is the highest capacity of adsorption reported for the adsorption of CR.

The isotherm of CR adsorption on ZNa-P was fitted to Langmuir, Freundlich, Sips and Toth models. The results are shown in Figure.IV.11. The parameters of each model were calculated using nonlinear regression and summarized in Table.IV.6. The comparison of R^2 of the different models shows that the Langmuir, Sips and Toth models present high R^2 . The Langmuir and Sips models present R^2 of 0.994, Toth model gives an R^2 of 0.9946 while Freundlich model gives the lowest R^2 of 0.889. the comparison of RMSE of all applied models revealed that Toth model gives the lowest RMSE suggesting that the isotherms data are best fitted with Toth model.

The parameters m in Sips model and t in Toth model characterize the heterogeneity of the adsorption system, the closer are the parameter to the unit the less heterogenous is the system. It is observed from Table.IV.6 that m and t are very close to 1, therefore Sips and Toth could be reduced to Langmuir equation. These results suggest that the adsorption of the CR on ZNa-P occurs on monomolecular layer and on homogenous surface.

The maximum capacity of adsorption given by Langmuir isotherm is 4704 mg.g^{-1} . $1/n$ are less than 1, thereby indicating that the adsorption of CR on ZNa-P is favorable.

Table.IV.6 Langmuir, Freundlich, Sips and Toth parameters for CR adsorption on ZNa-P

Model	parameter	23±1°C
Experimental	$Q_m \text{ (mg. g}^{-1}\text{)}$	4642.27
Langmuir	$Q_m \text{ (mg. g}^{-1}\text{)}$	$4.76 \cdot 10^3$
	$K_L \text{ (L. mg}^{-1}\text{)}$	0.0614
	R_L	0.0160
	R^2	0.994
	RMSE	125.27
Freundlich	$K_F \text{ (L. mg}^{-1}\text{)}$	$1.20 \cdot 10^3$
	$1/n$	0.199
	R^2	0.889
	RMSE	524.91
Sips	$Q_m \text{ (mg. g}^{-1}\text{)}$	$4.73 \cdot 10^3$
	$K_S \text{ (L. mg}^{-m}\text{)}$	0.0524
	m	1.0676
	R^2	0.9941
	RMSE	121.25
Toth	$K_T \text{ (mg. g}^{-1}\text{)}$	$5.9 \cdot 10^3$
	$a_T \text{ (L. mg}^{-1}\text{)}$	19.71
	t	0.969
	R^2	0.9946
	RMSE	115.63

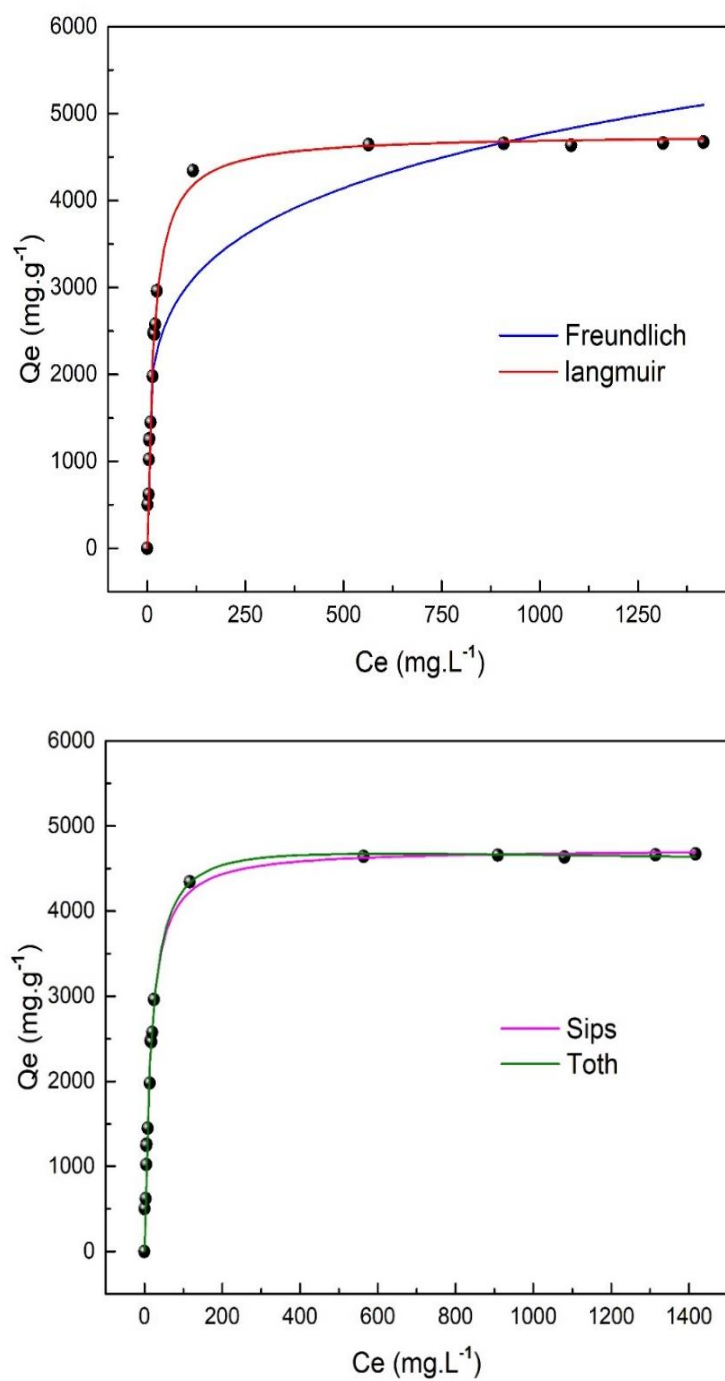


Figure.IV.11. Isotherm of CR adsorption on ZNa-P and its nonlinear regression to Langmuir Freundlich Sips and Toth models

IV.3.2.7 Effect of the temperature and thermodynamic study

To better understand the nature and the mechanism of CR adsorption on ZNa-P surface, the study of the temperature effect was investigated. The results are shown in Figure.IV.12. The study of adsorption at different temperatures allows to determine the different thermodynamic parameters. The thermodynamic parameters were calculated as previously explained in chapter II. The results are presented in Table.IV.7.

The value of ΔG° is negative which indicates that the process is spontaneous. Moreover, we notice a decrease in the values of ΔG° with increasing temperature indicating that the adsorption becomes more favorable at high temperatures. The positive value of ΔS° indicates the increase in the randomness at the solid / liquid interface during the adsorption of CR. The results show that the adsorption process of CR is exothermic.

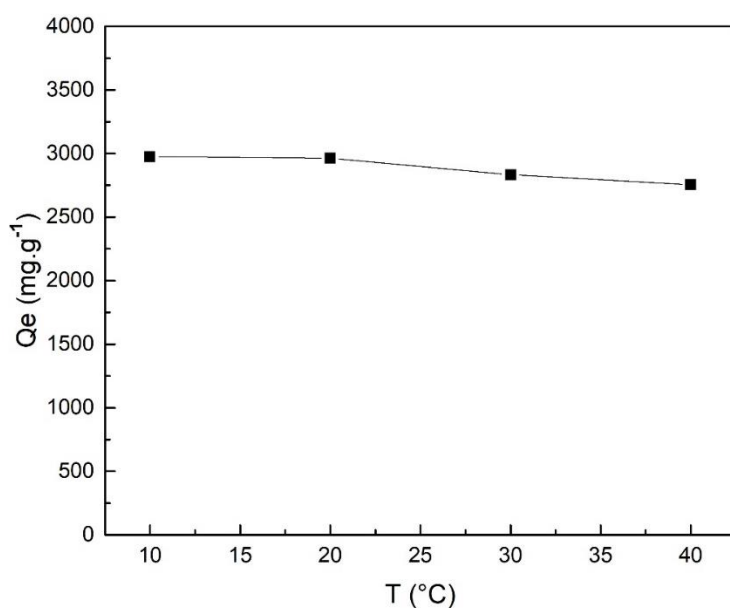


Figure.IV.12. The effect of the temperature of CR adsorption on ZNa-P

Table.IV.7. The thermodynamic parameters of AR66 adsorption onto ZNa-P

ΔH° (kJ/mol)	ΔS° (J/K.mol)	ΔG° (kJ/mol)			
		10°C	20°C	30°C	40°C
-21.14	27.35	-28.89	-29.16	-29.43	-29.71

IV.3.3 Study of the Adsorption of AR66 on ZNa-P using CCD

IV.3.3.1 CCD regression model development

The matrix of the experimental design, based on CCD proposed by the design expert software, along with the results of the response are shown in Table.IV.8. The experimental design consisted of 30 experimental runs with 6 central replicates of the central point where the parameters values corresponded to the zero level (0,0,0,0). As it could be seen from Table.IV.8 the capacity of adsorption (response) varied significantly with the different levels of the factors.

Table.IV.8. Experimental design based on central composite design (CCD) used in this study

Run	X ₁ pH	X ₂ (mg/L)	X ₃ (g/L)	X ₄ (min)	R (mg/g)
1	2.5	600	0.4	15	1746.21
2	3	600	0.4	20	1580.68
3	3	600	0.4	15	1499.55
4	2	200	0.6	25	334.75
5	2	200	0.2	25	995.08
6	4	1000	0.2	5	1540.91
7	2	1000	0.2	5	3034.85
8	3	600	0.4	15	1298.55
9	2	1000	0.6	25	1759.85
10	4	1000	0.2	25	2174.24
11	4	200	0.2	25	943.18
12	3	600	0.4	15	1456.89
13	3	600	0.4	15	1389.36
14	2	1000	0.6	5	1613.26
15	4	200	0.6	5	248.36
16	4	1000	0.6	25	903.03
17	2	1000	0.2	25	3437.88
18	2	200	0.6	5	323.23
19	3	600	0.4	10	1206.52
20	3.5	600	0.4	15	1121.59
21	3	400	0.4	15	977.65
22	3	600	0.3	15	1714.39
23	3	600	0.5	15	1209.39
24	4	200	0.2	5	523.64
25	3	600	0.4	15	1378.03
26	4	1000	0.6	5	474.747
27	3	600	0.4	15	1403.03
28	3	800	0.4	15	1770.45
29	2	200	0.2	5	908.33
30	4	200	0.6	25	336.14

According to the experimental results of the response, obtained by following the proposed design, the quadratic regression was chosen by the RSM to fit the experimental data. The details of the fit summary as well as the Analysis of variance (ANOVA) for the AR66 adsorption onto ZNa-P are represented in Table.A.1 and Table.A.2 in appendix A. The model F-value of 129.95 (Table.A.2) implied that the model was significant. There is only a 0.01% chance that a "Model F-Value" this large could occur due to noise.

The significant regression of the quadratic model was, as well, validated by the insignificant Lack-of-Fit. In fact, the Lack of Fit study (Table.A.2) reported that the quadratic regression presented a Lack of Fit F-value of 2.12 with a p-value of 0.21 which was above the significance threshold (5%). Moreover, the quadratic regression exhibited the highest coefficients of correlation R^2 , adjusted R^2 and predicted R^2 as can be observed in model summary statistics in (Table.A.1). The predicted R^2 of 0.9668 was in reasonable agreement with the adjusted R^2 of 0.9842. It can be noted that the cubic regression also led to high R^2 but the model was not be selected by the fact of being aliased. A desirable adequate precision of 49.68 was obtained indicating that the suggested model can be applied to navigate the design space.

The investigation of ANOVA results allows to establish the quadratic relationship, between the adsorption capacity of AR66 on ZNa-P and the selected variables, expressed by equation IV.2. The factors of the quadratic polynomial are reported in Table.A.1.

$$R = 1417.47 - 337.90 X_1 + 649.85 X_2 - 473.77 X_3 + 145.69 X_4 - 265.18 X_1 X_2 + 70.33 X_1 X_3 + 57.57 X_1 X_4 - 206.83 X_2 X_3 + 62.85 X_2 X_4 - 54.28 X_3 X_4 + 23.37 X_1^2 - 216.03 X_2^2 + 135.33 X_3^2 - 137.83 X_4^2 \quad \text{IV. 2}$$

The diagnostic plots shown in FigureIV.13. present the predicted values versus the actual experimental values. It could be observed that the predicted values were in a good agreement with the experimental data which confirms the adequacy of the obtained model to fit the studied system. The optimization of the experimental variables was performed to maximize the capacity of dye adsorption. the optimum conditions were pH of 2, initial dye concentration of 1000 mg/L, mass of adsorbent of 0.2 g/L and 20 min for the contact time. The predicted maximum of the adsorption capacity for these conditions was 3458.12 mg/g.

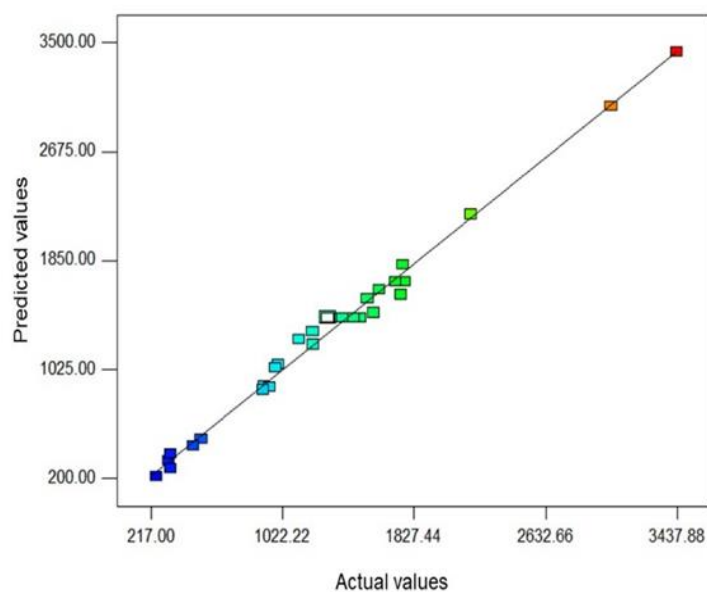


Figure.IV.13. Diagnostic plot of the predicted values versus actual values

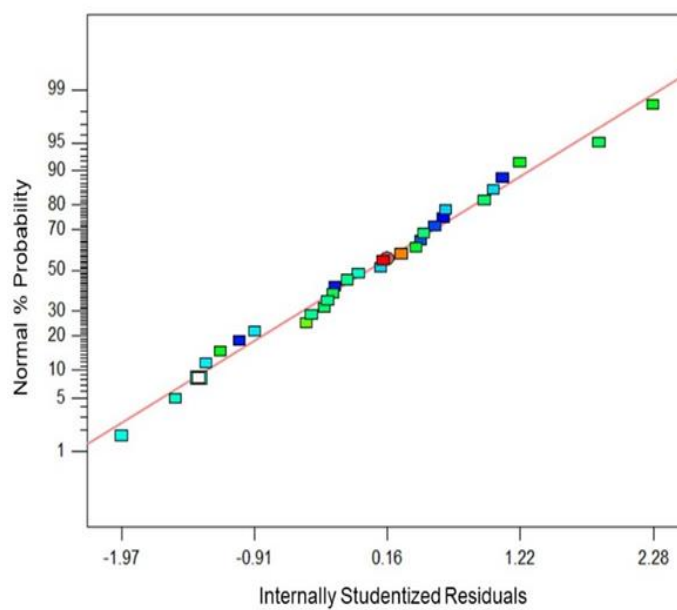


Figure.IV.14. Normal probability plots of the residuals

The effects of the different variables on the capacity of dye adsorption on ZNa-P are displayed in 2D contours as well in 3D response surface plots provided by the design software. The 2D response surface plots for AR66 removal on ZNa-P are represented in Figure.IV.15.

Since the studied system has more than two parameters, two of the variables were varied while the two others were maintained constant at an optimum level.

IV.3.3.2 The effect of the pH

As it is demonstrated in Figure.IV.15. The capacity of adsorption is highly influenced by the pH of the solution. The highest adsorption capacities of AR66 on ZNa-P, represented by the red surfaces, were observed at the lowest pH values. The capacity of adsorption decreased for an increasing pH, reaching the lowest values at higher pH represented by blue area. This can be attributed to the electrostatic forces generated between the ionized dye molecules in the aqueous solution and the nature of the charges gained by the adsorbent surface at the different pH values.

The study of the zeta potential of the ZNa-P should help to better elucidate this phenomenon. The results of the zeta potential analysis are shown in Table.IV.9. According to Table.IV.9, the zeta potential decreased with the increase of pH. Its sign changed from positive to negative for a pH value around pH=5.67 which corresponds to the point of zero charge (pH_{zc}) of the ZNa-P. Therefore, in a solution of pH lower than the pH_{zc} , the ZNa-P surface is positively charged due to its protonation; while at pH higher than the pH_{zc} the surface undergoes a deprotonation and gains a negative charge. The decrease of the zeta potential and consequently the positive charges can adequately explain the decrease of the adsorption capacity of the negatively charged molecules. It is noteworthy that even at a pH value of 4 the adsorption capacities were very high and can exceed 1000 mg/g.

Table.IV.9. Zeta potential of ZNa-P at different pH

pH	Zeta potential
2	20.65
4	15.27
6	-5.71
8	-21.85
10	-21.48

The significant individual effect of the pH parameter was reflected by the high F-value (225) of the parameter pH obtained by ANOVA.

IV.3.3.3 The effect of the initial dye concentration

The Figure.IV.15 illustrates, also, the strong effect of the initial concentration on the AR66 adsorption capacity. The increase in the initial concentration increased the capacity of removing the dye from the aqueous solution which can be explained by the fact that the presence of the ZNa-P in a solution more crowded by dye molecules raises the probability of contact between the dye and the adsorbent which allows to occupy larger active surface by fixing more molecules on the free adsorptive sites [225]. The ANOVA results shows that the initial dye concentration had the most significant influence on the capacity of adsorption with the highest F-value of 832.22.

IV.3.3.4 The effect of the adsorbent mass

In addition, the mass of adsorbent appeared is one of the most influential parameters on the capacity of adsorption with an F-value of 442.34. It is demonstrated by Figure.IV.15. that the use of less mass of adsorbent increases highly the adsorption capacity since this latter is calculated per unit of mass. In other words, the adsorption of a given dye quantity on a larger adsorbent surface (higher adsorbent mass) decreases the capacity of adsorption as long as the use of a lower adsorbent mass may be adequate to remove the same quantity. A dosage of 0.2 g/L is sufficiently powerful and permits to obtain a very high capacity of adsorption which can reach more than 3000 mg/g in given conditions.

IV.3.3.5 The effect of the contact time

The effect of the contact time on the capacity of adsorption can be also observed from the same figure (Figure.IV.15) showing that a higher capacity of adsorption was reached for a larger contact time. For instance, for pH of 3, an adsorbent dosage of 0.2 g/L and an initial concentration of 1000 mg/L, the capacity of adsorption increased from 2270 mg/g for 5 min contact time to 2670 mg/g for 15min contact time. However, comparing to the other factors, the contact time had the least significant effect on the adsorption capacity which is demonstrated by the lowest F-value of 41.83 and the slightly inclined contour curves of the adsorption capacities.

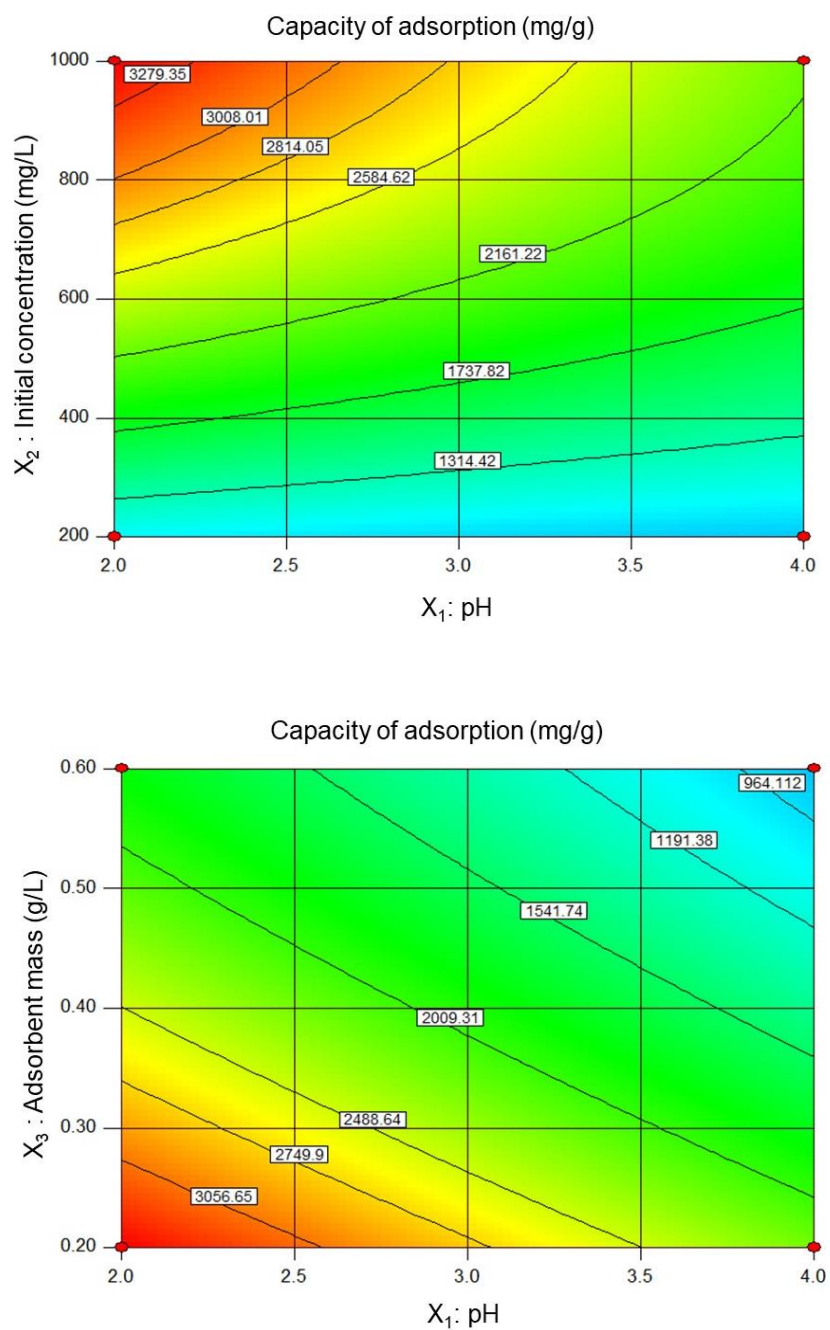


Figure.IV.15. 2D response surface plots for AR66 removal on ZNa-P(a)

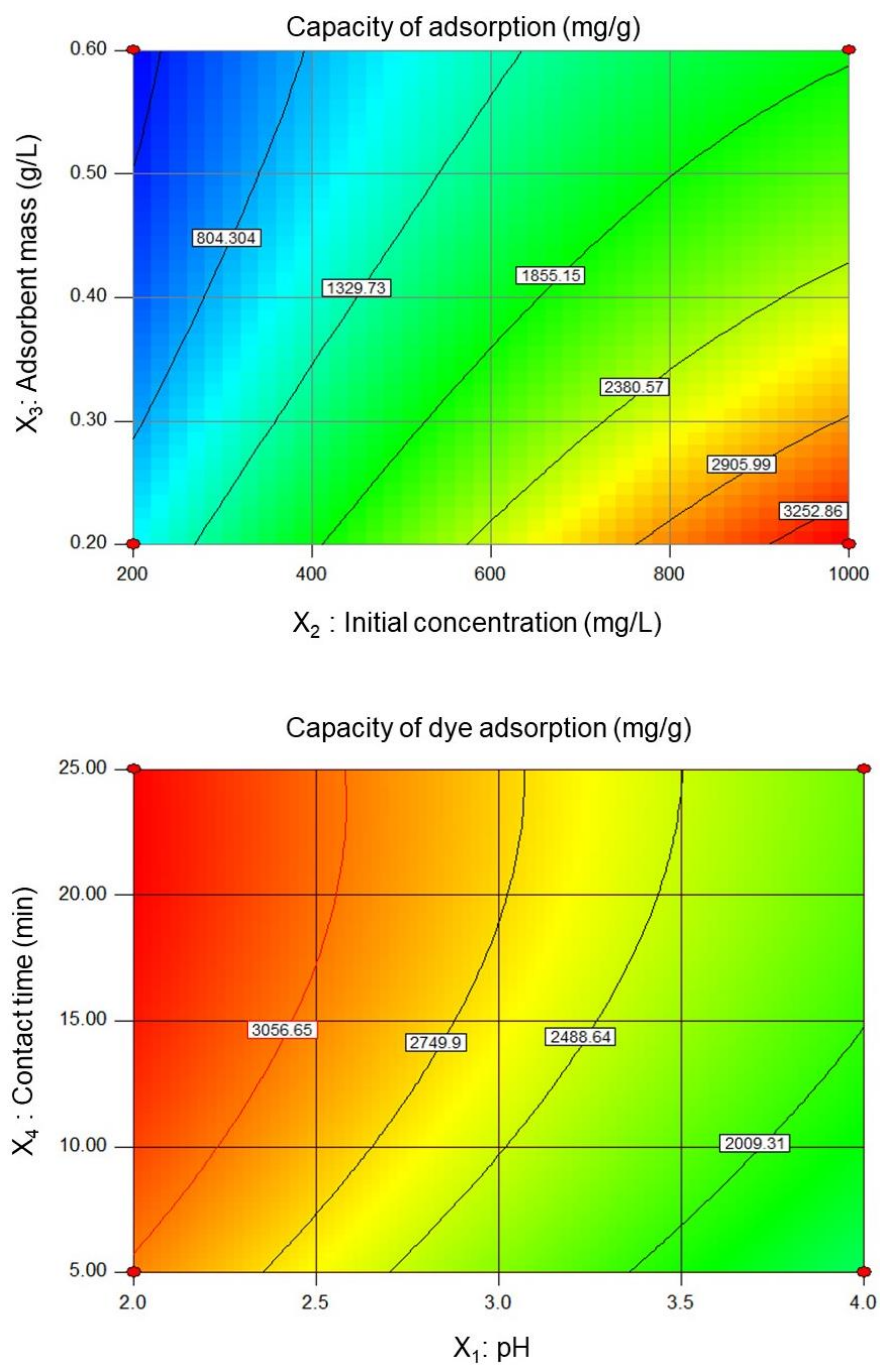


Figure.IV.15. 2D response surface plots for AR66 removal on ZNa-P (b)

IV.3.3.6 Investigation of the interaction effects between the different parameters

In addition to the independent effect of each factor on the capacity of adsorption, the Expert Design software provides a comprehensive study on the nature of the interaction effects between the different factors on the studied response through the ANOVA and the 2D and 3D contour curves.

The ANOVA results reveal that the most significant interactions were generated by the joint effect of the pH and the initial concentration (X_1X_2) with a F-value of 134.38 followed by the joint effect of the initial concentration and the adsorbent dosage (X_2X_3) with a F-value of 81.75. The non-plan surface plots and the presence of curvatures in the 3D surface analysis of the interaction effects prove the significant interaction impacts of X_1X_2 and X_2X_3 on the studied response [226].

The Figure.IV.16. demonstrates the interaction between the pH and the initial concentration at different levels of adsorbent mass and contact time. The increase of the initial concentration with the simultaneous decrease of the pH causes an important increase of the capacity of adsorption of the AR66 on ZNa-P. For instance at fixed levels of mass adsorbent (0.2 g/L) and contact time (25 min) the capacity of adsorption increased from 940 mg/g at pH of 4 and an initial concentration of 200 mg/L to more than 3390 mg/L for a pH of 2 and an initial concentration of 1000 mg/L. In fact, the more active surface -due to the lower pH combined to the high probability of contact between the adsorbent and the adsorbate due to the high initial concentration- accounted for the fast raise in the adsorption capacity of the dye on the ZNa-P surface.

Figure.IV.17 displays the joint effect of the initial concentration and the adsorbent mass at pH =2 and after 25min of contact (Figure.IV.10 (a)) and at pH=4 after 5min of contact time (Figure.IV.10 (b)). The curvatures displayed in Figure.IV.10 reveals the high interaction between the initial concentration and the mass of adsorbent. According to the 3D plots, at a fixed level of pH and contact time, the highest capacities of adsorption were obtained for an initial concentration and a mass of adsorbent close to their 1 and -1 levels, respectively. The increase of the mass of adsorbent and the decrease of the contact time led to a decrease in the capacity of adsorption as it could be seen that the blue color predominates.

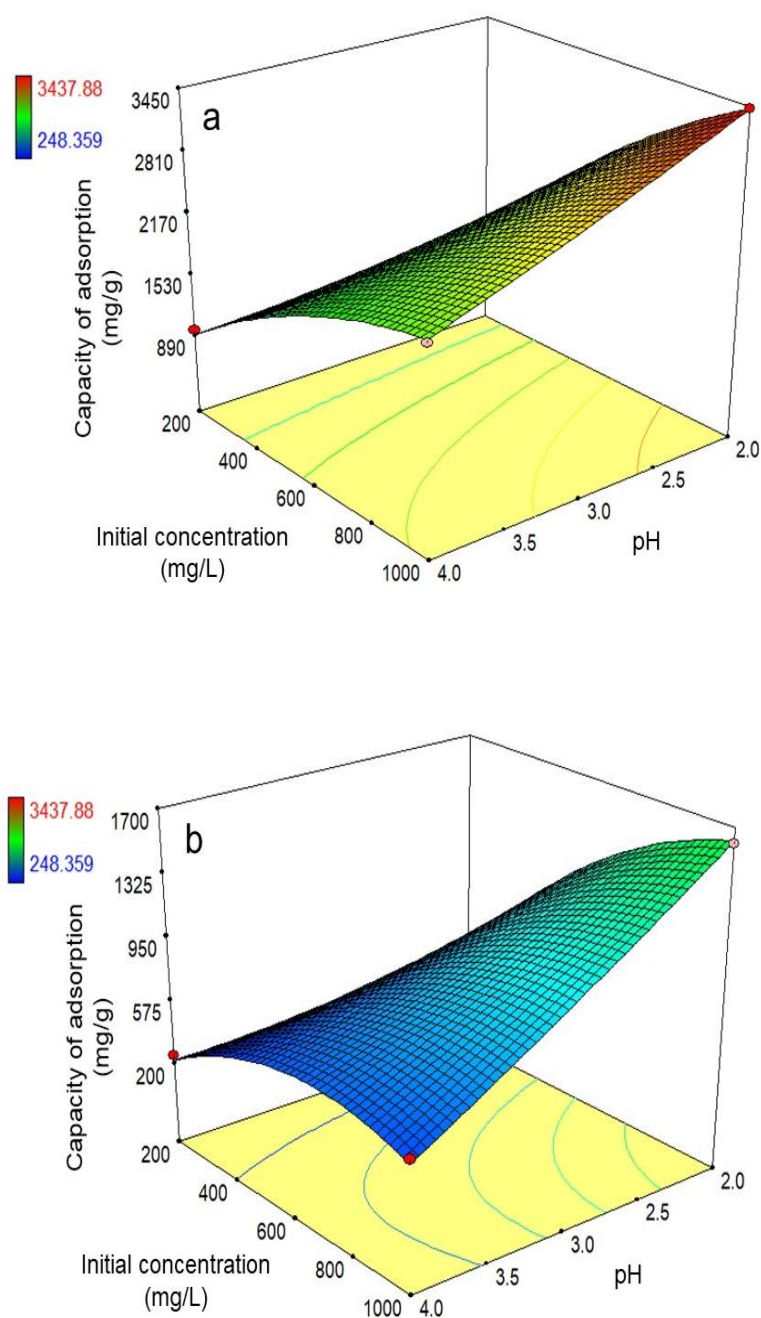


Figure.IV.16. Interaction effect of the pH X_1 and the initial dye concentration X_2 on the capacity of adsorption for (a) $X_3 = 0.2\text{g/L}$ and $X_4 = 25\text{ min}$ (b) $X_3 = 1\text{g/L}$ and $X_4 = 5\text{min}$

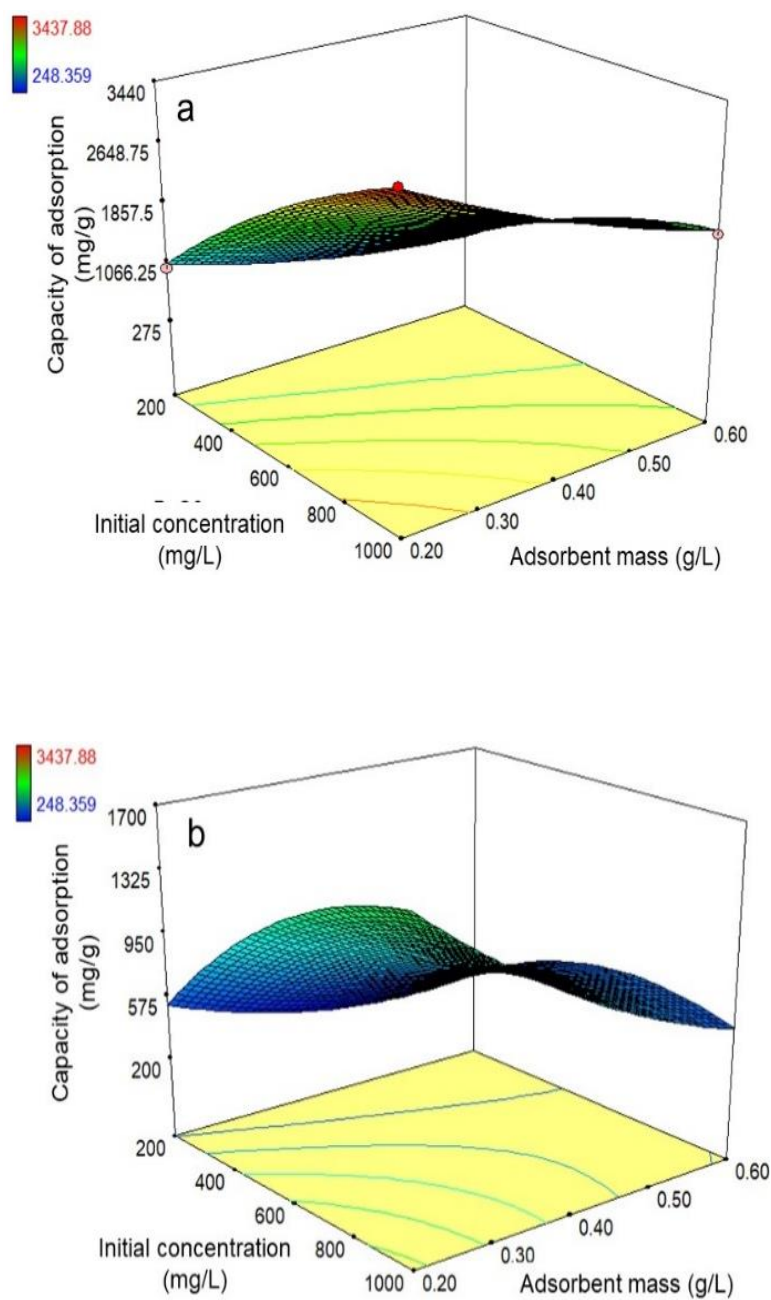


Figure.IV.17. Interaction effect of the initial dye concentration X_2 and the adsorbent mass X_3 on the capacity of adsorption for (a) $X_1=2$ and $X_4=25$ min and (b) $X_1=4$ and $X_4=5$ min

The remaining joint effects of the other quadratic terms (X_1X_3 , X_1X_4 , X_2X_4 , X_3X_4) on the capacity of adsorption were found to be much less significant as indicated by their corresponding F-values which were lower than 10.

The uneven interaction impacts of the pH-mass of adsorbent, pH-contact time, initial concentration-contact time and mass of adsorbent-contact time are displayed in 3D response surface plots represented in Figure.IV.18.

It could be observed that the lowest interaction effects were generated by the terms involving the contact time. It can be seen that the contours were more linear, and the colored section were almost parallel to the contact time axe, confirming the low effect of the contact time on the response. The effect of the contact time was more obvious for high concentrations ($X_2 > 700\text{mg/L}$), where the red contour is larger the more the contact time is higher. For example, for an initial concentration of 1000 mg/L the adsorption capacity was 2670 mg/g after 5 min while it exceeded 3000 mg/g after 25min. It is noteworthy that for lower concentrations, $X_2 < 600\text{mg/L}$, the capacity of adsorption was almost constant over the contact time range. Indeed, at low concentration there is enough space to fix the dye molecules, while at higher concentration a competition for the active sites occurs and hence an increase of the contact time allows to fix more molecules and then increases the adsorption capacity.

The model equation proposed by the design software permits to have a quick view on the independent and the joint effect of the different model terms through the coefficients related to each term. The coefficients accompanied by a positive sign indicate that the corresponding parameters have positive effects on the response, while the parameters associated with negative coefficients are expected to have unfavorable effects on the response. In addition, the numerical value of the coefficients is relative to the influence of the associated term on the response and the results are in good agreement.

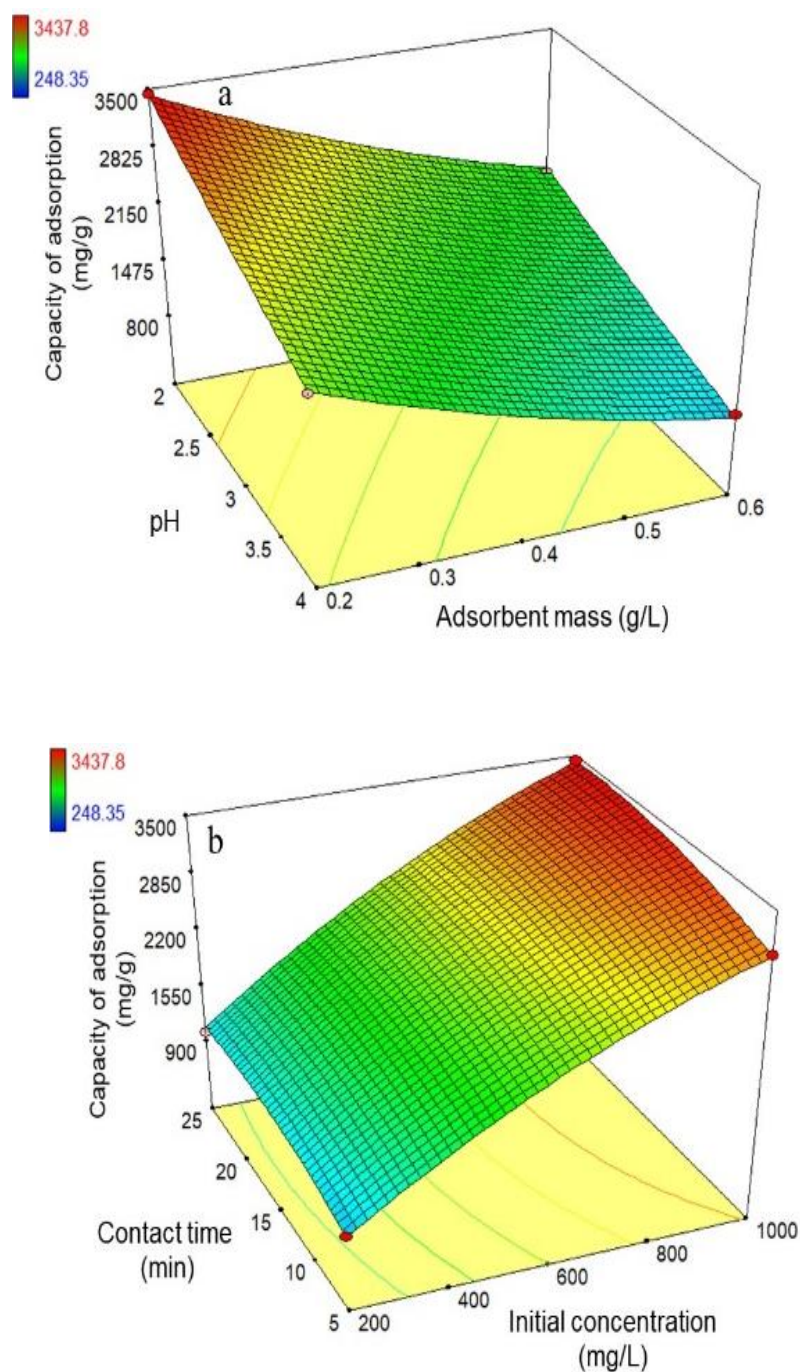


Figure.IV.18 The interaction effect of: (a) pH - adsorbent mass X_1X_3 (b) initial concentration - contact time X_2X_4 (c) pH - contact time X_1X_4 (d) adsorbent mass - contact time X_3X_4

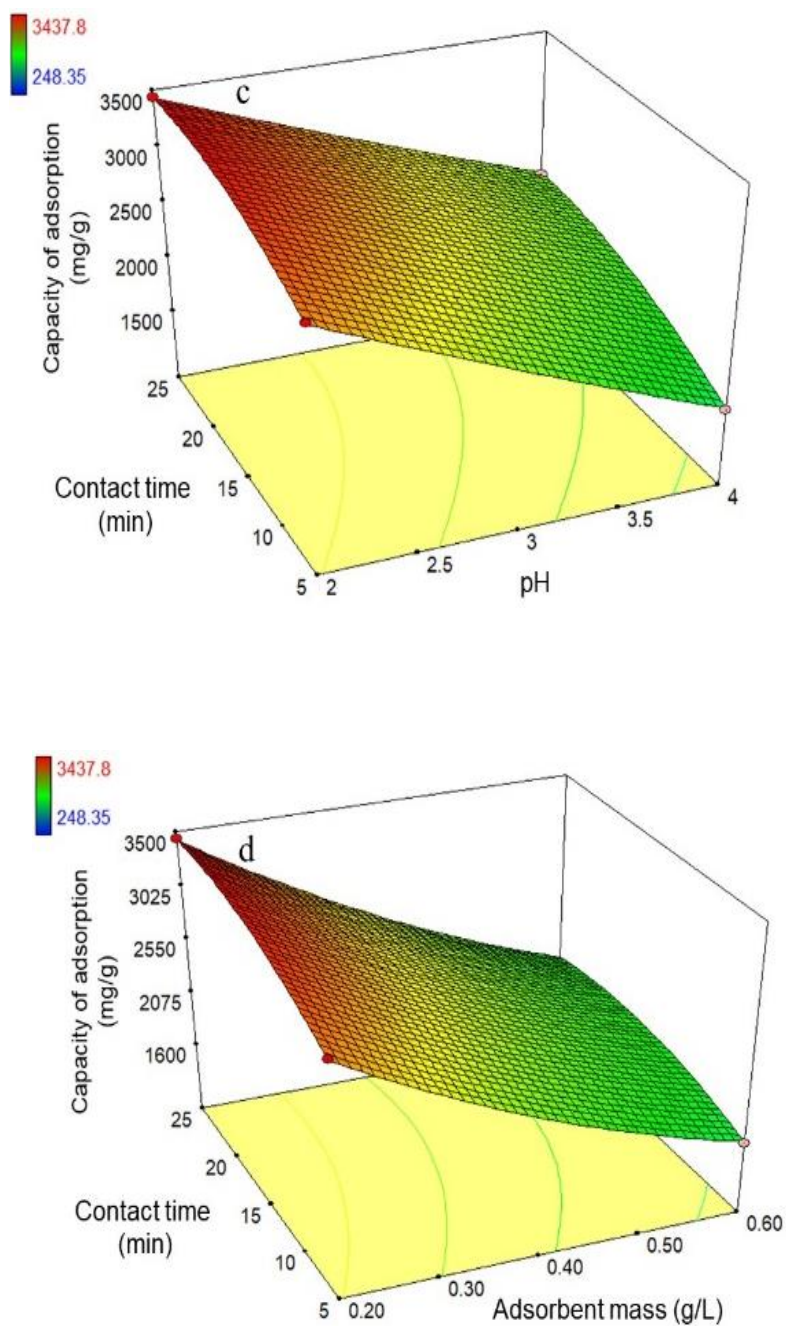


Figure.IV.18. The interaction effect of: (a) pH - adsorbent mass X_1X_3 (b) initial concentration - contact time X_2X_4 (c) pH - contact time X_1X_4 (d) adsorbent mass - contact time X_3X_4

IV.3.3.7 Kinetics of adsorption

The adsorption capacities of the AR66 on ZNa-P as a function of the time, for different initial dye concentrations, are given in Figure.IV.19. According to Figure.IV.19, it appears that the adsorption for the lowest concentrations ($C_0 < 500$ mg/L) was very fast; the equilibrium was promptly reached within the first minutes ($t < 5$ min). For the higher concentrations, more than 85% of the dye was adsorbed in a first phase of adsorption (10-20 min) and then the equilibrium was gradually reached in around 30 minutes for the concentration of 1000 mg/L and 3 hours for 2000 mg/L.

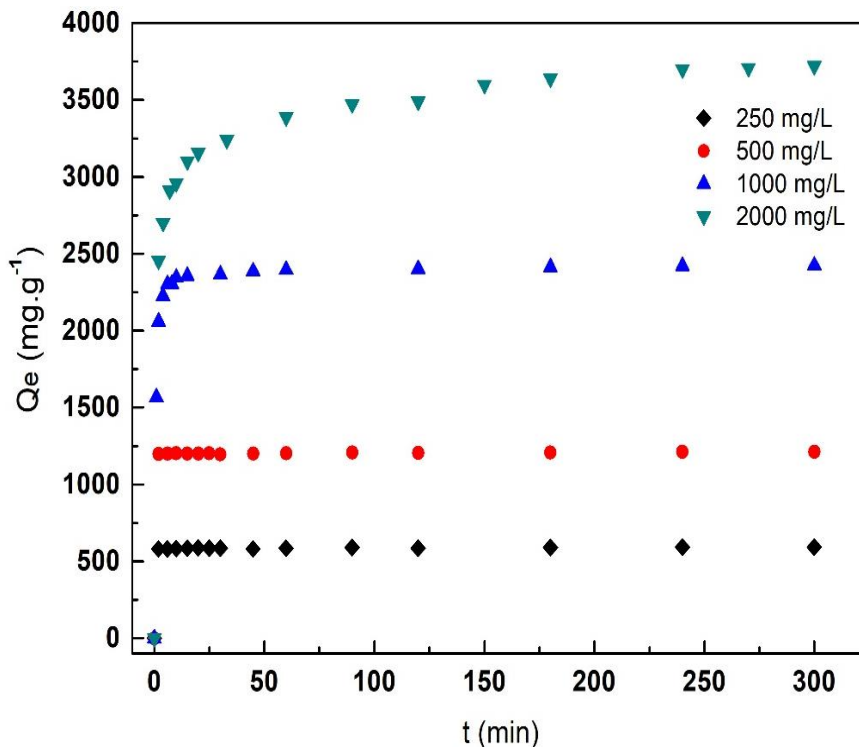


Figure.IV.19. AR66 adsorption kinetics at different initial concentrations

IV.3.3.8 Kinitics modeling

The kinetics of adsorption were fitted to different models: pseudo-first order, pseudo-second order, Elovich and diffusion-chemisorption models. Table.IV. 10 concludes the correlation coefficients and the kinetic constants determined for the different models fitted to the experimental data.

The results show that the values of R^2 given by pseudo first order plots were not very acceptable since they were ranging from 0.12 to 0.92 in addition that the Q_e calculated using this model

which did not agree with the experimental results. These findings show that the adsorption of the dye on the zeolite did not follow a first-order reaction. Elovich model plots obtained by plotting Q_t versus $\ln(t)$ do not give well straight lines in addition to their low R^2 ($R^2=0.287$, 0.495 , 0.726 and 0.98), suggesting that the Elovich model does not describe accurately the adsorption of the dye onto ZNa-P. The same observations were obtained for the plots of the diffusion-chemisorption model which gave R^2 between 0.749 - 0.91 . From Table.IV. 10 it could be observed that the highest R^2 were obtained using the pseudo-second-order model where R^2 are very close to 1. The linear plot of t/Q_t versus t in Figure.IV.20 represents the second model regression of the adsorption kinetics. The plots of the pseudo-second order display well straight lines with a very good agreement between the values of $Q_{e.cal}$ the values of $Q_{e.exp}$ experimentally obtained. Thus, these results show the accuracy of the model to describe the adsorption kinetics of the AR66 on the zeolite.

Table.IV. 10 Comparison of pseudo first order, pseudo second order, Elovich and Diffusion- Chemisorption models for AR66 adsorption on ZNa-P

C_0 (mg. L ⁻¹)	250	500	1000	2000
Experimental data				
Q_{exp} (mg. g ⁻¹)	373.23	756.45	1484.805	2934.51
Pseudo-first order model				
k_1 (min ⁻¹)	0.015	0.011	0.019	0.022
Q_e (mg. g ⁻¹)	13.26	24.08	215.522	1460.40
R^2	0.442	0.3376	0.784	0.822
Pseudo-second order model				
k_2 (g. mg ⁻¹ min ⁻¹)	0.0073	0.0045	$7.59 \cdot 10^{-4}$	$6.94 \cdot 10^{-5}$
Q_e (mg. g ⁻¹)	387,48	804,63	1535,06	3018,02
R^2	1	0.999	1	0.999
Elovich model				
α (mg. g ⁻¹ min ⁻¹)	$6.24 \cdot 10^{18}$	$1.36 \cdot 10^{18}$	$1.10 \cdot 10^{11}$	$5.25 \cdot 10^6$
β (g. mg ⁻¹)	0.7513	0.3641	0.0105	0.0042
R^2	0.2877	0.4957	0.5783	0.9887
Diffusion-Chemisorption Model				
Q_e (mg. g ⁻¹)	403.03	1049.9	2894.7	6194.6
K_{DC} (mg/g. min ^{1/2})	9085.54	23537.11	5632.38	3808.04
R^2	0.749	0.839	0.852	0.913

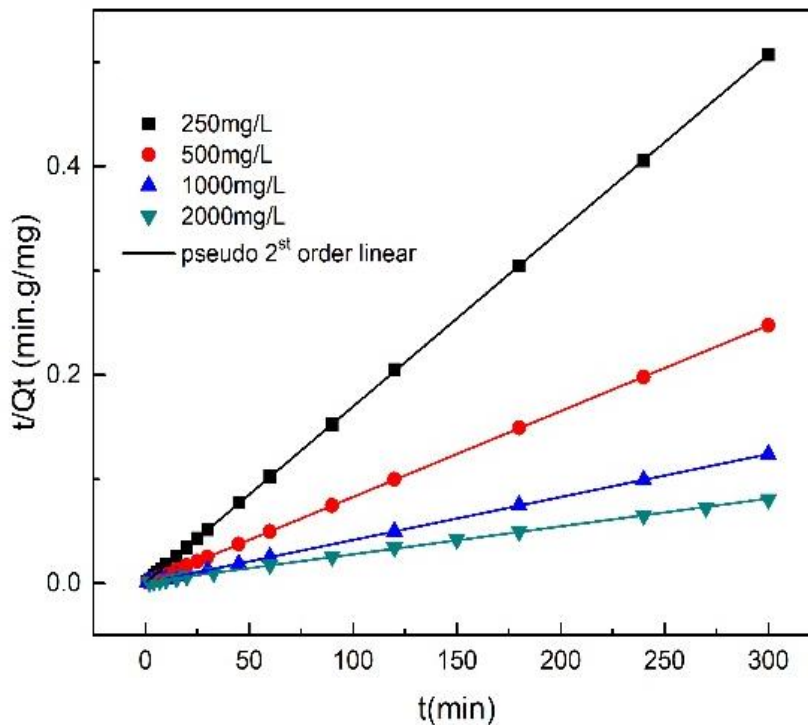


Figure.IV.20. Kinetics of AR66 adsorption onto ZNa-P fitted to the pseudo-second order

IV.3.3.9 Adsorption mechanism of AR66 on ZNa-P

The kinetics were also fitted to the intraparticle diffusion adsorption model and the results are shown in Figure.IV.21. The corresponding parameters, as well as the coefficients of correlation R^2 are summarized in Table.IV.11. Referring to Figure.IV.21, a multilinearity is observed irrespective of the initial dye concentration, implying the involvement of more than one step in the adsorption process [227].

For high concentrations, 1000 mg/L and 2000 mg/L, three straight regions are observed; while for the low concentrations, 250mg/L and 500mg/L, the region could be divided on two main straight regions. The first stage described by the first straight line, was completed within the first three minutes; it can be ascribed to a rapid external mass transfer followed by surface adsorption (film diffusion) where the pollutant is transported to the external surface of the adsorbent [228].

The second step, only observed for the tow highest concentrations, represents a gradual adsorption stage where the intraparticle diffusion can be the rate-limiting step. The third stage corresponds to the final equilibrium step where the intraparticle diffusion begins to slow down

due to the saturation and the lack of active sites. For the lower concentrations, the adsorption process seems to be very fast during the first step and the equilibrium region is rapidly reached because of the low concentration of the remaining dye. This suggests that, for low concentrations, the adsorption mainly occurs in the first step and it can be limited to the external surface adsorption due to the availability of large active surface comparing to the dye quantity in the solution [8][111]. Figure.IV.21 shows that the linear lines for all regions did not pass through the origin indicating that intraparticle diffusion is not the only limiting step in the adsorption process.

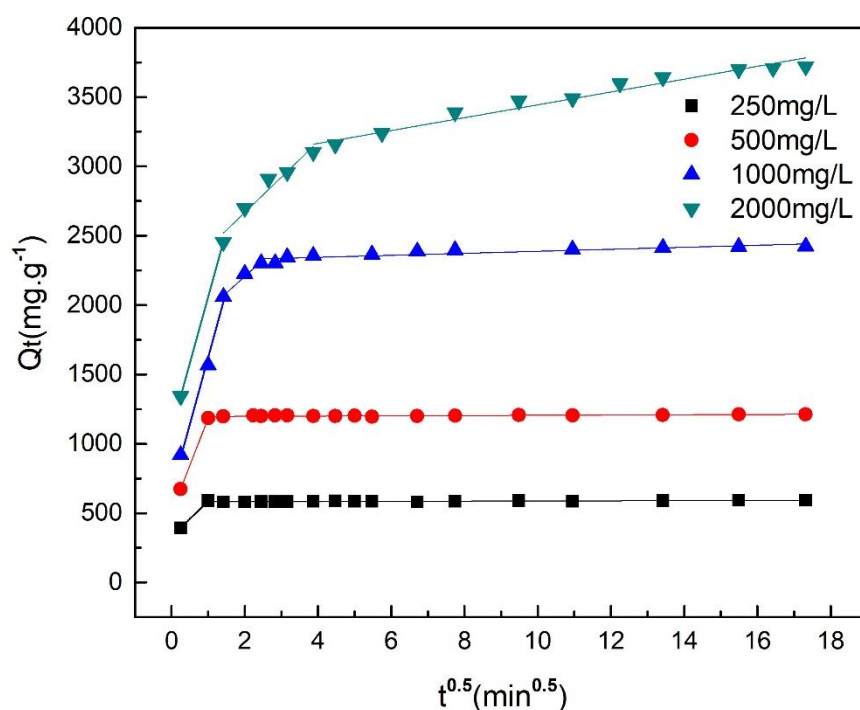


Figure.IV.21. Kinetic simulation by the Intraparticle diffusion model for different initial concentrations

Table.IV.11. Intraparticle diffusion model parameters

Initial dye concentration (mg/L)	Kp_1 $\text{mg g}^{-1} \text{min}^{-0.5}$	R^2	Kp_2 $\text{mg g}^{-1} \text{min}^{-0.5}$	R^2	Kp_3 $\text{mg g}^{-1} \text{min}^{-0.5}$	R^2
250	262.79	1	/	/	0.683	0.717
500	681.11	1	/	/	0.935	0.773
1000	956.2	0.98	238.34	0.96	8.39	0.792
2000	964.85	1	254.61	0.931	43.87	0.957

IV.3.3.10 Isotherms of adsorption

The isotherm of the AR66 onto ZNa-P at room temperature ($\sim 24^{\circ}\text{C}$) is shown in Figure.IV.22. The form of the adsorption isotherm is of type H according to the classification of Giles et al.[224]. This isotherm indicates that AR66 has a high affinity for all adsorbent surface, particularly at low concentrations, and represents a system where the dye is strongly attracted to the adsorbent. It can be observed from Figure.IV.22 that the capacity of adsorption increased with the increase of the dye concentration until reaching an equilibrium represented by a plateau. In fact, the number of dye molecules adsorbed on the adsorbent surface increases with the increase of the solution concentration until it reaches a maximum for which the active sites are completely occupied and the quantity of molecules adsorbed remains the same even if the concentration increases more. This maximum corresponds to the maximum capacity of adsorption. In this study, the maximum capacity of adsorption of AR66 on ZNa-P was estimated at around 3700mg/g.

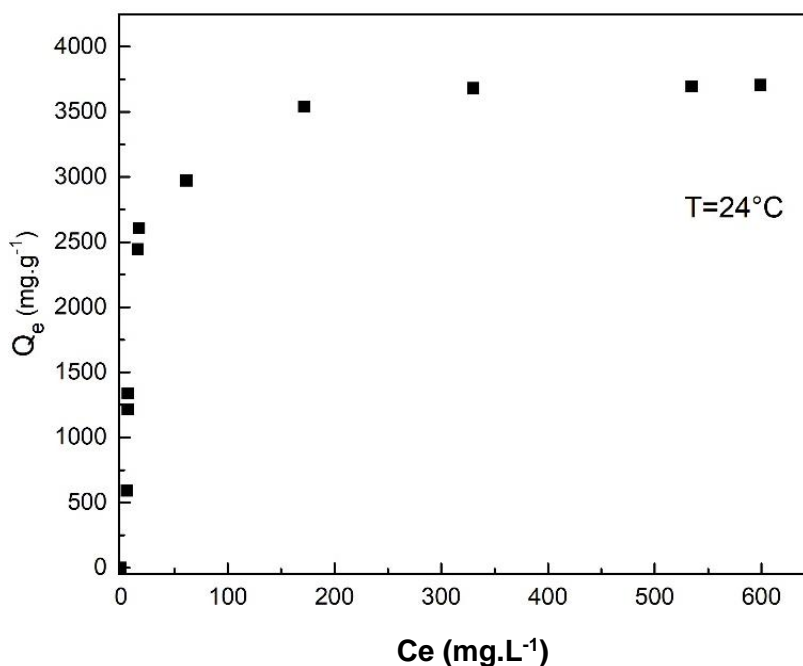


Figure.IV.22. Isotherm of AR66 adsorption onto ZNa-P at room temperature $\sim 24^{\circ}\text{C}$

The isotherm data were fitted to two-parameters models: Langmuir and Freundlich and the plots are represented in Figure.IV.16 (a).

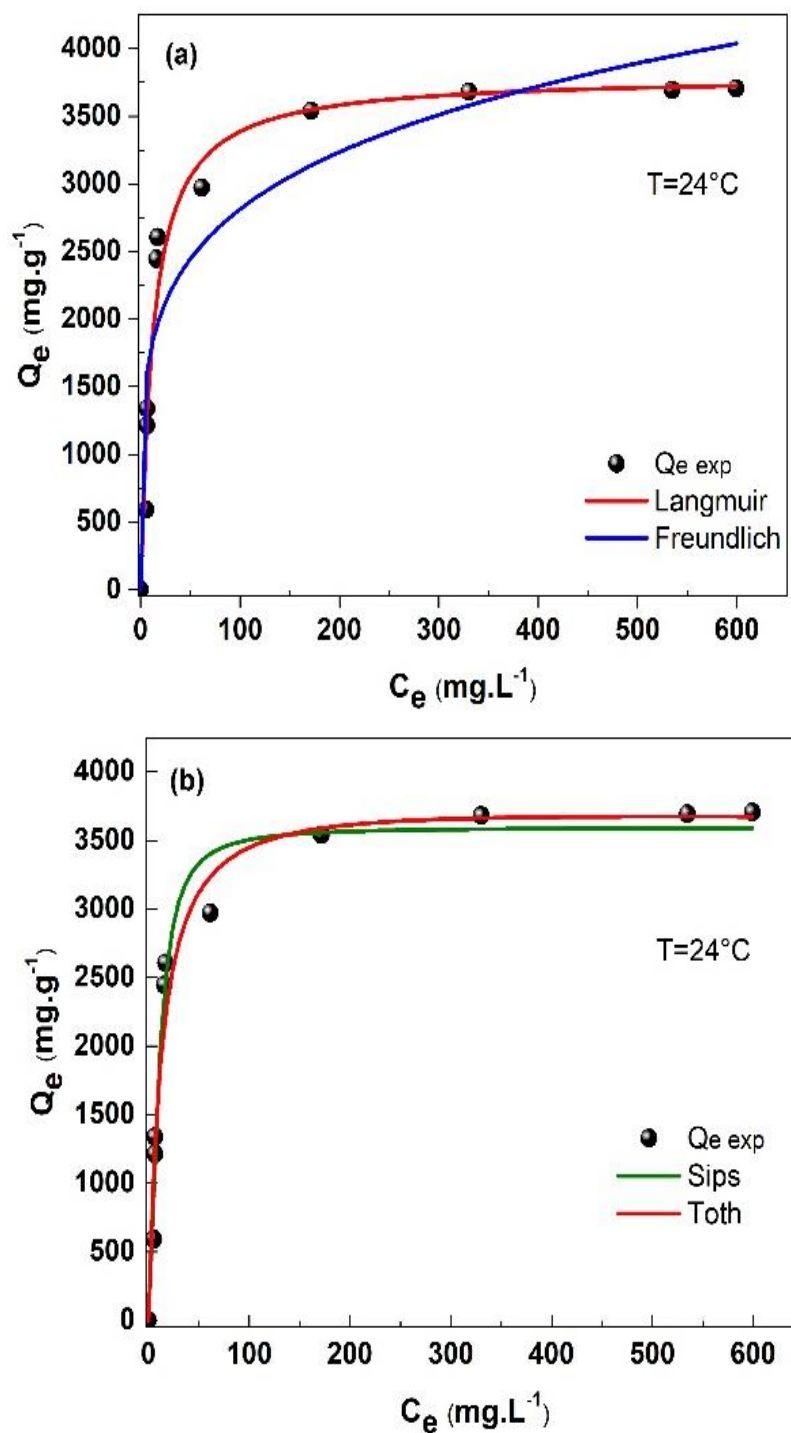


Figure.IV.23. Isotherm data fitted to Langmuir, Freundlich models, Sips and Toth models

The parameters of these models are summarized in Table.IV.12. As observed, the Langmuir model fitted more accurately the experimental data than the Freundlich model with a coefficient of correlation R^2 of 0.957 and $Q_{e \text{ cal}}$ very close to the $Q_{e \text{ exp}}$ suggesting that the adsorption of

AR66 onto ZNa-P is a monolayer adsorption. the R_L dimensionless parameter calculated for the Langmuir model (separation factor) was 0.006, namely in the range of 0-1, indicating a favorable adsorption process [178]

The isotherm data were also fitted to the Sips and Toth three-parameter models. The resulting plots are shown in Figure.IV.16 (b) and the corresponding parameters are summarized in Table.IV.12. It can be clearly observed that both the Sips and Toth models accurately describe experimental isotherm data with high R^2 values, 0.973 and 0.957 respectively. Moreover, this tow models led to the closest Q_e values if compared to the experimental ones. The parameters m in Sips model and t in Toth model characterize the heterogeneity of the adsorption system, the closer are the parameter to the unit the less heterogenous is the system. It is observed from Table.IV.12 that m and t are very close to 1, therefore Sips and Toth the surface of adsorbent is more homogenous. The maximum capacity of adsorption given by Langmuir isotherm is $3801 \text{ mg} \cdot \text{g}^{-1}$. $1/n$ are less than 1, thereby indicating that the adsorption of CR on ZNa-P is favorable. These results suggest that the adsorption of the AR66 on ZNa-P occurs on monomolecular layer and on homogenous surface.

Table.IV.12 Langmuir, Freundlich, Sips and Toth parameters for AR66 adsorption on ZNa-P

Model	parameter	24°C
Experimental	$Q_m (\text{mg} \cdot \text{g}^{-1})$	3707.27
Langmuir	$K_L (\text{L} \cdot \text{mg}^{-1})$	0.082
	$q_m (\text{mg} \cdot \text{g}^{-1})$	3801.3
	R_L	0.006
	R^2	0.957
	RMSE	324.5
Freundlich	$K_F (\text{L} \cdot \text{mg}^{-1})$	1110.3
	n	4.95
	R^2	0.855
	RMSE	623.7
Sips	$K_S (\text{L} \cdot \text{mg}^{-m})$	0.097
	$q_m (\text{mg} \cdot \text{g}^{-1})$	3595.79
	m	1.16
	R^2	0.973
	RMSE	261.2
Toth	$K_T (\text{mg} \cdot \text{g}^{-1})$	3671.82
	$a_T (\text{L} \cdot \text{mg}^{-1})$	14.10
	t	0.974
	R^2	0.957
	RMSE	314.85

IV.3.3.11 Effect of the temperature and thermodynamic study

The temperature is one the most important parameter affecting the adsorption process. The effect of the temperature on the adsorption of AR66 onto ZNa-P is shown in Figure.IV.24. Figure.IV.24 shows slightly a negative effect on the adsorption capacity, since a decrease in the capacity of adsorption from around 3250 mg/g to 2990 mg/g was observed for an increase in the operating temperature from 20°C to 40°C. This indicates that the adsorption of AR66 onto ZNa-P is favorable at low temperatures, indicating an exothermic process.

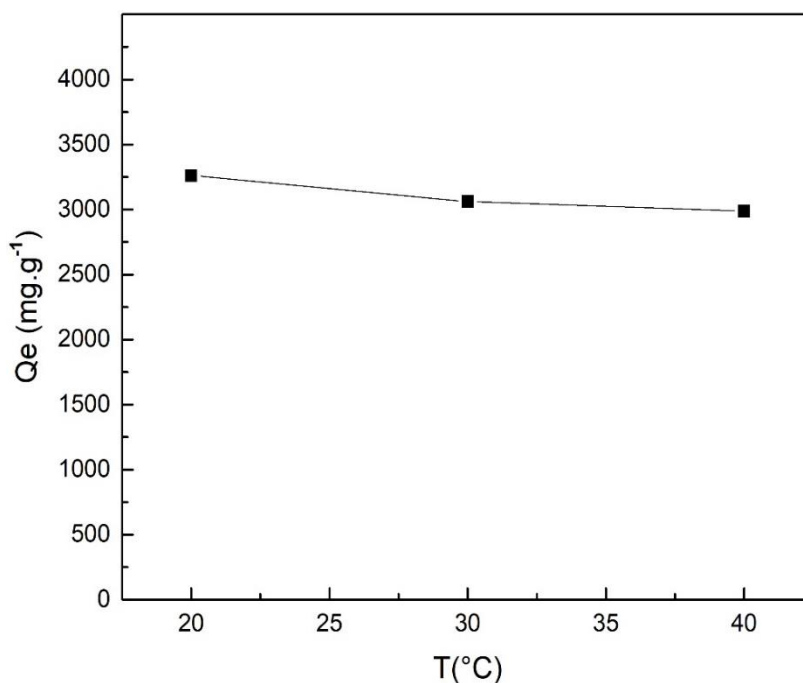


Figure.IV.24. The effect of the temperature on the AR66 adsorption onn the AR66 adsorption onto ZNa-P

The study of the effect of the temperature allows to determine the thermodynamic parameters. The thermodynamic parameters: Gibbs free energy change ΔG° (J/mol) enthalpy ΔH° (J/mol) and entropy ΔS° (J/K. mol) were evaluated and collected in Table.IV.13. The negative value of the enthalpy, -9 kJ/mol, confirmed the exothermic nature of the adsorption of AR66. A positive ΔS° implied a good adsorbent-dye affinity and an increasing randomness at the interface liquid/solid. Moreover, the adsorption process was spontaneous and thermodynamically feasible at all the temperature which was demonstrated by the negative ΔG° .

Similar results were reported for the adsorption of anionic dyes: Reactive Red 239 [229] and Congo Red onto zeolite[230].

Table.IV.13. The thermodynamic parameters of AR66 adsorption onto ZNa-P

ΔH° (kJ/mol)	ΔS° (J/K.mol)	ΔG° (kJ/mol)		
		20°C	30°C	40°C
-9.035	39.47	-14.08	-14.76	-15.44

IV.3.4 Proposed adsorption mechanism of CR and AR66 on ZNa-P

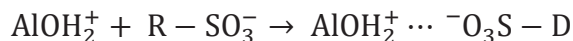
At acidic solution, the CR and AR66 take their anionic forms by being dissociated to polar groups according to the following equation:



Furthermore, at $pH < pH_{zc}$ the Al-OH and Si-OH groups of the ZNa-P are protonated according to the following equation:



Due to the electrostatic attraction between these two counter-ions, the adsorption process occurs as follows:



The FTIR spectra of ZNa-P after the adsorption of CR and AR66 are represented in Figure.IV.25. Some modifications were observed comparing to the ZNa-P spectrum before adsorption. After dye adsorption many functional group bands were moved to different wavenumber. Some bands, such as 3365, 3016, 1737, 1647 and 968 were shifted to lower frequencies while the bands at 586 was shifted to higher frequencies. The peak at 738 was completely disappeared after adsorption.

These changes indicate that there was a possible interaction between the surface of the ZNa-P and the dyes ions.

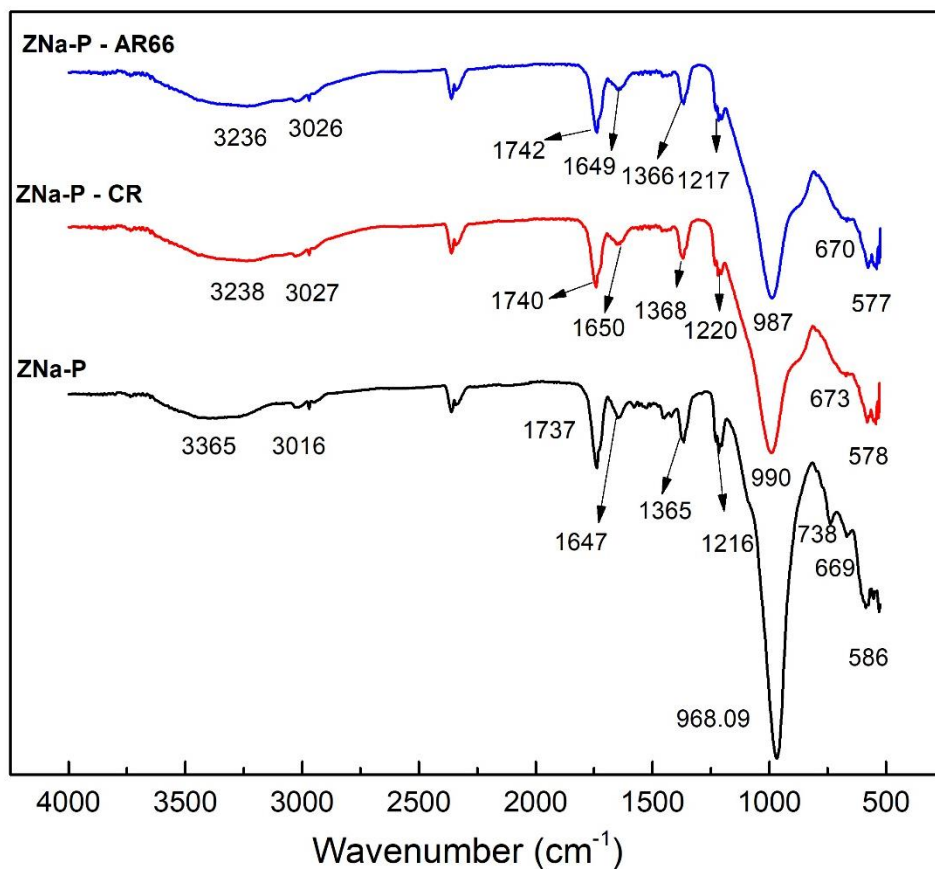


Figure.IV.25. The effect of the temperature on the AR66 adsorption onn the AR66 adsorption onto ZNa-P

IV.3.5 Comparison of adsorption capacity of CR / AR66 on different adsorbents

The adsorption capacities of the studied materials vis-à-vis CR / AR66 were compared to other materials reported in literature and presented in Table.IV.14. It was observed that the materials synthesized in this work represent very high capacities of adsorption especially for the ZNa-P synthesized from CFA using microwave assisted hydrothermal method. The ZNa-P represent the highest capacities of adsorption for both dyes in comparison to the studies reported in literature.

Table.IV.14. The comparison of the adsorption capacities of CR / AR66 on of the studied materials with other materials in literature

Adsorbent	Dye	pH	Initial concentration	$Q_{e \max}$ (mg.g ⁻¹)	Reference
calcium hydroxyapatite	CR	6	150	487.80	[231]
ZnAl-NO ₃	CR	6	1200	571.43	[232]
bentonite/zeolite-NaP	CR	5	20	46.29	[233]
cationic surfactant modified clinoptilolite	CR	5	1000	200	[223]
ZNa-P	CR	3	1000	4760	This study
Acutodesmus obliquus strain	AR66	2	50	44.24	[171]
Fe ₃ O ₄ /natural zeolite	AR66	3	100	317.67	[234]
Calcined Mg–Al–CO ₃	AR66		100	99.9	[13]
Mg-Cu-Al-Fe-CO ₃	AR66	6.8	200	118	This study
Calcined Mg-Cu-Al-Fe-CO ₃	AR66	6.8	500	901	This study
ZNa-P	AR66	3	1000	3707.27	This study

IV.4 Conclusion

In this study the waste CFA was successfully converted into zeolite Na-P applied as adsorbent for the anionic dye AR66 and CR from wastewater. The conversion of CFA into zeolite has been performed through a novel process following three steps. Prior the conversion by microwave assisted method. The CFA has undergone double pre-treatments to enhance the extraction of aluminosilicate from CFA particles. The characterization methods demonstrated that the CFA were successfully transformed into zeolite displaying good characteristics especially a surface area of 378m²/g. The ZNa-P obtained was used to remove the anionic dyes CR and AR66 from aqueous solution. The study of the effect of the different parameters on the adsorption capacity has been studied using conventional method for CR adsorption study. However a CCD was adopted to investigate the adsorption process and to study the effect of four independent variables (pH, Initial dye concentration, adsorbent mass and the contact time) on the capacity of adsorption and the interaction among them through a minimum number of

manipulations and a concise time. According to the results, the capacity of adsorption increased with the increase of the initial dye concentration and the contact time. Nevertheless, the increase in the pH of the solution and the adsorbent dosage impacted negatively the adsorption capacity. The optimum conditions for the adsorption of AR66 on ZNa-P were found to be 2.35 (pH), 1000 mg/g (initial dye concentration), 0.2 g/L (mass of adsorbent) and 18.06 min (contact time). The pseudo-second order was found to fit accurately the kinetics data for both AR66 and CR adsorption. The equilibrium data were well described by the Langmuir model. An extremely high capacities of adsorption was reach in this work which is more that 4760mg/g for CR and 3800 mg/g for AR66. As conclusion, the CFA can be economically converted into an effective adsorbent for anionic dyes removal such as AR66 and Congo Red.

References

- [1] T. Robinson, G. McMullan, R. Marchant, and P. Nigam, "Remediation of dyes in textile effluent: A critical review on current treatment technologies with a proposed alternative," *Bioresour. Technol.*, vol. 77, no. 3, pp. 247–255, 2001.
- [2] C. J. Ogugbue and T. Sawidis, "Bioremediation and Detoxification of Synthetic Wastewater Containing Triarylmethane Dyes by *Aeromonas hydrophila* Isolated from Industrial Effluent," *Biotechnol. Res. Int.*, vol. 2011, pp. 1–11, 2011.
- [3] F. Rafii, J. D. Hall, and C. E. Cerniglia, "Mutagenicity of Azo Dyes Used in Foods , Drugs and Cosmetics Before and After Reduction by *Clostridium* Species from the Human Intestinal Tract," vol. 35, pp. 897–901, 1997.
- [4] E. Mijowska, W. Konicki, D. Moszynski, and E. Mijowska, "Adsorption of anionic azo-dyes from aqueous solutions onto graphene oxide: Equilibrium , kinetic and thermodynamic studies," *J. Colloid Interface Sci.*, vol. 496, pp. 188–200, 2017.
- [5] Y. M. Slokar and A. M. Le Marechal, "Methods of Decoloration of Textile Wastewaters," *Dye. Pigment.*, vol. 37, no. 4, pp. 335–356, 1998.
- [6] M. Abbasi and N. R. Asl, "Sonochemical degradation of Basic Blue 41 dye assisted by nanoTiO₂ and H₂O₂," *J. Hazard. Mater.*, vol. 153, pp. 942–947, 2008.
- [7] E. Errais *et al.*, "Efficient anionic dye adsorption on natural untreated clay : Kinetic study and thermodynamic parameters," *Desalination*, vol. 275, no. 1–3, pp. 74–81, 2011.
- [8] I. Harizi, D. Chebli, A. Bouguettoucha, S. Rohani, and A. Amrane, "A New Mg–Al–Cu–Fe-LDH Composite to Enhance the Adsorption of Acid Red 66 Dye : Characterization , Kinetics and Isotherm Analysis," *Arab. J. Sci. Eng.*, 2018.
- [9] M. Li, L. M. Farmen, and C. K. Chan, "Selenium Removal from Sulfate-Containing Groundwater Using Granular Layered Double Hydroxide Materials," *Ind. Eng. Chem. Res.*, vol. 56, no. 9, pp. 2458–2465, 2017.
- [10] F. P. De Sá, B. N. Cunha, and L. M. Nunes, "Effect of pH on the adsorption of Sunset Yellow FCF food dye into a layered double hydroxide (CaAl-LDH-NO₃)," *Chem. Eng.*

- J.*, vol. 215–216, pp. 122–127, 2013.
- [11] F. Z. Mahjoubi, A. Khalidi, M. Abdennouri, and N. Barka, “Zn–Al layered double hydroxides intercalated with carbonate, nitrate, chloride and sulfate ions: Synthesis, characterization and dyes removal properties,” *J. Taibah Univ. Sci.*, vol. 11, no. 1, pp. 90–100, 2015.
 - [12] S. Tezuka, R. Chitrakar, A. Sonoda, K. Ooi, and T. Tomida, “Studies on selective adsorbents for oxo-anions. NO₃⁻ adsorptive properties of Ni-Fe layered double hydroxide in seawater,” *Adsorption*, vol. 11, no. 1 SUPPL., pp. 751–755, 2005.
 - [13] D. Chebli, A. Bouguettoucha, A. Reffas, C. Tiar, M. Boutahala, H. Gulyas and A. Amrane, “Removal of the anionic dye Biebrich scarlet from water by adsorption to calcined and non-calcined Mg–Al layered double hydroxides,” *Desalin. Water Treat.*, vol. 3994, no. December, pp. 1–13, 2016.
 - [14] K. Shekoohi, F. S. Hosseini, A. H. Haghighi, and A. Sahrayian, “Synthesis of some Mg/Co-Al type nano hydrotalcites and characterization,” *MethodsX*, vol. 4, pp. 86–94, 2017.
 - [15] F. Kovanda, T. Grygar, V. Dorníček, T. Rojka, P. Bezdička, and K. Jiráková, “Thermal behaviour of Cu-Mg-Mn and Ni-Mg-Mn layered double hydroxides and characterization of formed oxides,” *Appl. Clay Sci.*, vol. 28, no. 1–4 SPEC. ISS., pp. 121–136, 2005.
 - [16] Y. Guo, Z. Zhu, Y. Qiu, and J. Zhao, “Adsorption of arsenate on Cu/Mg/Fe/La layered double hydroxide from aqueous solutions,” *J. Hazard. Mater.*, vol. 239–240, pp. 279–288, 2012.
 - [17] K. H. Goh, T. T. Lim, and Z. Dong, “Application of layered double hydroxides for removal of oxyanions: A review,” *Water Res.*, vol. 42, no. 6–7, pp. 1343–1368, 2008.
 - [18] H. Asiabi, Y. Yamini, M. Shamsayei, and E. Tahmasebi, “Highly selective and efficient removal and extraction of heavy metals by layered double hydroxides intercalated with the diphenylamine-4-sulfonate: A comparative study,” *Chem. Eng. J.*, vol. 323, pp. 212–223, 2017.
 - [19] F. L. Theiss, S. J. Couperthwaite, G. A. Ayoko, and R. L. Frost, “A review of the removal

- of anions and oxyanions of the halogen elements from aqueous solution by layered double hydroxides,” *J. Colloid Interface Sci.*, vol. 417, pp. 356–368, 2014.
- [20] I. Akin, G. Arslan, A. Tor, M. Ersoz, and Y. Cengeloglu, “Arsenic (V) removal from underground water by magnetic nanoparticles synthesized from waste red mud,” *J. Hazard. Mater.*, vol. 235–236, pp. 62–68, 2012.
- [21] R. William, R. G. Thiery, R. M. Schuller, and J. J. Subway, “ash : a review of the and proposed classification system with emphasis on environmental impacts,” *Environ. Geol. NOTES*, vol. 96, 1981.
- [22] J. Pizarro, C.Ximena, J. Sebastián, C. Ortizc, N. Patricio, H. Cid, R. Héctor, D. Barros and N. Belzile, “Adsorption of Cu²⁺ on coal fly ash modified with functionalized mesoporous silica,” *Fuel*, vol. 156, pp. 96–102, 2015.
- [23] I. Smirnova, J. Mamic, and W. Arlt, “Adsorption of Drugs on Silica Aerogels,” *Langmuir*, vol. 19, no. 20, pp. 8521–8525, 2013.
- [24] F. Goodarzi, “Characteristics and composition of fly ash from Canadian coal-fired power plants,” *Fuel*, vol. 85, pp. 1418–1427, 2006.
- [25] M. Abbasi and M. M. Habibi, “Optimization and characterization of Direct Blue 71 removal using nanocomposite of Chitosan-MWCNTs: Central composite design modeling,” *J. Taiwan Inst. Chem. Eng.*, vol. 62, pp. 112–121, 2016.
- [26] E. Akceylan, M. Bahadir, and M. Yilmaz, “Removal efficiency of a calix[4]arene-based polymer for water-soluble carcinogenic direct azo dyes and aromatic amines,” *J. Hazard. Mater.*, vol. 162, no. 2–3, pp. 960–966, 2009.
- [27] T. Lean, S. Mohd, J. Noordin, and M. Kassim, “Acidic and Basic Dyes Removal by Adsorption on Chemically Treated Mangrove Barks,” *Int. J. Appl. Sci. Technol.*, vol. 2, no. 3, pp. 270–276, 2012.
- [28] H. Ben Mansour, *Colorants textiles: biodégradation & Toxicité: colorant*. Editions universitaires europeennes, 2012.
- [29] B. D. C. Ventura-camargo and M. A. Marin-morales, “Azo Dyes: Characterization and

- Toxicity– A Review,” *Text. Light Ind. Sci. Technol.*, no. May 2013, 2013.
- [30] A. Welham, “The theory of dyeing (and the secret of life),” *J. Soc. Dye. Colour.*, vol. 116, pp. 140–143, 2000.
- [31] D. R. Waring and G. Hallas, “Classification of Dyes by Chemical Structure,” in *The Chemistry and Application of Dyes*, Springer Science & Business Media, 2013, pp. 17–47.
- [32] K. Hunger *et al.*, “Dye Classes for Principal Applications,” *Industrial Dyes*. pp. 113–338, 09-Dec-2002.
- [33] M. T. Yagub, T. K. Sen, S. Afroze, and H. M. Ang, “Dye and its removal from aqueous solution by adsorption : A review,” *Adv. Colloid Interface Sci.*, vol. 209, pp. 172–184, 2014.
- [34] H. Gao and K. Tastaskan, “Removal of anionic Azo-dyes from aqueous solution,” *J. Hazard. Mater.*, vol. 261, pp. 83–90, 2010.
- [35] Z. Carmen and S. Daniela, “Textile organic dyes—characteristics, polluting effects and separation/elimination procedures from industrial effluents—a critical overview,” in *Organic Pollutants Ten Years After the Stockholm Convention - Environmental and Analytical Update*, 2012.
- [36] C. R. L. D. Souza and P. Peralta-Zamora, “Degradation of reactive dyes by the metallic iron/hydrogen peroxide system,” *Quim. Nova*, vol. 28, no. 2, pp. 226–228, 2005.
- [37] J. C. Greene and G. L. Baughman, “Effects of 46 dyes on population growth of freshwater green alga *Selenastrum capricornutum*,” *Text. Chem. Color.*, vol. 28, no. 4, pp. 23–26, 1996.
- [38] A. E. Clarke and R. Anliker, “Organic dyes and pigments,” in *handbook of environmental chemistry*, Hutzinger, Ed. 1980.
- [39] K. Specht and T. Platzek, “Textile dyes and finishes - Remarks to toxicological and analytical aspects,” *J. Deut. Leb.*, vol. 91, pp. 352–359, 1995.
- [40] K. Golka, S. Kopps, and Z. W. Myslak, “Carcinogenicity of azo colorants: Influence of

- solubility and bioavailability,” *Toxicol. Lett.*, vol. 151, no. 1, pp. 203–210, 2004.
- [41] T. Velpandian, K. Saha, A. K. Ravi, S. S. Kumari, N. R. Biswas, and S. Ghose, “Ocular hazards of the colors used during the festival-of-colors (Holi) in India—Malachite green toxicity,” *J. Hazard. Mater.*, vol. 139, no. 2, pp. 204–208, 2007.
- [42] R. G. Saratale, G. D. Saratale, J. S. Chang, and S. P. Govindwar, “Decolorization and biodegradation of textile dye Navy blue HER by *Trichosporon beigellii* NCIM-3326,” *J. Hazard. Mater.*, vol. 166, no. 2, pp. 1421–1428, 2009.
- [43] M. . gulube.T , Ray Gumbo.J, Masindi.V, “An update on synthetic dyes adsorption onto clay based minerals: A state-of-art review,” *J. Environ. Manage.*, vol. 191, pp. 35–57, 2017.
- [44] V. Katheresan, J. Kansedo, and S. Y. Lau, “Efficiency of various recent wastewater dye removal methods: A review,” *J. Environ. Chem. Eng.*, vol. 6, no. 4, pp. 4676–4697, 2018.
- [45] A. B. dos Santos, F. J. Cervantes, and J. B. van Lier, “Review paper on current technologies for decolourisation of textile wastewaters: Perspectives for anaerobic biotechnology,” *Bioresour. Technol.*, vol. 98, no. 12, pp. 2369–2385, 2007.
- [46] J. Wang *et al.*, “Polyvinylpyrrolidone and polyacrylamide intercalated molybdenum disulfide as adsorbents for enhanced removal of chromium(VI) from aqueous solutions,” *Chem. Eng. J.*, vol. 334, pp. 569–578, 2018.
- [47] G. Limousin, J.-P. Gaudet, L. Charlet, S. Szenknect, V. Barthes, and M. Krimissa, “Sorption isotherms : A review on physical bases , modeling and measurement,” *Appl. Geochemistry*, vol. 22, pp. 249–275, 2007.
- [48] M. N. Rashed, “Adsorption technique for the removal of organic pollutants from water and wastewater,” in *Organic pollutants-monitoring, risk and treatment*, IntechOpen, 2013.
- [49] M. Desjonquères and D. Spanjaard, “Adsorption Phenomena,” in *Concepts in Surface Physics*, Springer, Berlin, Heidelberg, 1996, pp. 17–161.
- [50] S. Verhaverbeke, “Cleaning of Trace Metallic Impurities from Solid Substrates Using

- Liquid Media,” in *Handbook for Cleaning/Decontamination of Surfaces*, Elsevier, 2007, pp. 485–538.
- [51] F. Rouquerol, J. Rouquerol, and K. Sing, “Introduction,” in *Adsorption by Powders and Porous Solids*, 1999, pp. 1–26.
- [52] G. Crini, “Non-conventional low-cost adsorbents for dye removal: A review,” *Bioresour. Technol.*, vol. 97, no. 9, pp. 1061–1085, 2006.
- [53] J. Pérez-Calderón, M. V Santos, and N. Zaritzky, “Reactive RED 195 dye removal using chitosan coacervated particles as bio-sorbent: Analysis of kinetics, equilibrium and adsorption mechanisms,” *J. Environ. Chem. Eng.*, vol. 6, no. 5, pp. 6749–6760, 2018.
- [54] R. Gopinathan, A. Bhowal, and C. Garlapati, “Adsorption Studies of Some Anionic Dyes Adsorbed by Chitosan and New Four-Parameter Adsorption Isotherm Model,” *J. Chem. Eng. Data*, vol. 64, no. 6, pp. 2320–2328, Jun. 2019.
- [55] S. Banerjee, S. Dubey, R. K. Gautam, M. C. Chattopadhyaya, and Y. C. Sharma, “Adsorption characteristics of alumina nanoparticles for the removal of hazardous dye, Orange G from aqueous solutions,” *Arab. J. Chem.*, 2017.
- [56] M. S. Thabet and A. M. Ismaiel, “Sol-Gel γ -Al₂O₃ Nanoparticles Assessment of the Removal of Eosin Yellow Using: Adsorption, Kinetic and Thermodynamic Parameters,” *J. Encapsulation Adsorpt. Sci.*, vol. 6, pp. 70–90, 2016.
- [57] Y.-H. Huang, C.-L. Hsueh, C.-P. Huang, L.-C. Su, and C.-Y. Chen, “Adsorption thermodynamic and kinetic studies of Pb(II) removal from water onto a versatile Al₂O₃-supported iron oxide,” *Sep. Purif. Technol.*, vol. 55, no. 1, pp. 23–29, 2007.
- [58] M. N. Ahmed and R. N. Ram, “Removal of basic dye from waste-water using silica as adsorbent,” *Environ. Pollut.*, vol. 77, no. 1, pp. 79–86, 1992.
- [59] A. Banaei, S. Ebrahimi, H. Vojoudi, S. Karimi, A. Badiei, and E. Pourbasheer, “Adsorption equilibrium and thermodynamics of anionic reactive dyes from aqueous solutions by using a new modified silica gel with 2,2'-(pentane-1,5-diylbis(oxy))dibenzaldehyde,” *Chem. Eng. Res. Des.*, vol. 123, pp. 50–62, 2017.

- [60] N. R. de Mattos, C. R. de Oliveira, L. G. B. Camargo, R. S. R. da Silva, and R. L. Lavall, "Azo dye adsorption on anthracite: A view of thermodynamics, kinetics and cosmotropic effects," *Sep. Purif. Technol.*, vol. 209, pp. 806–814, 2019.
- [61] E. Eren, "Adsorption Performance and Mechanism in Binding of Azo Dye by Raw Bentonite," *Clean Soil Air Water*, vol. 38, pp. 758–763, 2010.
- [62] A. S. Özcan and A. Özcan, "Adsorption of acid dyes from aqueous solutions onto acid-activated bentonite," *J. Colloid Interface Sci.*, vol. 276, no. 1, pp. 39–46, 2004.
- [63] D. Mohan, K. P. Singh, G. Singh, and K. Kumar, "Removal of Dyes from Wastewater Using Flyash , a Low-Cost Adsorbent," *Ind. Eng. Chem. Res.*, vol. 41, no. 15, pp. 3688–3695, 2002.
- [64] S. D. Khattri and M. K. Singh, "Colour Removal from Dye Wastewater Using Sugar Cane Dust as an Adsorbent," *Adsorpt. Sci. Technol.*, vol. 17, no. 4, pp. 269–282, Apr. 1999.
- [65] R. Sivaraj, C. Namasivayam, and K. Kadirvelu, "Orange peel as an adsorbent in the removal of Acid violet 17 (acid dye) from aqueous solutions," *Waste Manag.*, vol. 21, no. 1, pp. 105–110, 2001.
- [66] T. W. Seow and C. K. Lim, "Removal of Dye by Adsorption : A Review," vol. 11, no. 4, pp. 2675–2679, 2016.
- [67] W. Feitknecht and G. Fischer, "Zur Chemie und Morphologie der basischen Salze zweiwertiger Metalle. II. Über basische Kobaltsulfate. (IX. Mitteilung über basische Salze)," *Helv. Chim. Acta*, vol. 18, no. 1, pp. 40–60, 1935.
- [68] J. Wang, A. G. Kalinichev, and R. J. Kirkpatrick, "Molecular modeling of water structure in nano-pores between brucite (001) surfaces," *Geochim. Cosmochim. Acta*, vol. 68, no. 16, pp. 3351–3365, 2004.
- [69] X. Duan and D. G. Evans, *Layered double hydroxides*, vol. 119. Springer Science & Business Media, 2006.
- [70] M. L. Occelli, J. P. Olivier, A. Auroux, M. Kalwei, and H. Eckert, "Basicity and Porosity

- of a Calcined Hydrotalcite-Type Material from Nitrogen Porosimetry and Adsorption Microcalorimetry Methods,” *Chem. Mater.*, vol. 15, no. 22, pp. 4231–4238, Nov. 2003.
- [71] R. Allmann, “The crystal structure of pyroaurite,” *Acta Crystallogr. Sect. B*, vol. 24, no. 7, pp. 972–977, Jul. 1968.
- [72] H. F. W. Taylor, “Crystal structures of some double hydroxide minerals,” *Mineral. Mag.*, vol. 39, no. 304, pp. 377–389, 1973.
- [73] M. Richetta, L. Digiamberardino, A. Mattoccia, P. G. Medaglia, R. Montanari, R. Pizzoferrato, D. Scarpellini, A. Varone, S. Kaciulis, A. Mezzi, P. Soltania, and A. Orsini, “Surface spectroscopy and structural analysis of nanostructured multifunctional (Zn, Al) layered double hydroxides,” *Surf. Interface Anal.*, vol. 48, no. 7, pp. 1–6, 2016.
- [74] N. Benselka-Hadj Abdelkader, A. Bentouami, Z. Derriche, N. Bettahar, and L. C. de Ménorval, “Synthesis and characterization of Mg-Fe layer double hydroxides and its application on adsorption of Orange G from aqueous solution,” *Chem. Eng. J.*, vol. 169, no. 1–3, pp. 231–238, 2011.
- [75] J. He, M. Wei, B. Li, Y. Kang, D. G. Evans, and X. Duan, “Preparation of Layered Double Hydroxides,” *Struct Bond*, vol. 119, no. September 2005, pp. 89–119, 2005.
- [76] W. T. Reichle, “Synthesis of anionic clay minerals (mixed metal hydroxides, hydrotalcite),” *Solid State Ionics*, vol. 22, no. 1, pp. 135–141, 1986.
- [77] F. Cavani, F. Trifiro, and A. Vaccari, “Hydrotalcite-type anionic clays: Preparation, properties and applications,” *Catal. Today*, vol. 11, no. 2, pp. 173–301, 1991.
- [78] S. Miyata, “Anion-Exchange Properties of Hydrotalcite-Like Compounds,” *Clays Clay Miner.*, vol. 31, no. 4, pp. 5–311, 1983.
- [79] A. De Roy, C. Forano, and J. P. Besse, “Layered Double Hydroxides: synthesis and post-synthesis modification,” in *Layered Double Hydroxides: Present and Future*, 2001, pp. 1–39.
- [80] Y. Feng, “Formation et propriétés de matériaux Hydroxydes Doubles Lamellaires bi-intercalés,” *Agrégats Moléculaires et Atomiques*, PhD thesis, Université Blaise Pascal -

- Clermont-Ferrand II, 2006.
- [81] M. Mersellem, “Synthèse et caractérisation des Hydroxydes Double Lamellaire (HDL) et application au transfert de biomolécules,” Magister thesis, Université d’Oran Mohamed BOUDIAF, 2014.
- [82] K. L. Erickson, T. E. Bostrom, and R. L. Frost, “A study of structural memory effects in synthetic hydrotalcites using environmental SEM,” *Mater. Lett.*, vol. 59, no. 2, pp. 226–229, 2005.
- [83] S. Miyata, “The Syntheses of Hydrotalcite-Like Compounds and Their Structures and Physico-Chemical Properties—I: the Systems $\text{Mg}^{2+}\text{-Al}^{3+}\text{-NO}_3^-$, $\text{Mg}^{2+}\text{-Al}^{3+}\text{-Cl}^-$, $\text{Mg}^{2+}\text{-Al}^{3+}\text{-ClO}_4^-$, $\text{Ni}^{2+}\text{-Al}^{3+}\text{-Cl}^-$ and $\text{Zn}^{2+}\text{-Al}^{3+}\text{-Cl}^-$,” *Clays Clay Miner.*, vol. 23, no. 5, pp. 369–375, 1975.
- [84] A. Smalenskaite, A. N. Salak, M. G. S. Ferreira, and A. Kareiva, “Reconstruction peculiarity in co-precipitated Mg/Al and Mg/Al/Ce layered double hydroxides,” in *NanoPortugal international conference*, 2016, pp. 5–6.
- [85] A. Vaccari, “Layered Double Hydroxides: Present and Future,” *Appl. Clay Sci. - APPL CLAY SCI*, vol. 22, pp. 75–76, Jan. 2002.
- [86] H. Morioka *et al.*, “Partial oxidation of methane to synthesis gas over supported Ni catalysts prepared from Ni–Ca/Al-layered double hydroxide,” *Appl. Catal. A Gen.*, vol. 215, no. 1, pp. 11–19, 2001.
- [87] D. Tichit, M. Naciri Bennani, F. Figueras, R. Tessier, and J. Kervennal, “Aldol condensation of acetone over layered double hydroxides of the meixnerite type,” *Appl. Clay Sci.*, vol. 13, no. 5, pp. 401–415, 1998.
- [88] T. Nishimura, N. Kakiuchi, M. Inoue, and S. Uemura, “Palladium(ii)-supported hydrotalcite as a catalyst for selective oxidation of alcohols using molecular oxygen,” *Chem. Commun.*, no. 14, pp. 1245–1246, 2000.
- [89] Y. Zhao, J. He, M. Dai, D. Zhao, X. Wu, and B. Liu, “Emerging CoMn-LDH@MnO₂ electrode materials assembled using nanosheets for flexible and foldable energy storage devices,” *J. Energy Chem.*, 2019.

- [90] C. R. Gardner, "Potential and limitations of drug targeting: An overview," *Biomaterials*, vol. 6, no. 3, pp. 153–160, 1985.
- [91] M. B. A. Rahman, M. Basri, M. Z. Hussein, M. N. H. Idris, R. N. Z. R. A. Rahman, and A. B. Salleh, "Immobilisation of lipase from *Candida rugosa* on layered double hydroxides of Mg/Al and its nanocomposite as biocatalyst for the synthesis of ester," *Catal. Today*, vol. 93–95, pp. 405–410, 2004.
- [92] D. G. Evans and X. Duan, "Preparation of layered double hydroxides and their applications as additives in polymers, as precursors to magnetic materials and in biology and medicine," *Chem. Commun.*, no. 5, pp. 485–496, 2006.
- [93] Y.-J. Lin, D.-Q. Li, D. G. Evans, and X. Duan, "Modulating effect of Mg–Al–CO₃ layered double hydroxides on the thermal stability of PVC resin," *Polym. Degrad. Stab.*, vol. 88, no. 2, pp. 286–293, 2005.
- [94] L. Shi, D. Li, J. Wang, S. Li, D. G. Evans, and X. Duan, "Synthesis, Flame-Retardant and Smoke-Suppressant Properties of a Borate-Intercalated Layered Double Hydroxide," *Clays Clay Miner.*, vol. 53, no. 3, pp. 294–300, 2005.
- [95] B. Ou, J. Wang, Y. Wu, S. Zhao, and Z. Wang, "Efficient removal of Cr (VI) by magnetic and recyclable calcined CoFe-LDH/g-C₃N₄ via the synergy of adsorption and photocatalysis under visible light," *Chem. Eng. J.*, vol. 380, p. 122600, 2020.
- [96] Y. Zheng, B. Cheng, W. You, J. Yu, and W. Ho, "3D hierarchical graphene oxide-NiFe LDH composite with enhanced adsorption affinity to Congo red, methyl orange and Cr(VI) ions," *J. Hazard. Mater.*, vol. 369, pp. 214–225, 2019.
- [97] P. Karthikeyan and S. Meenakshi, "Synthesis and characterization of Zn–Al LDHs/activated carbon composite and its adsorption properties for phosphate and nitrate ions in aqueous medium," *J. Mol. Liq.*, p. 111766, 2019.
- [98] W. Feitknecht and M. Gerber, "Zur Kenntnis der Doppelhydroxyde und basischen Doppelsalze III. Über Magnesium-Aluminiumdoppelhydroxyd," *Helv. Chim. Acta*, vol. 25, pp. 131–137, 1942.
- [99] L. El Gaini, M. Lakraimi, E. Sebbar, A. Meghea, and M. Bakasse, "Removal of indigo

- carmine dye from water to Mg-Al-CO₃-calcined layered double hydroxides,” *J. Hazard. Mater.*, vol. 161, no. 2–3, pp. 627–632, 2009.
- [100] Z. Ni, S. Xia, L. Wang, F. Xing, and G. Pan, “Treatment of methyl orange by calcined layered double hydroxides in aqueous solution: Adsorption property and kinetic studies,” *Colloid Interface Sci.*, vol. 316, pp. 284–291, 2007.
- [101] Y. Guo, Z. Zhu, Y. Qiu, and J. Zhao, “Enhanced adsorption of acid brown 14 dye on calcined Mg/Fe layered double hydroxide with memory effect,” *Chem. Eng. J.*, vol. 219, pp. 69–77, 2013.
- [102] H. Zaghoulane-Boudiaf, M. Boutahala, and L. Arab, “Removal of methyl orange from aqueous solution by uncalcined and calcined MgNiAl layered double hydroxides (LDHs),” *Chem. Eng. J.*, vol. 187, pp. 142–149, 2012.
- [103] R. M. M. dos Santos *et al.*, “Removal of Acid Green 68 : 1 from aqueous solutions by calcined and uncalcined layered double hydroxides,” *Appl. Clay Sci.*, vol. 80–81, pp. 189–195, 2013.
- [104] R. Lafi, K. Charradi, M. A. Djebbi, A. Ben Haj Amara, and A. Hafiane, “Adsorption study of Congo red dye from aqueous solution to Mg-Al-layered double hydroxide,” *Adv. Powder Technol.*, vol. 27, no. 1, pp. 232–237, 2016.
- [105] Y. Lu *et al.*, “High performance NiFe layered double hydroxide for methyl orange dye and Cr(VI) adsorption,” *Chemosphere*, vol. 152, pp. 415–422, 2016.
- [106] B. Li, Y. Zhang, X. Zhou, Z. Liu, Q. Liu, and X. Li, “Different dye removal mechanisms between monodispersed and uniform hexagonal thin plate-like MgAl-CO₃- LDH and its calcined product in efficient removal of Congo red from water,” *J. Alloys Compd.*, vol. 673, pp. 265–271, 2016.
- [107] C. Lei, X. Zhu, B. Zhu, C. Jiang, Y. Le, and J. Yu, “Superb adsorption capacity of hierarchical calcined Ni/Mg/Al layered double hydroxides for Congo red and Cr(VI) ions,” *J. Hazard. Mater.*, vol. 321, pp. 801–811, 2017.
- [108] K. El Hassani, B. H. Beakou, D. Kalnina, E. Oukani, and A. Anouar, “Effect of morphological properties of layered double hydroxides on adsorption of azo dye Methyl

- Orange: A comparative study,” *Appl. Clay Sci.*, vol. 140, pp. 124–131, 2017.
- [109] J. Qu *et al.*, “Synthesis of Li–Al layered double hydroxides via a mechanochemical route,” *Appl. Clay Sci.*, vol. 120, pp. 24–27, 2016.
- [110] D. Bharali and R. C. Deka, “Adsorptive removal of congo red from aqueous solution by sonochemically synthesized NiAl layered double hydroxide,” *J. Environ. Chem. Eng.*, vol. 5, no. 2, pp. 2056–2067, 2017.
- [111] R. Morais *et al.*, “Adsorption of Acid Yellow 42 dye on calcined layered double hydroxide : Effect of time , concentration , pH and temperature,” *Appl. Clay Sci.*, vol. 140, pp. 132–139, 2017.
- [112] C. Tiar, M. Boutahala, A. Benhouria, and H. Zaghoulane-Boudiaf, “Synthesis and physicochemical characterization of ZnMgNiAl-CO₃-layered double hydroxide and evaluation of its sodium dodecylbenzenesulfonate removal efficiency,” *Desalin. Water Treat.*, vol. 57, no. 28, pp. 1–12, 2016.
- [113] D. Bharali and R. C. Deka, “Preferential adsorption of various anionic and cationic dyes from aqueous solution over ternary CuMgAl layered double hydroxide,” *Colloids Surfaces A Physicochem. Eng. Asp.*, vol. 525, no. April, pp. 64–76, 2017.
- [114] C. F. Linares, M. Vásquez, R. Castillo, P. Bretto, R. Solano, and A. Rincón, “Applications of CoMo/calcined quaternary hydrotalcites for hydrotreatment reactions,” *Fuel Process. Technol.*, vol. 132, pp. 105–110, 2015.
- [115] A. F. Cronstedt, “Observation and description of an unknown kind of rock to be named zeolites,” *Kongl Vetenskaps Acad Handl Stock.*, vol. 11, pp. 120–123, 1756.
- [116] A. Dyer, “An Introduction to Zeolite Molecular Sieves,” *Mineral. Mag.*, vol. 53, no. 373, p. 662, 1988.
- [117] D. P. A. Jacobs, E. M. Flanigen, J. C. Jansen, and H. van Bekkum, *Introduction to Zeolite Science and Practice*. Amsterdam: Elsevier, 2001.
- [118] D. C. Baerlocher, L. B. McCusker, and D. H. Olson, *Atlas of Zeolite Framework Types*. Amsterdam: Elsevier, 2007.

- [119] D. W. Breck, "Zeolite Molecular Sieves: Structure, Chemistry," *Anal. Chim. Acta*, vol. 75, 1975.
- [120] S. Zaidi and S. Rohani, "Progress towards a dry process for the synthesis of zeolite - A review," *Rev. Chem. Eng.*, vol. 21, Jan. 2005.
- [121] (IZA-SC), "Zeolite Framework Types," 2017. .
- [122] E. M. Flanigen, "Chapter 2 Zeolites and Molecular Sieves an Historical Perspective," in *Introduction to Zeolite Science and Practice*, vol. 58, H. van Bekkum, E. M. Flanigen, and J. C. B. T.-S. in S. S. and C. Jansen, Eds. Elsevier, 1991, pp. 13–34.
- [123] J. Yu, "Chapter 3: SYNTHESIS OF ZEOLITES," *Stud. Surf. Sci. Catal.*, vol. 168, pp. 39–103, 2007.
- [124] J. D. Sherman, "Synthetic zeolites and other microporous oxide molecular sieves," *Proc. Natl. Acad. Sci. U. S. A.*, vol. 96, no. 7, pp. 3471–3478, Mar. 1999.
- [125] V. R. M. Barrer, "Zeolites and clay minerals as sorbents and molecular sieves.," *Acad. Press. London – New York*, Jan. 1980.
- [126] R. Srivastava, "Synthesis and applications of ordered and disordered mesoporous zeolites: Present and future prospective," *Catal. Today*, vol. 309, pp. 172–188, 2018.
- [127] Z. Xue *et al.*, "Effective removal of Mg^{2+} and Ca^{2+} ions by mesoporous LTA zeolite," *Desalination*, vol. 341, pp. 10–18, May 2014.
- [128] T. Kubota, S. Fukutani, T. Ohta, and Y. Mahara, "Removal of radioactive cesium, strontium, and iodine from natural waters using bentonite, zeolite, and activated carbon," *J. Radioanal. Nucl. Chem.*, vol. 296, May 2012.
- [129] H. Eichorn, "H. Eichorn," *Ann. Phys.*, vol. 105, p. 126, 1858.
- [130] R. B. Benarmas, "Etude de la synthese des nanocristaux de zeolithe de type faujasite et leur modification post-synthese," *phD thesis Univ. d'Oran*, 2014.
- [131] S. V Vassilev and C. G. Vassileva, "Methods for characterization of composition of fly ashes from coal-fired power stations: A critical overview," *Energy and Fuels*, vol. 19, no. 3, pp. 1084–1098, 2005.

- [132] C. Belviso, “State-of-the-art applications of fly ash from coal and biomass: A focus on zeolite synthesis processes and issues,” *Prog. Energy Combust. Sci.*, vol. 65, pp. 109–135, 2018.
- [133] J. C. Hower, “Petrographic examination of coal-combustion fly ash,” *Int. J. Coal Geol.*, vol. 92, pp. 90–97, 2012.
- [134] W. Franus, “Characterization of X-type zeolite prepared from coal fly ash,” *Polish J. Environ. Stud.*, vol. 21, no. 2, pp. 337–343, 2012.
- [135] M. Ahmaruzzaman, “A review on the utilization of fly ash,” *Prog. Energy Combust. Sci.*, vol. 36, no. 3, pp. 327–363, 2010.
- [136] S. B. Wang, S. B. Zhou, G. Huang, B. F. Xiong, S. H. Chen, and X. J. Yi, “Fabrication of 128×128 element optical switch array by micromachining technology,” *Microelectronics J.*, vol. 36, no. 1, pp. 91–95, 2005.
- [137] T. Sakthivel, D. L. Reid, I. Goldstein, L. Hench, and S. Seal, “Hydrophobic High Surface Area Zeolites Derived from Fly Ash for Oil Spill Remediation,” *Environ. Sci. Technol.*, vol. 47, no. 11, pp. 5843–5850, Jun. 2013.
- [138] T. Aldahri, J. Behin, H. Kazemian, and S. Rohani, “Effect of microwave irradiation on crystal growth of zeolitized coal fly ash with different solid/liquid ratios,” *Adv. Powder Technol.*, vol. 28, no. 11, pp. 2865–2874, 2017.
- [139] J. Behin, S. S. Bukhari, V. Dehnavi, H. Kazemian, and S. Rohani, “Using Coal Fly Ash and Wastewater for Microwave Synthesis of LTA Zeolite,” *Chem. Eng. Technol.*, vol. 37, no. 9, pp. 1532–1540, Sep. 2014.
- [140] A. Shoumkova and V. Stoyanova, “Zeolites formation by hydrothermal alkali activation of coal fly ash from thermal power station ‘Maritsa 3’, Bulgaria,” *Fuel*, vol. 103, pp. 533–541, 2013.
- [141] C. Belviso, F. Cavalcante, A. Lettino, and S. Fiore, “Effects of ultrasonic treatment on zeolite synthesized from coal fly ash,” *Ultrason. Sonochem.*, vol. 18, no. 2, pp. 661–668, 2011.

- [142] X. Querol, A. Alastuey, A. López-Soler, and F. Plana, “A Fast Method for Recycling Fly Ash: Microwave-Assisted Zeolite Synthesis,” *Environ. Sci. Technol.*, vol. 31, no. 9, pp. 2527–2533, 1997.
- [143] C. D. Woolard, K. Petrus, and M. Van der Horst, “The use of a modified fly ash as an adsorbent for lead,” *Water SA*, vol. 26, no. 4, pp. 531–536, 2000.
- [144] A. Alastuey, N. Moreno, J.C. Umana, A. Alastuey, E. Hernandez, A. Lopez-Soler and F. Plana, “Synthesis of zeolites from coal fly ash : an overview,” vol. 50, pp. 413–423, 2002.
- [145] X. S. Zhao, G. Q. Lu, and H. Y. Zhu, “Effects of Ageing and Seeding on the Formation of Zeolite Y from Coal Fly Ash,” *J. Porous Mater.*, vol. 4, no. 4, pp. 245–251, 1997.
- [146] S. S. Bukhari, J. Behin, H. Kazemian, and S. Rohani, “Conversion of coal fly ash to zeolite utilizing microwave and ultrasound energies : A review,” *FUEL*, vol. 140, pp. 250–266, 2015.
- [147] T. WAJIMA and K. SUGAWARA, “Material Conversion from Various Incinerated Ashes Using Alkali Fusion Method,” *Int. J. Soc. Mater. Eng. Resour.*, vol. 17, no. 1, pp. 47–52, 2010.
- [148] N. Murayama, H. Yamamoto, and J. Shibata, “Mechanism of zeolite synthesis from coal fly ash by alkali hydrothermal reaction,” 2002.
- [149] D. Wu, B. Zhang, L. Yan, H. Kong, and X. Wang, “Effect of some additives on synthesis of zeolite from coal fly ash,” *Int. J. Miner. Process.*, vol. 80, no. 2, pp. 266–272, 2006.
- [150] Y. P. Chauhan and M. Talib, “A novel and green approach of synthesis and characterization of nano-adsorbents (zeolites) from coal fly ash: A review,” *Sci. Rev. Chem. Commun*, vol. 2, no. 1, pp. 12–19, 2012.
- [151] K. S. Hui, C. Y. H. Chao, and S. C. Kot, “Removal of mixed heavy metal ions in wastewater by zeolite 4A and residual products from recycled coal fly ash,” *J. Hazard. Mater.*, vol. 127, no. 1, pp. 89–101, 2005.
- [152] G. G. Hollman, G. Steenbruggen, and M. Janssen-Jurkovicova, “A two-step process for the synthesis of zeolites from coal fly ash,” *Fuel*, vol. 78, pp. 1225–1230, 1999.

- [153] A. Srinivasan and M. W. Grutzeck, "The Adsorption of SO₂ by Zeolites Synthesized from Fly Ash," *Environ. Sci. Technol.*, vol. 33, no. 9, pp. 1464–1469, May 1999.
- [154] M. Park, C. L. Choi, W. T. Lim, M. C. Kim, J. Choi, and N. H. Heo, "Molten-salt method for the synthesis of zeolitic materials II. Characterization of zeolitic materials," *Microporous Mesoporous Mater.*, vol. 37, no. 1–2, pp. 91–98, 2000.
- [155] X. Querol *et al.*, "Application of zeolitic material synthesised from fly ash to the decontamination of waste water and flue gas," *J. Chem. Technol. Biotechnol.*, vol. 77, no. 3, pp. 292–298, 2002.
- [156] N. Murayama, T. Takahashi, K. Shuku, H. Lee, and J. Shibata, "Effect of reaction temperature on hydrothermal syntheses of potassium type zeolites from coal fly ash," *Int. J. Miner. Process.*, vol. 87, pp. 129–133, 2008.
- [157] X. Querol *et al.*, "Synthesis of zeolites from fly ash at pilot plant scale. Examples of potential applications," *Fuel*, vol. 80, no. 6, pp. 857–865, 2001.
- [158] R. Moriyama, S. Takeda, M. Onozaki, Y. Katayama, K. Shiota, T. Fukuda, H. Sugihara and Y. Tani., "Large-scale synthesis of artificial zeolite from coal fly ash with a small charge of alkaline solution," *Fuel*, vol. 84, no. 12, pp. 1455–1461, 2005.
- [159] M. Inada, H. Tsujimoto, Y. Eguchi, N. Enomoto, and J. Hojo, "Microwave-assisted zeolite synthesis from coal fly ash in hydrothermal process," *Fuel*, vol. 84, pp. 1482–1486, 2005.
- [160] S. Wang and Z. H. Zhu, "Sonochemical treatment of fly ash for dye removal from wastewater," *J. Hazard. Mater.*, vol. 126, no. 1, pp. 91–95, 2005.
- [161] N. Shigemoto, H. Miyaura, and K. Hayashi, "Selective formation of Na-X zeolite from coal fly ash by fusion with sodium hydroxide prior to hydrothermal reaction," *J. Mater. Sci.*, vol. 28, no. 17, pp. 4781–4786, 1993.
- [162] S. S. Bukhari, J. Behin, H. Kazemian, and S. Rohani, "A comparative study using direct hydrothermal and indirect fusion methods to produce zeolites from coal fly ash utilizing single-mode microwave energy," *J. Mater. Sci.*, vol. 49, pp. 8261–8271, 2014.

- [163] T. Lundstedt, R.E. Santelli, E.P. Oliveira, L.S. Villar and L.A. Escaleira, "Experimental design and optimization," *Chemom. Intell. Lab. Syst.*, vol. 42, no. 1, pp. 3–40, 1998.
- [164] M. A. Bezerra, R. E. Santelli, E. P. Oliveira, L. S. Villara, and L. A. Escaleira, "Response surface methodology (RSM) as a tool for optimization in analytical chemistry," *Talanta*, vol. 76, pp. 965–977, 2008.
- [165] G. Hanrahan and K. Lu, "Application of Factorial and Response Surface Methodology in Modern Experimental Design and Optimization," *Crit. Rev. Anal. Chem.*, vol. 36, no. 3–4, pp. 141–151, Dec. 2006.
- [166] G. Sacconi, E. Tanzi, S. Mallozzi, and S. Cavalli, "Determination of niacin in fresh and dry cured pork products by ion chromatography: experimental design approach for the optimisation of nicotinic acid separation," *Food Chem.*, vol. 92, no. 2, pp. 373–379, 2005.
- [167] G. E. P. Box and D. W. Behnken, "Some New Three Level Designs for the Study of Quantitative Variables," *Technometrics*, vol. 2, no. 4, pp. 455–475, 1960.
- [168] S. L. C. Ferreira, R.E. Bruns, H.S. Ferreira, G.D. Matos, J.M. David, G.C. Brandão, E.G.P. da Silva, L.A. Portugal and P.S. dos Reis, "Box-Behnken design: An alternative for the optimization of analytical methods," *Anal. Chim. Acta*, vol. 597, no. 2, pp. 179–186, 2007.
- [169] G. E. P. Box and K. B. Wilson, "On the Experimental Attainment of Optimum Conditions," *J. R. Stat. Soc. Ser. B*, vol. 13, no. 1, pp. 1–38, Jan. 1951.
- [170] D. H. Doehlert, "Uniform Shell Designs," *J. R. Stat. Soc. Ser. C (Applied Stat.)*, vol. 19, no. 3, pp. 231–239, Nov. 1970.
- [171] P. Sarwa, R. Vijayakumar, and S. K. Verma, "Adsorption of Acid Red 66 Dye from Aqueous Solution by Green Microalgae *Acutodesmus obliquus* Strain PSV2 Isolated from an Industrial Polluted Site," *OALib*, vol. 1, no. 3, pp. 1–8, 2014.
- [172] C. Pelekani and V. L. Snoeyink, "A kinetic and equilibrium study of competitive adsorption between atrazine and Congo red dye on activated carbon: the importance of pore size distribution," *Carbon N. Y.*, vol. 39, no. 1, pp. 25–37, 2001.

- [173] S. Lagergren and B. . Svenska, "About the theory of so-called adsorption of soluble substances," *K. Sven. Vetenskapsakademiens Handl.*, vol. 24, no. 4, pp. 1–39, 1898.
- [174] Y.-S. Ho and G. McKay, "The Kinetics of Sorption of Divalent Metal Ions Onto Sphagnum Moss Peat," *Water Res.*, vol. 34, pp. 735–742, 2000.
- [175] S. Roginsky and Y. B. Zeldovich, "The catalytic oxidation of carbon monoxide on manganese dioxide," *Acta Physi chem USSR*, vol. 1, p. 554, 1934.
- [176] OzkanAksakal and HandanUcun, "Equilibrium, kinetic and thermodynamic studies of the biosorption of textile dye (Reactive Red 195) onto *Pinus sylvestris* L," *J. Hazard. Mater.*, vol. 181, no. 1–3, pp. 666–672, 2010.
- [177] C. Sutherland and C. Venkobachar, "A diffusion-chemisorption kinetic model for simulating biosorption using forest macro-fungus, *fomes fasciatus*," *Int. Res. J. Plant Sci.*, vol. 1, no. 4, pp. 107–117, 2010.
- [178] W. J. Weber Jr and J. C. Morris, "Kinetics of adsorption on carbon from solution," *J. Sanit. Eng. Div. Am. Soc. Civ. Eng.*, vol. 89, no. 2, pp. 31–60, 1963.
- [179] I. Langmuir, "THE ADSORPTION OF GASES ON PLANE SURFACES OF GLASS, MICA AND PLATINUM.," *J. Am. Chem. Soc.*, vol. 40, no. 9, pp. 1361–1403, Sep. 1918.
- [180] K. R. Hall, L. C. Eagleton, A. Acrivos, and T. Vermeulen, "Pore- and Solid-Diffusion Kinetics in Fixed-Bed Adsorption under Constant-Pattern Conditions," *Ind. Eng. Chem. Fundam.*, vol. 5, no. 2, pp. 212–223, 1966.
- [181] H. Freundlich, "Über die Adsorption in Lösungen," *Zeitschrift für Phys. Chemie*, vol. 57U, no. 1, pp. 385–470, 1907.
- [182] K. Y. Foo and B. H. Hameed, "Insights into the modeling of adsorption isotherm systems," *Chem. Eng. J.*, vol. 156, pp. 2–10, 2010.
- [183] S. A. Glantz, B. K. Slinker, and T. B. Neilands, *Primer of applied regression and analysis of variance*, vol. 309. McGraw-Hill New York, 1990.
- [184] B. Sengupta, M. S. Bhakhar, and R. Sengupta, "Extraction of copper from ammoniacal solutions into emulsion liquid membranes using LIX 84 I," *Hydrometallurgy*, vol. 89,

- no. 3–4, pp. 311–318, 2007.
- [185] H. Zhang, J. Wang, B. Zhang, Q. Liu, S. Li, H. Yan and L. Liu, “Synthesis of a hydrotalcite-like compound from oil shale ash and its application in uranium removal,” *Colloids Surfaces A Physicochem. Eng. Asp.*, vol. 444, pp. 129–137, 2014.
- [186] L. Li, P. Liu, L. Zhang, and D. Chen, “Photophysical properties of donor–[π]-acceptor azoic chromophores adsorbed and intercalated into MgAlLDH,” *J. Solid State Chem.*, vol. 198, pp. 218–223, 2013.
- [187] G. Eshaq, A. M. Rabie, A. A. Bakr, A. H. Mady, and A. E. ElMetwally, “Cr(VI) adsorption from aqueous solutions onto Mg–Zn–Al LDH and its corresponding oxide,” *Desalin. Water Treat.*, vol. 57, no. 43, pp. 20377–20387, 2016.
- [188] L. Zhang, J. Liu, H. Xiao, D. Liu, Y. Qin, H. Wu, H. Li, N. Du and W. Hou, “Preparation and properties of mixed metal oxides based layered double hydroxide as anode materials for dye-sensitized solar cell,” *Chem. Eng. J.*, vol. 250, no. September 2015, pp. 1–5, 2014.
- [189] M. Purushothaman and G. Pugazhenti, “Utilization of Calcined Ni–Al Layered Double Hydroxide (LDH) as an Adsorbent for Removal of Methyl Orange Dye from Aqueous Solution,” *Environ. Sci. Technol.*, vol. 33, no. 2, pp. 482–489, 2014.
- [190] J. S. Valente, M. Sánchez-Cantú, E. Lima, and F. Figueras, “Method for Large-Scale Production of Multimetallic Layered Double Hydroxides: Formation Mechanism Discernment,” *Chem. Mater.*, vol. 21, no. 24, pp. 5809–5818, 2009.
- [191] X.-J. Wang, X.-P. Zhu, L.-M. Lan, and H.-B. Zuo, “Removal of chromium from laboratory wastewater using preparation–adsorption technology with a Mg/Al/Cr layered compound,” *RSC Adv.*, vol. 6, no. 88, pp. 85595–85602, 2016.
- [192] H. Abdolmohammad-Zadeh, S. Kohansal, and G. H. Sadeghi, “Nickel–aluminum layered double hydroxide as a nanosorbent for selective solid-phase extraction and spectrofluorometric determination of salicylic acid in pharmaceutical and biological samples,” *Talanta*, vol. 84, no. 2, pp. 368–373, 2011.
- [193] O. P. Ferreira, O. L. Alves, D. X. Gouveia, A. G. Souza Filho, J. A. C. De Paiva, and J.

- M. Filho, "Thermal decomposition and structural reconstruction effect on Mg-Fe-based hydrotalcite compounds," *J. Solid State Chem.*, vol. 177, no. 9, pp. 3058–3069, 2004.
- [194] J. Fan, Z. Xu, and S. Zheng, "Comment on 'Factors influencing the removal of fluoride from aqueous solution by calcined Mg-Al-CO₃ layered double hydroxides,'" *J. Hazard. Mater.*, vol. 139, no. 1, pp. 175–177, 2007.
- [195] M. Lakraimi, A. Legrouri, A. Barroug, A. De Roy, and J. Pierre Besse, "Preparation of a new stable hybrid material by chloride–2,4-dichlorophenoxyacetate ion exchange into the zinc–aluminium–chloride layered double hydroxide," *J. Mater. Chem.*, vol. 10, no. 4, pp. 1007–1011, 2000.
- [196] X. Cheng, X. Huang, X. Wang, and D. Sun, "Influence of calcination on the adsorptive removal of phosphate by Zn – Al layered double hydroxides from excess sludge liquor," *J. Hazard. Mater.*, vol. 177, no. 1–3, pp. 516–523, 2010.
- [197] K. S. W. Sing, "Reporting physisorption data for gas/solid systems with special reference to the determination of surface area and porosity (Recommendations 1984)," *Pure Appl. Chem.*, vol. 57, no. 4, pp. 603–619, 1985.
- [198] M. Thommes, K. Kaneko, A.V. Neimark, J.P. Olivier, F. Reinoso, J. Rouquerol and K.C.W. Sing, "Physisorption of gases, with special reference to the evaluation of surface area and pore size distribution (IUPAC Technical Report)," *Pure Appl. Chem.*, vol. 87, no. 9–10, pp. 1051–1069, 2015.
- [199] J. Zhou, S. Yang, J. Yu, and Z. Shu, "Novel hollow microspheres of hierarchical zinc-aluminum layered double hydroxides and their enhanced adsorption capacity for phosphate in water," *J. Hazard. Mater.*, vol. 192, no. 3, pp. 1114–1121, 2011.
- [200] Z. Yu, D. Chen, M. Rønning, T. Vrålstad, E. Ochoa-Fernández, and A. Holmen, "Large-scale synthesis of carbon nanofibers on Ni-Fe-Al hydrotalcite derived catalysts. I. Preparation and characterization of the Ni-Fe-Al hydrotalcites and their derived catalysts," *Appl. Catal. A Gen.*, vol. 338, no. 1–2, pp. 136–146, 2008.
- [201] C. Forano, U. Costantino, V. Prévot, and C. T. Gueho, "Chapter 14.1 - Layered Double Hydroxides (LDH)," in *Handbook of Clay Science*, vol. 5, no. Supplement C, F. Bergaya

- and G. B. T.-D. in C. S. Lagaly, Eds. Elsevier, 2013, pp. 745–782.
- [202] Z. Yan, B. Zhu, J. Yu, and Z. Xu, “Effect of calcination on adsorption performance of Mg–Al layered double hydroxide prepared by a water-in-oil microemulsion method,” *RSC Adv.*, vol. 6, no. 55, pp. 50128–50137, 2016.
- [203] R. Extremera, I. Pavlovic, M. R. Pérez, and C. Barriga, “Removal of acid orange 10 by calcined Mg/Al layered double hydroxides from water and recovery of the adsorbed dye,” *Chem. Eng. J.*, vol. 213, pp. 392–400, 2012.
- [204] I. M. Ahmed and M. S. Gasser, “Adsorption study of anionic reactive dye from aqueous solution to Mg-Fe-CO₃ layered double hydroxide (LDH),” *Appl. Surf. Sci.*, vol. 259, pp. 650–656, 2012.
- [205] H. N. Tran, S. J. You, T. V. Nguyen, and H. P. Chao, “Insight into the adsorption mechanism of cationic dye onto biosorbents derived from agricultural wastes,” *Chem. Eng. Commun.*, vol. 204, no. 9, pp. 1020–1036, 2017.
- [206] J. Wang, C. P. Huang, H. E. Allen, D. K. Cha, and D. Kim, “Adsorption Characteristics of Dye onto Sludge Particulates,” *COLLOID INTERFACE Sci.*, vol. 528, pp. 518–528, 1998.
- [207] G. Alberghina, R. Bianchini, M. Fichera, and S. Fisichella, “Dimerization of Cibacron Blue F3GA and other dyes : influence of salts and temperature,” *Dye. pigments*, vol. 46, pp. 129–137, 2000.
- [208] A. W. M. Ip, J. P. Barford, and G. McKay, “Reactive Black dye adsorption/desorption onto different adsorbents: Effect of salt, surface chemistry, pore size and surface area,” *J. Colloid Interface Sci.*, vol. 337, no. 1, pp. 32–38, 2009.
- [209] M. Alkan, S. Çelikçapa, O. Demirbas, and M. Dog, “Removal of reactive blue 221 and acid blue 62 anionic dyes from aqueous solutions by sepiolite,” *Dye. pigments*, vol. 65, pp. 251–259, 2005.
- [210] C. Lei, M. Pi, P. Kuang, Y. Guo, and F. Zhang, “Organic dye removal from aqueous solutions by hierarchical calcined Ni-Fe layered double hydroxide : Isotherm , kinetic and mechanism studies,” *J. Colloid Interface Sci.*, vol. 496, pp. 158–166, 2017.

- [211] S. I. Pereira, S. F. Aquino, and A. Dias, “Calcined Layered Double Hydroxides for Decolorization of Azo Dye Solutions: Equilibrium, Kinetics, and Recycling Studies 1,” vol. 29, no. 7, 2012.
- [212] T. Aldahri, J. Behin, H. Kazemian, and S. Rohani, “Synthesis of zeolite Na-P from coal fly ash by thermo-sonochemical treatment,” *Fuel*, vol. 182, pp. 494–501, 2016.
- [213] R. Goren, B. Ersoy, C. Ozgur, and T. Alp, “Colloidal stability – slip casting behavior relationship in slurry of mullite synthesized by the USP method,” *Ceram. Int.*, vol. 83, pp. 679–685, 2012.
- [214] E. M. Flanigen, H. Khatami, and H. A. Szymanski, “Molecular Sieve Zeolites Advances in Chemistry Series,” *Am. Chem. Soc. Washington, D.C.*, vol. 101, p. 201, 1971.
- [215] X. Zhang, Q. Guo, Z. Zhang, F. Ling, W. Sun, and R. Li, “Synthesis and characterization of Y/B Ccomposite zeolite and its hydrocracking performance,” in *Nanoporous Materials - Proceedings Of The 5th International Symposium*, Sayari Abdelhamid and J. Mietek, Eds. 2008, pp. 99–108.
- [216] P. Castaldi, L. Santona, C. Cozza, G. Giuliano, C. Abbruzzese, V. Nastro and P. Melis, “Thermal and spectroscopic studies of zeolites exchanged with metal cations,” *J. Mol. Struct.*, vol. 734, no. 1–3, pp. 99–105, 2005.
- [217] T. Al-dahri, A. A. Abdulrazak, I. H. Khalaf, and S. Rohani, “Response surface modeling of the removal of methyl orange dye from its aqueous solution using two types of zeolite synthesized from coal fly ash,” no. June, 2018.
- [218] K. Margeta, N. Zabukovec, M. Siljeg, and A. Farkas, “Natural Zeolites in Water Treatment – How Effective is Their Use,” *Water Treatment.*, Walid Elshorbagy and Rezaul Kabir Chowdhury, IntechOpen, 2013.
- [219] D. Kamel, A. Sihem, C. Halima, and S. Tahar, “Decolourization process of an azoïque dye (Congo red) by photochemical methods in homogeneous medium,” *Desalination*, vol. 247, no. 1–3, pp. 412–422, 2009.
- [220] V. Vimonses, S. Lei, B. Jin, C. W. K. Chow, and C. Saint, “Kinetic study and equilibrium isotherm analysis of Congo Red adsorption by clay materials,” *Chem. Eng. J. J.*, vol. 148,

- pp. 354–364, 2009.
- [221] W. T. Tsai, Y. M. Chang, C. W. Lai, and C. C. Lo, “Adsorption of ethyl violet dye in aqueous solution by regenerated spent bleaching earth,” *J. Colloid Interface Sci.*, vol. 289, no. 2, pp. 333–338, 2005.
- [222] B. Acemioğlu, “Adsorption of Congo red from aqueous solution onto calcium-rich fly ash,” *J. Colloid Interface Sci.*, vol. 274, no. 2, pp. 371–379, 2004.
- [223] R. Nodehi, H. Shayesteh, and A. R. Kelishami, “Enhanced adsorption of congo red using cationic surfactant functionalized zeolite particles,” *Microchem. J.*, 2019.
- [224] C. H. GILES, D. SMITH, and A. HUITSON, “A General Treatment and Classification of the Solute Adsorption Isotherm I. Theoretical,” *J. Colloid Interface Sci.*, vol. 47, no. 3, pp. 755–765, 1974.
- [225] M. Kousha, S. Tavakoli, E. Daneshvar, A. Vazirzadeh, and A. Bhatnagar, “Central composite design optimization of Acid Blue 25 dye biosorption using shrimp shell biomass,” *J. Mol. Liq.*, vol. 207, pp. 266–273, 2015.
- [226] R. Manivasagan and P. Karthic, “Application of Response Surface Methodology for the Extraction of Chromium(VI) by Emulsion Liquid Membrane,” *J. Taiwan Inst. Chem. Eng.*, vol. 41, pp. 105–110, 2010.
- [227] W. H. Cheung, Y. S. Szeto, and G. McKay, “Intraparticle diffusion processes during acid dye adsorption onto chitosan,” *Bioresour. Technol.*, vol. 98, pp. 2897–2904, 2007.
- [228] M. Ozacar, I. A. Sengil, and H. Turkmenler, “Equilibrium and kinetic data , and adsorption mechanism for adsorption of lead onto valonia tannin resin,” *Chem. Eng.*, vol. 143, pp. 32–42, 2008.
- [229] E. Alver and A. ü Metin, “Anionic dye removal from aqueous solutions using modified zeolite: Adsorption kinetics and isotherm studies,” *Chem. Eng. J.*, vol. 200–202, pp. 59–67, 2012.
- [230] I. Harizi, T. Aldahri, D. Chebli, S. Rohani, and A. Bouguettoucha, “Highly Efficient Adsorbent for Anionic Dye using a Synthesized Zeolite P from Coal Fly Ash,” in *ISERD*

142nd international conference, 2018, pp. 1–6.

- [231] M. Chahkandi, “Mechanism of Congo red adsorption on new sol-gel-derived hydroxyapatite nano-particle,” *Mater. Chem. Phys.*, vol. 202, pp. 340–351, 2017.
- [232] S. Chilukoti and T. Thangavel, “Enhanced adsorption of Congo red on microwave synthesized layered Zn-Al double hydroxides and its adsorption behaviour using mixture of dyes from aqueous solution,” *Inorg. Chem. Commun.*, vol. 100, pp. 107–117, 2019.
- [233] M. Shaban, M. R. Abukhadra, M. G. Shahien, and S. S. Ibrahim, “Novel bentonite / zeolite-NaP composite efficiently removes methylene blue and Congo red dyes,” *Environ. Chem. Lett.*, vol. 16, no. 1, pp. 275–280, 2017.
- [234] A. A. Abdulrazak, Z. Mohsin, and S. Rohani, “Optimizing Biebrich Scarlet removal from water by magnetic zeolite 13X using response surface method,” *J. Environ. Chem. Eng.*, vol. 6, no. 5, pp. 6175–6183, 2018.

***General conclusion and
perspectives***

The main objective of this work was to synthesize innovative materials through simple and low-cost methods as well to highlight the potential of the obtained materials in the depollution of wastewater effluents. In order to assess this potential, several experiments (such as material characterization, parameters effects, kinetics and equilibrium experiments) were performed. The experimental results obtained will be summarized in this chapter.

Basically, two main materials have been prepared and used as adsorbent for anionic dye removal from wastewater. The first material chosen was a layered double hydroxide while the second material was a zeolite P.

The layered double hydroxide (LDH) or anionic clay as it is known, has been chosen due to its interesting chemical and physical properties as well as their ease of synthesis. This material shows high efficiencies in attracting different types of anionic pollutants especially azo dyes. Layered double hydroxides based on Bi or tri metal cations are commonly studied. In this work a new layered double hydroxide, based on four metal cations: Cu, Mg, Fe and Al, has been proposed. The LDH used in this work was synthesized by the method of coprecipitation at constant pH. A part of the LDH has been calcined in a programmable furnace under 550°C for 1h. The obtained product was noted as CLDH.

The obtained LDH and CLDH were characterized with several methods: XRD, FTIR, TGA/DTA, BET, SEM, and XRF. Then the capacities of LDH and CLDH to remove AR66 were evaluated by exploring the effect of pH, initial dye concentration, adsorbent mass, time of contact and temperature. Moreover, the mechanism of adsorption was investigated through kinetics and isotherms modeling. The following is summary of the obtained results:

- The XRD was carried out for phase identification of the materials obtained.

The XRD results showed that the layered structure has been successfully formed under the experimental conditions used. This is confirmed by the appearance of the characteristic peaks of the layered double hydroxides at specific angles.

- After calcination the XRD illustrated the destruction of the layered structure where the main characteristic peaks of the LDH have been disappeared.
- The XRF results revealed that the target of obtaining quadri-metal layered double hydroxide was well achieved.

- In the FTIR spectrum, a strong decrease in the intensities of the bands attributed to the carbonate anions is observed after the thermal treatment of Mg-Cu-Al-Fe-CO₃. Also, the absence of peaks characterizing the existence of water molecules has been clearly noticed.
- The BET demonstrated that the calcination has increased the surface area from 48.5m²g⁻¹ for LDH to 69.67 for CLDH.
- TGA/DTA revealed that the loss in weight of the CLDH is much lower compared to LDH.
- Maximum adsorption in monolayer Q_{max} for LDH was 125mg/g while for CLDH it was 920 mg/g. This obtained adsorption capacity made of the calcined Mg-Cu-Al-Fe a competitive adsorbent.
- This improvement in the amount adsorbed dye for CLDH is probably due to the increase of the specific surface area by calcination.
- The thermodynamic study revealed that the adsorption process of AR66 on both LDH and CLDH is endothermic.
- The study of the effect of the different parameters on the adsorption capacity reveals that that the pH of the solution is a primordial parameter that can strongly affect the adsorption process.
- The capacity of adsorption is also affected by the mass adsorbent, contact time and the solution concentration.

This study also involved the use of the coal fly ash waste for the synthesis of valuable materials such as zeolite. The use of waste such as coal fly ash (CFA) is meant to offer an alternative and cheaper mean of producing this unique and functional material. The similarity of composition between the zeolite and CFA made of this later a cheap resource of silica and alumina needed for zeolite synthesis. Furthermore, the potential of the obtained zeolite Na-P (ZNa-P) as a low-cost adsorbent material was assessed for the removal of anionic dye AR66. A preliminary study to evaluate the adsorption capacity of ZNa-P was performed using the anionic dye CR.

CFA waste was collected from an industrial power plant (Ontario, Canada). The conversion of the CFA into zeolite is a very precise process. In fact, every detail in the synthesis process

can significantly affect the result. Succeeding a CFA conversion into zeolite depends mainly on an effective extraction and dissolution of the aluminosilicate contained in the CFA particles in the reaction mixture. The CFA was converted to ZNa-P using microwave assisted hydrothermal method after a pre-treatment of the CFA.

- The XRF analysis results illustrate that the CFA contains SiO_2 and Al_2O_3 as major components which made of it a good choice for zeolite preparation.
- The raw CFA is composed of several phases: quartz, calcite, mullite and hematite. The quartz is the major phase contained in CFA which can be identified by its characteristic XRD peaks at 15.97° , 21.05° and 26.78° .
- The XRD pattern of the CFA after zeolitization shows the disappearance of some peaks as well as a decrease of intensity of others.
- Characteristic peaks of zeolite P appeared at specific angles: $2\theta = 12.68^\circ$, 17.78° , 21.85° , 28.26° and 31.08° confirming the successful zeolitization of the CFA into zeolite P.
- The XRF results show that the exchangeable cations in the prepared zeolite were Na^+ .
- BET results highlight the extremally high ZNa-P surface area of $378 \text{ m}^2 \cdot \text{g}^{-1}$ obtained by the applied process of the synthesis.

The ZNa-P was applied to remove the anionic dyes CR and AR66 from aqueous solution. The study of the CR was performed using the conventional method. The adsorption of AR66 on ZNa-P was investigated using an experimental design provided by Design-Expert 7. The kinetic and equilibrium studies for both dyes were explored by fitting the experimental data to different mathematical models. The use of an experimental design provides us with a rich study of the process using a minimum number of manipulations which reduces time, costs and energy.

- The adsorption of AR66 on ZNa-P could be fitted by a quadratic equation where the coefficients of the equation reflect the individual and the interacted effect of the different parameters.
- The experimental design reveals that the adsorption of AR66 on ZNa-P is mainly depending on pH, initial dye concentration and adsorbent mass.
- The most significant interactions were generated by the joint effect of pH / initial concentration and initial concentration / adsorbent dosage.

- The increase of solution pH affects negatively the capacity of adsorption while this later is positively affected by the increase in the initial concentration. The contact time after the 10 first minutes has a neglectable effect on the adsorption capacity.
- The optimum conditions were found to be 2.35 (pH), 1000 mg/g (initial dye concentration), 0.2 g/L (mass of adsorbent) and 18.06 min (contact time).

The modeling of the experimental data of the adsorption of the AR66 on LDH, CLDH as well as CR and AR66 on ZNa-P illustrated that the pseudo-second order model fits accurately the kinetics data, while the equilibrium experimental data were well described by Langmuir model. Sips and Toth can also describe the isotherms of adsorption of the dyes on the studied materials. Extremely high capacities of adsorption were reached in this work. It was found that the maximum of capacity of adsorption of AR66 on CLDH was $924 \text{ mg} \cdot \text{g}^{-1}$, however it can exceed $3700 \text{ mg} \cdot \text{g}^{-1}$ for the adsorption of the same dye onto ZNa-P and 4760 for CR adsorption on ZNa-P. To the best of our knowledge, and in comparison with the capacities of adsorption reported previously, the maximum capacities of adsorption found in this work using ZNa-P were considered the highest.

The higher capacity of adsorption of AR66 on ZNa-P in comparison with CLDH may be explained by the larger surface area shown by ZNa-P.

Thermodynamics studies reveal that the adsorption process on LDH and CLDH was endothermic while being exothermic in case of adsorption onto ZNa-P.

Both CLDH and ZNa-P can be used as excellent adsorbents for anionic dyes. The comparison of the adsorption process on LDH with ZNa-P shows that each material presents advantages over the other.

In fact, the adsorption using ZNa-P has the following advantages:

- It gives higher capacity of adsorption.
- Faster process where the equilibrium is quickly reached within less than 30 min.
- It offers a valorization of CFA waste which develops positive impact on the environment.

While the use of CLDH has the following advantages:

- Easier synthesis with pre-known composition using pure chemicals.
- The process of adsorption is run in natural pH.

Perspectives

Based on the study presented in this work, a number of recommendations exist for future work:

- Application of LDH and ZNa-P for in cationic dyes removal.
- Investigation of the adsorption of dyes mixture.
- Elaboration of composite materials prepared based on LDH and ZNa-P.
- Adsorbents regeneration.
- Application of continuous adsorption process.

Appendix A

Table.A.1. Fit summary for AR66 adsorption onto ZNa-P

Sequential Model Sum of Squares [Type I]						
Source	Sum of Squares	df	Mean Square	F-value	p-value Prob > F	
Mean vs Total	5.15 10 ⁷	1	5.15 10 ⁷			
Linear vs Mean	1.30 10 ⁷	4	3.25 10 ⁶	32.8955	< 0.0001	
2FI vs Linear	2.05 10 ⁶	6	3.42 10 ⁵	16.2477	< 0.0001	
<u>Quadratic vs 2FI</u>	<u>2.74 10⁵</u>	<u>4</u>	<u>6.86 10⁴</u>	<u>8.1919</u>	<u>0.0010</u>	<u>Suggested</u>
Cubic vs Quadratic	9.38 10 ⁴	8	117. 10 ⁴	2.5794	0.1146	Aliased
Residual	3.18 10 ⁴	7	4.54 10 ³			
Total	6.69 10 ⁷	30	2.25 10 ⁶			
Lack of Fit Tests						
Source	Sum of Squares	df	Mean Square	F-value	p-value Prob > F	
Linear	2.43 10 ⁶	20	1.21 10 ⁵	25.36	0.0010	
2FI	3.76 10 ⁵	14	2.69 10 ⁴	5.61	0.0337	
<u>Quadratic</u>	<u>1.02 10⁵</u>	<u>10</u>	<u>1.02 10⁴</u>	<u>2.12</u>	<u>0.2100</u>	<u>Suggested</u>
Cubic	7.88 10 ³	2	3937.97	0.82	0.4911	Aliased
Pure Error	2.39 10 ⁴	5	4787.25			
Model Summary Statistics						
Source	Std.Dev	R ²	Adjusted R ²	Predicted R ²	PRESS	
Linear	313.178	0.840	0.815	0.709	4.47 10 ⁶	
2FI	145.086	0.974	0.960	0.904	1.48 10 ⁶	
<u>Quadratic</u>	<u>91.503</u>	<u>0.992</u>	<u>0.984</u>	<u>0.967</u>	<u>5.10 10⁵</u>	<u>Suggested</u>
Cubic	67.414	0.998	0.991	0.882	1.82 10 ⁶	Aliased

Table.A.2. Analysis of variance (ANOVA) results for the suggested quadratic model

Source	Coefficient Estimate	df	Standard Error	Sum of Squares	Mean Square	F-value	p-value Prob > F	
Intercept	1417.47	1	25.36					
X_1	-337.90	1	22.53	$1.88 \cdot 10^6$	$1.88 \cdot 10^6$	225.00	< 0.0001	
X_2	649.85	1	22.53	$6.97 \cdot 10^6$	$6.97 \cdot 10^6$	832.22	< 0.0001	
X_3	-473.77	1	22.53	$3.70 \cdot 10^6$	$3.70 \cdot 10^6$	442.34	< 0.0001	
X_4	145.69	1	22.53	$3.50 \cdot 10^5$	$3.50 \cdot 10^5$	41.83	< 0.0001	
X_1X_2	-265.18	1	22.88	$1.13 \cdot 10^6$	$1.13 \cdot 10^6$	134.38	< 0.0001	
X_1X_3	70.33	1	22.88	$7.92 \cdot 10^4$	$7.92 \cdot 10^4$	9.45	0.0077	
X_1X_4	57.57	1	22.88	$5.30 \cdot 10^4$	$5.30 \cdot 10^4$	6.33	0.0237	
X_2X_3	-206.83	1	22.88	$6.84 \cdot 10^5$	$6.84 \cdot 10^5$	81.75	< 0.0001	
X_2X_4	62.85	1	22.88	$6.32 \cdot 10^4$	$6.32 \cdot 10^4$	7.55	0.0150	
X_3X_4	-54.28	1	22.88	$4.71 \cdot 10^4$	$4.71 \cdot 10^4$	5.63	0.0314	
X_1^2	23.37	1	224.30	90.9	90.9	0.01	0.9184	
X_2^2	-216.03	1	224.30	$7.77 \cdot 10^3$	$7.77 \cdot 10^3$	0.93	0.3508	
X_3^2	135.33	1	224.30	$3.05 \cdot 10^3$	$3.05 \cdot 10^3$	0.36	0.5553	
X_4^2	-137.83	1	224.30	$3.16 \cdot 10^3$	$3.16 \cdot 10^3$	0.38	0.5481	
Model		14		$1.52 \cdot 10^7$	$1.09 \cdot 10^6$	129.95	< 0.0001	significant
Residual		15		$1.26 \cdot 10^5$	$8.37 \cdot 10^3$			
Lack of Fit		10		$1.02 \cdot 10^5$	$1.02 \cdot 10^4$	2.12	0.2100	not significant
Pure Error		5		$2.39 \cdot 10^4$	$4.79 \cdot 10^3$			
Cor Total		29		$1.54 \cdot 10^7$				